

# LISTENING TO HOT DARK SECTOR PHASE TRANSITIONS

MASTER'S THESIS IN PHYSICS

CARLO TASILLO

REVIEWERS:

Prof. Dr. Felix Kahlhöfer & Prof. Dr. Julien Lesgourgues

*The present work was submitted to:*

Faculty of Mathematics, Computer Science and Natural Sciences  
Institute for Theoretical Particle Physics and Cosmology  
RWTH Aachen University

21. May 2021

## ABSTRACT

This thesis focuses on stochastic gravitational wave backgrounds from first-order phase transitions in the early Universe driven by a dark sector beyond the Standard Model (SM). In particular, we consider the case of a dark sector hotter than the thermal bath of SM particles, which leads to a large enhancement of gravitational wave signals. The example of an additional  $U(1)$  gauge extension to the SM, which is spontaneously broken at high energies in a first-order phase transition, is studied in detail. We also calculate the dilution of the resulting gravitational wave signal caused by the entropy injection from massive dark Higgs decays into SM particles. Furthermore, the possibility of a phase of cannibalism in the dark sector is taken into consideration. A new extension to CosmoTransitions is presented that can be used to calculate signal-to-noise ratios for the detection of stochastic gravitational wave backgrounds from dark sector phase transitions with respect to current and future GW interferometers such as LISA or the Einstein Telescope.

## ACKNOWLEDGMENTS

First and foremost, I thank *Felix Kahlhöfer* for his supervision, enlightening discussions and the opportunity to write my thesis in his research group in the first place. You always treated me like a valuable member of it and gave room for asking all kinds of questions. Even though we have met only once at the institute throughout the last year due to the pandemic, you often enough responded within an instance when I contacted you. I sincerely appreciate that you left me the necessary freedom to think about other interesting questions, but told me in the right moments when I should stop pondering and start to summarize our findings. You did a great job and made me evolve into a much better physicist than I was one year ago.

I would also like to thank *Julien Lesgourgues* for agreeing to co-referee my thesis and an insightful discussion on the nature of gravitational waves and the physics of their detection. I really appreciated your efforts to make Master students engage in the recent work of other research groups in your journal club. Thank you also for your great lecture on the “Ingredients of the Universe”, which has been an essential motivation for me to work in the field of particle cosmology.

I am grateful for the co-supervision and support by *Fatih Ertas*. You not only withstood seemingly never-ending emails and proofread my whole thesis, but also encouraged me to keep a healthy work-life balance. Thank you for always taking the necessary time to answer my questions, even just before the deadline of your own thesis.

I owe thanks to *Jose Eliel Camargo-Molina* for speaking with me about the peculiarities of *CosmoTransitions* and his current work on the successor of *Vevacious*. It has been a great help and motivation to see that we are not the only group struggling with the already existing software for analyzing phase transitions. I would also like to thank *Moritz Breitbach* for giving us detailed information on his own implementation of *CosmoTransitions*.

Thanks to *Saniya Heeba*, *Silvia Manconi* and *Christian Fidler* for their initiative to organize a virtual equality reading circle, which we should by now rather call a leftist propaganda reading circle, after having discussed institutionalized and structural racism, policing and gender studies. It is really fun to discuss with you about politics and society, and a great way to get to know each other from a distance.

Outside of the institute, I owe great thanks to my friends *Jasmin Bedow* and *Simon Schwarz*. Both of them partially proofread the thesis despite their own busy schedules and without them, this work would contain many more mistakes than it still does. Next, my thanks go to *Sara Meyer*, *Lukas Weber* and *Florian Jurina*, who sent postcards back and forth with me and delighted me with virtual “fight club” sessions. Thanks to *Jerry Schmitt*, *Jérôme Jordan* and *Hauke Vossler* for late-night cooking sessions, advice concerning houseplants, and their efforts to keep fit while our bouldering gym is closed.

Furthermore, I am grateful to the *Cusanuswerk* and the *Studienstiftung des deutschen Volkes* for supporting my studies since their beginning at TU Dortmund University and later on at RWTH Aachen University as well as the Università degli Studi di Perugia.

I owe my deepest gratitude to *Roberto Cortese* for cheering me up and calming me down, whenever necessary, as well as traveling a thousand kilometers by train in the middle of a pandemic, after having missed two flights on a single day. Thank you for all your help and encouragement, which made this thesis possible.

Last but not least, I would like to thank my parents *Heike* and *Claudio* and my brother *Sandro* for their endless encouragement to always pursue my dreams. This work is as much your achievement as it is mine. You were with me every step of the way, offering unconditional love and support, without ever asking for a return.

*Turn away from me so I can have a moment's joy  
before I go to the place of no return,  
to the land of gloom and utter darkness,  
to the land of deepest night,  
of utter darkness and disorder,  
where even the light is like darkness.*

*— Job's plea to God*



# CONTENTS

1	INTRODUCTION	1
2	THEORETICAL BACKGROUND	3
2.1	The early Universe . . . . .	3
2.1.1	A chronology of the Universe . . . . .	4
2.1.2	Shortcomings of our fundamental theories . . . . .	7
2.2	Particle thermodynamics in an expanding universe . . . . .	8
2.2.1	The expanding Universe . . . . .	8
2.2.2	Particle interactions in the Universe . . . . .	9
2.2.2.1	The relativistic Boltzmann equation in an expanding Universe . . . . .	10
2.2.2.2	The collision operator . . . . .	11
2.2.2.3	The Boltzmann equation for an (inverse) decay . . . . .	11
2.2.2.4	Momenta of the Boltzmann equation . . . . .	13
2.2.2.5	Local thermal equilibrium . . . . .	14
2.3	Finite-temperature effects in quantum field theory . . . . .	16
2.3.1	The quantum harmonic oscillator in a thermal bath . . . . .	16
2.3.2	Thermal Field Theory . . . . .	17
2.3.3	The effective potential . . . . .	19
2.3.4	Treatment of the effective potential's divergences . . . . .	21
2.3.4.1	The Coleman-Weinberg contribution . . . . .	22
2.3.4.2	Hard thermal loops and daisy resummation . . . . .	22
2.3.4.3	The cancellation of the potential barrier . . . . .	25
2.3.4.4	Summary . . . . .	27
2.4	First-order phase transitions in the early Universe . . . . .	28
2.5	Gravitational waves from phase transitions . . . . .	33
2.5.1	Gravitational radiation . . . . .	34
2.5.2	Energy and momentum of gravitational waves . . . . .	37
2.5.3	Stochastic backgrounds . . . . .	40
2.5.4	The spectrum of gravitational waves from first-order phase transitions . . . . .	42
2.5.5	Detection of stochastic backgrounds . . . . .	46
3	THE DECAY OF A HOT DARK SECTOR	49
3.1	What is a hot dark sector? . . . . .	49
3.2	Local thermal equilibrium of the dark sector . . . . .	51
3.3	Out-of-equilibrium evolution of the mediator species . . . . .	55
3.3.1	A first approximation for non-relativistic decays . . . . .	55
3.3.2	Cannibalism . . . . .	57

3.4	Injecting entropy into the SM . . . . .	60
3.4.1	Derivation of the equations governing the entropy injection . . . . .	61
3.4.2	Numerical solution of the equations governing the entropy injection . . . . .	65
3.4.3	The dilution of dark matter and gravitational waves . . . . .	68
3.5	Parameterizing SGWBs from hot dark sectors . . . . .	73
4	THE DARK PHOTON MODEL . . . . .	77
4.1	Definition of the model . . . . .	77
4.2	Exploration of the model parameter space . . . . .	83
4.3	Observation of the produced gravitational waves . . . . .	87
4.4	Summary . . . . .	92
5	CONCLUSIONS . . . . .	95
A	THE SOFTWARE EMPLOYED FOR OUR CALCULATIONS . . . . .	99
	BIBLIOGRAPHY . . . . .	105

## ACRONYMS

BBN	Big Bang nucleosynthesis
BBO	Big Bang Observatory
B-DECIGO	basic DECIGO
BSM	beyond the Standard Model
CMB	cosmic microwave background
CP	charge conjugation parity
DE	dark energy
DECIGO	DECI-hertz Interferometer Gravitational wave Observatory
DM	dark matter
DOF	degrees of freedom
DS	dark sector
ET	Einstein Telescope
EWPT	electroweak phase transition
FLRW	Friedmann–Lemaître–Robertson–Walker
FOPT	first-order phase transition
GR	General Relativity
GUT	grand unified theory
GW	gravitational wave
IR	infrared
KMS	Kubo-Martin-Schwinger
$\Lambda$ CDM	$\Lambda$ cold dark matter
LIGO	Laser Interferometer Gravitational-Wave Observatory
LISA	Laser Interferometer Space Antenna
LTE	local thermal equilibrium
MHD	magnetohydrodynamic
NANOGrav	North American Nanohertz Observatory for Gravitational Waves
ODE	ordinary differential equation
PDE	partial differential equation
PLI	power-law integrated
QCD	quantum chromodynamics
QFT	quantum field theory
SGWB	stochastic gravitational wave background
SM	Standard Model
SNR	signal-to-noise ratio
TT	transverse-traceless
UV	ultraviolet
VEV	vacuum expectation value
WIMP	Weakly Interacting Massive Particle

## NOTATION

In this work, Einstein's summation convention  $\sum_{\mu} a_{\mu} b^{\mu} \equiv a_{\mu} b^{\mu}$  and the Dirac slash notation  $\not{k} \equiv k^{\mu} \gamma_{\mu}$  are used. If not stated otherwise, natural units are employed, in which  $c = \hbar = k_{\text{B}} = 1$ . Further, space-time indices are written as Greek letters, while spacial vectors are printed in boldface ( $\mathbf{x}$ ) with components denoted by Latin indices ( $x_i$ ). The flat Minkowski metric is chosen as  $\eta_{\mu\nu} \equiv \text{diag}(1, -1, -1, -1)$ , where the 0-component corresponds to the time variable (i. e.  $x^{\mu} = (x^0, \mathbf{x})$  with  $x^0 = t$ ). Partial derivatives with respect to a generic variable  $x$  are abbreviated as  $\partial_x$ ; space-time derivatives read  $\partial_{\mu} = \frac{\partial}{\partial x^{\mu}} = (\partial_t, \partial_i)$ , while total derivatives with respect to time are denoted by  $\dot{f}(t) = \frac{df}{dt}$ . A particle's four-momentum is defined as  $p^{\mu} = (E, \mathbf{p})$ , such that  $p_{\mu} x^{\mu} = E t - \mathbf{p} \cdot \mathbf{x}$  and  $d^4 p = dE d^3 p$ .

The Einstein tensor is given by  $G_{\mu\nu} \equiv R_{\mu\nu} - \frac{1}{2} R g_{\mu\nu}$  with the Ricci scalar  $R \equiv R^{\mu}_{\mu}$  and the Ricci tensor  $R_{\mu\nu} \equiv R^{\rho}_{\mu\gamma\nu}$ , which is, in turn, defined over the Riemann tensor

$$R^{\mu}_{\nu\alpha\beta} \equiv \partial_{\alpha} \Gamma^{\mu}_{\nu\beta} - \partial_{\beta} \Gamma^{\mu}_{\nu\alpha} + \Gamma^{\mu}_{\alpha\rho} \Gamma^{\rho}_{\nu\beta} - \Gamma^{\rho}_{\nu\alpha} \Gamma^{\mu}_{\beta\rho},$$

where the Christoffel symbols

$$\Gamma^{\alpha}_{\mu\nu} \equiv \frac{1}{2} g^{\alpha\beta} (\partial_{\mu} g_{\beta\nu} + \partial_{\nu} g_{\beta\mu} - \partial_{\beta} g_{\mu\nu})$$

can be calculated as space-time derivatives of the metric  $g_{\mu\nu}$ . To simplify the Einstein equations, the reduced Planck mass  $M_{\text{pl}} = (8 \pi G)^{-1/2} \approx 2.4 \cdot 10^{18} \text{ GeV}$  is employed, where  $G$  is Newton's gravitational constant. By default, energies, temperatures, masses, and momenta are all given in units of  $\text{eV} \approx 1.6 \cdot 10^{-19} \text{ J}$ , whereas spacial and temporal distances come with inverse energy units.

# 1 | INTRODUCTION

Little more than 100 years ago, in 1916, Albert Einstein first predicted the existence of gravitational waves (GWs) as a consequence of his theory of General Relativity (GR) [1, 2]. However, due to the relative weakness of gravity, it took until 2016 to finally confirm that Einstein’s conclusion was right: The LIGO collaboration observed a merger of two black holes with about 30 solar masses each, at a distance of 1.3 billion light-years from Earth [3]. This observation can be seen as the starting shot for the era of GW astronomy. Until today, we have seen more than 50 individual signals of compact binary coalescences using a quickly growing family of GW interferometers [4, 5]. Due to the finite velocity of propagation of these waves, each event works as a puzzle piece to broaden our intellectual and observational horizon.

*A short history of  
GW astronomy*

Our findings from the measurements of the cosmic microwave background (CMB) state that our Universe had its beginning in the hot “Big Bang” era about which we, however, still know very little for certain. Interpreting the temperature anisotropies of the photons coming from this period, when our Universe was just some 380,000 years old, allowed us to define our current concordance model of cosmology [6]. For testing our theories of the early cosmos and for unraveling the flaws of the so-called  $\Lambda$  cold dark matter ( $\Lambda$ CDM) model, it is of paramount importance to directly observe what happened before the emission of the CMB. It is hence highly anticipated that the detection of a stochastic gravitational wave background (SGWB) coming from times before the emission of the CMB will reduce this gap and revolutionize what we know about our Universe [7].

*Testing our models  
of the very early  
Universe*

Just in September of the last year, we might have found the first hint for an SGWB in the 12.5 years data analysis of the NANOGrav collaboration [8]. Although the detected GWs could be explained by an astrophysical background, they could as well stem from very early Universe processes [9]. In any case their detection can be seen as an auspicious proof of principle for what will be possible with the planned space interferometers to be launched in the next years and decades. There exist only a few currently known processes in the very early Universe that could have produced an observable SGWB, e. g. time-varying scalar fields, inflation, kinks and cusps in cosmic strings, and first-order phase transitions (FOPTs) [10]. A detection of a signal coming from one of these processes would have a profound impact on our knowledge of cosmology and high-energy physics. Their detection

*Stochastic  
gravitational wave  
backgrounds*

is however complicated by the astrophysical confusion noise of many weak, independent, and unresolved sources like binary black holes or neutron star mergers [10, 11].

*Boosting and  
diluting GW signals  
from dark sectors*

In this thesis, a novel effect boosting the signal strengths of an SGWB from FOPTs is investigated. Assuming that the phase transition takes place in a dark sector (DS) that is initially decoupled from the particles of the SM, it has to be taken into account that the thermal DS and SM baths will in general have different temperature due to the lack of interaction between them [12]. It is shown that DS temperatures above that of the SM bath yield signal strengths that can be orders of magnitude higher than those in the case of a common temperature. Finally, the DS cannot be fully decoupled from the SM bath for all times, since otherwise the lightest dark sector particles could not decay. In that case, the DS would store too much energy and overclose the Universe, leading to its early collapse. This issue can be circumvented by allowing for a decay mechanism of the lightest dark sector state to the SM. Upon this decay, a considerable amount of entropy can be injected into the SM bath which will inevitably dilute frozen-out abundances such as dark matter [13] or the SGWB that has just been produced. This can be understood as a second, independent effect.

*The investigated  
dark sector model*

To demonstrate both effects, a simple particle physics model for a hot dark sector phase transition is used: The SM is extended by an additional  $U(1)_D$  gauge group whose respective gauge boson becomes massive when a complex scalar charged under the gauge group acquires a vacuum expectation value (VEV). The gauge boson is referred to as a “dark photon” due to its lack of interaction with the SM particle species and its similar description with respect to the SM photon, being the gauge boson of the  $U(1)_{EM}$  group for electromagnetism. The scalar field, whose real part becomes massive when it acquires a VEV, is referred to as a “dark Higgs field” by analogy to the SM Higgs field, with which it can mix, giving rise to a decay channel of the dark Higgs boson into SM particles. Mass mixing represents the only effective coupling between the DS and SM particles, which are assumed to carry no charge of the “dark” gauge group  $U(1)_D$ .

*Structure of this  
thesis*

This work is structured as follows: Chapter 2 gives an overview of the theoretical foundations that were used for the subsequent analysis. This comprises an overview of particle cosmology in the early Universe as well as an introduction to SGWBs and their production through FOPTs. In chapter 3, we study the thermal evolution of a DS after it featured an FOPT and discuss the theoretical origins of the two effects mentioned above. The findings are then applied to the proposed dark photon model in chapter 4. A conclusion and discussion of the general results can be found in chapter 5. Finally, a detailed description of our to-be-published tool for calculating SGWB spectra for DS phase transitions is provided in Appendix A.

## 2 | THEORETICAL BACKGROUND

In this chapter the theoretical foundation for what follows is discussed. The overview is organized in five parts: First, a general picture of what we know and do not know about the early Universe is drawn in section 2.1. A closer look on the quantitative description of this period using the Friedmann and relativistic Boltzmann equations is given in section 2.2. In section 2.3, finite-temperature effects in quantum field theory (QFT) are investigated with which the effective potential of a given particle physics model can be calculated. The effective potential is then used to study FOPTs in section 2.4. Finally, the connection between GWs and FOPTs and how the resulting SGWB can be determined is outlined in section 2.5.

### 2.1 THE EARLY UNIVERSE

Due to the speed of light being finite, a look into space is always a look into the past. The place where we can currently look farthest is called the surface of last scattering, which is depicted artistically in figure 2.1 by a thin red line. What happened since then, when the CMB had been emitted, is the formation of stars, galaxies and complex structure and, lately, the evolution of life being able to theorize about its origins. What happened during and before all this is within the domain of research of cosmology. The following review of the different events that happened until today is based on the references [6, 15].

*The CMB*

Our current understanding of what has happened before the emission of the CMB stems to a large extent from the precise investigation of the temperature variations across the surface of last scattering measured by the Planck collaboration [16]. Our best model for the cosmic evolution is the  $\Lambda$ CDM model, which is based on only six parameters, describing the matter content of the Universe, its present rate of expansion, the precise form of the surface of last scattering and the physical properties of a period called inflation [15].

*“The Big Bang theory”*

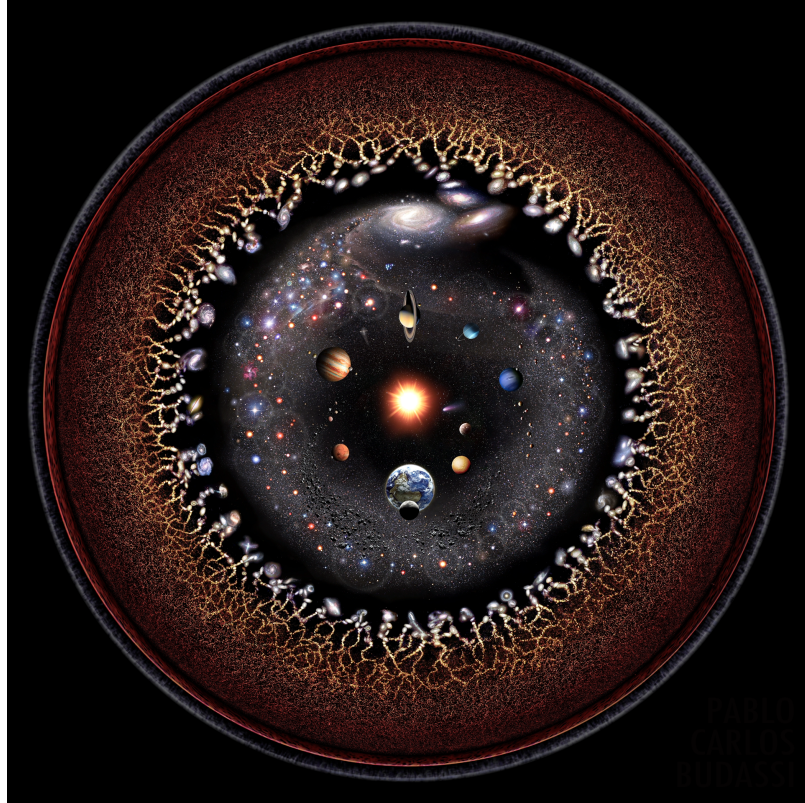


Figure 2.1: An artistic overview of the observable Universe on logarithmic scales taken from reference [14].

### 2.1.1 A chronology of the Universe

#### *Inflation*

The earliest event, about 13.8 billion years ago [16], that is described within the  $\Lambda$ CDM model is *inflation*. In a period that lasted approximately  $10^{-33}$  s, space expanded by an enormous factor of at least  $10^{26}$ . Inflation is thought to have been triggered by the phase transition that broke the so-called grand unified theory (GUT) at some temperature below  $10^{15}$  GeV. In that process, a scalar field (called “the inflaton”) acquired a VEV that resulted in a repulsive force, starting the accelerated expansion of space. The process ended with the decay of the inflaton field into the dense, hot plasma of frequently interacting elementary particles [6]. In a process called “baryogenesis” (still being an active field of research) the asymmetry of matter and anti-matter has then been produced. A second phase transition followed, which is referred to as the electroweak phase transition (EWPT), during which the Higgs boson of the SM acquired a VEV, giving mass to before massless particle species through the Higgs mechanism. Several models explain baryogenesis by a first-order EWPT, requiring extensions to the SM in which the EWPT is a smooth phase transition [17].

#### *Baryogenesis and the electroweak phase transition*

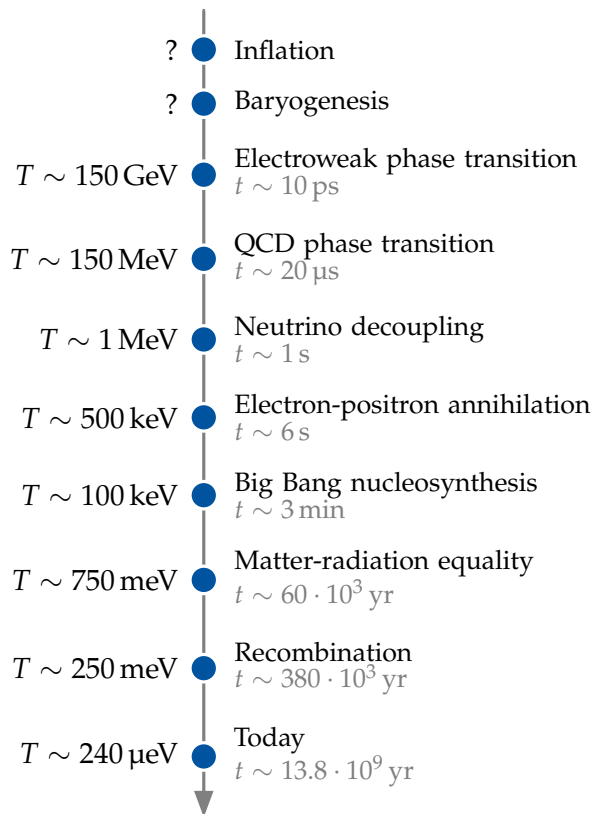


Figure 2.2: A timeline of important events in cosmology. The quoted temperatures refer to the SM bath, which will be defined in chapter 3.1.

The subsequent events (see Figure 2.2) can be described by considering a thermal equilibrium between the different particle species of the SM and their successive deviation from it. As first, quarks and gluons lose their asymptotic freedom and confine to hadrons, i. e. baryons and mesons, in a process known as the quantum chromodynamics (QCD) phase transition. Then, neutrinos decouple from the remaining thermal bath of SM particles. Due to their only weak coupling to other particle species and very low masses, their decoupling happens so early that they remain relativistic afterwards. When the temperature of the photon bath drops below the mass of electrons and positrons, both species become Boltzmann suppressed. Since entropy is conserved during the expansion (as will be described in section 2.2.2.5 more thoroughly), the electrons' and positrons' entropy is injected into the photon bath, reheating it with respect to the already decoupled neutrinos [6].

*QCD phase transition, neutrino decoupling and electron-positron annihilation*

About three minutes after the end of inflation, protons and neutrons combine to the first (still ionized) elements, i. e. helium, deuterium and lithium, during the Big Bang nucleosynthesis (BBN). The observation of very far (hence, very young) galaxies allows us to check the produced

*Big Bang nucleosynthesis*

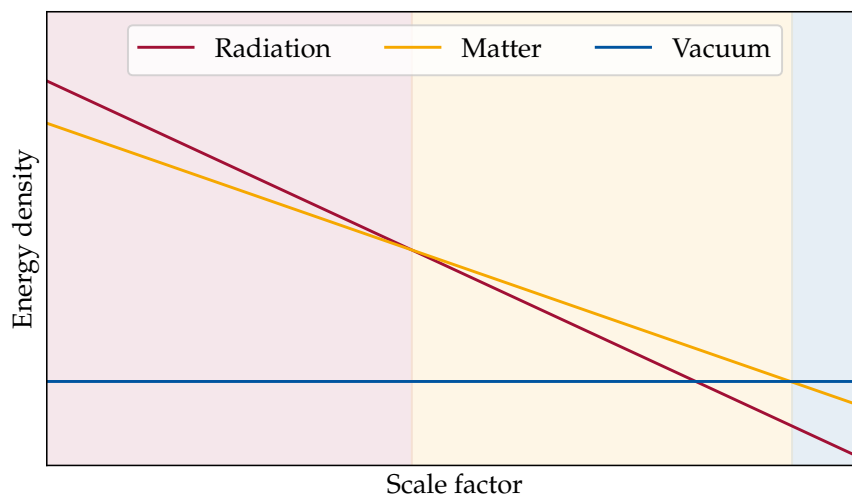


**Figure 2.3:** A sketch of the temporal evolution of the contributions to the Universe's energy density. Inflation is followed by phases of radiation and matter domination. Today's vacuum domination due to some still unknown form of dark energy began only recently a new period of accelerated expansion of the Universe.

element abundances, giving us the very first cosmological constraints for beyond the Standard Model (BSM) physics.

*Matter-radiation  
equality*

About 60,000 years after the end of inflation, non-relativistic matter becomes the most dominant part of the energy density content of the Universe. This is due to the different time evolutions of relativistic and non-relativistic matter: While a non-relativistic species' energy density decreases only due to its dilution during the expansion of the Universe, relativistic particles (which are conventionally referred to as "radiation" as opposed to "matter") also lose energy due to their individual redshift (see Figure 2.3).

*Recombination and  
vacuum domination*

Finally, when the Universe has cooled enough for electrons to bound to atomic cores, photons can propagate freely through the now no longer opaque Universe. The first "snapshot" of it is what we today call the CMB. In the remaining billions of years until today, matter begins to clump, forming astrophysical objects like our Sun. Only a few billion years ago, vacuum energy became (again) the dominant energy contribution and led anew to an accelerated expansion of space (see Figure 2.4). Recently, life started to evolve somewhere in the Milky Way, which learned how to organize itself and how to do science to ponder efficiently over its place in the world.

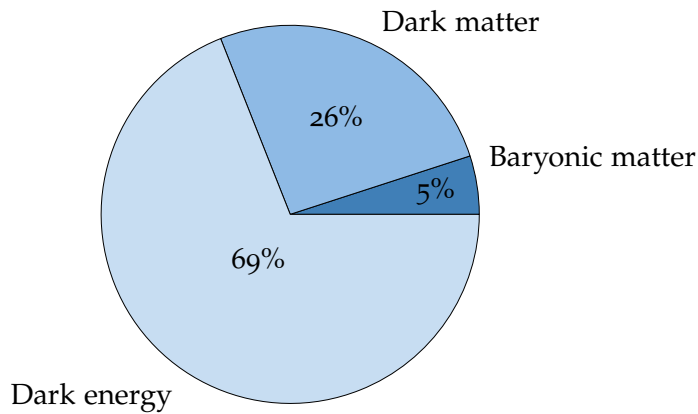


Figure 2.4: Today's energy density content of the Universe as it was measured by the Planck collaboration [16].

### 2.1.2 Shortcomings of our fundamental theories

In some sense, the presented cosmic timeline is still speculative: An inflaton particle has never been directly measured in a collider experiment, and we still are pretty much in the dark concerning what a potential GUT or even more fundamental theories should look like. These problems are however not the only ones. The major part of perplexity connected to the  $\Lambda$ CDM model comes with its name: As was found in the analysis of the CMB anisotropies measured by the Planck collaboration [16] (see Figure 2.4), about 95% of our Universe's energy density is "dark", hence unknown, to us. We know that there has to be a lot more matter (i. e., dark matter (DM)) in our galaxies than optically visible, but we do not know which particle species could account for this. Further, we know that there is this amount of vacuum energy that currently re-accelerates the expansion of our Universe (i. e., dark energy (DE)), but we do not know where it comes from. Since both problems are so urging, they were combined in the name of our concordance model of cosmology:  $\Lambda$  is some generic vacuum energy, while "CDM" accounts for cold (i. e., slowly moving) DM, which is favored by theories explaining the cosmic structure formation [18]. Of course, there exist also a lot of other problems, namely hierarchy problems in the SM [19], missing neutrino masses [20], the origin of the matter-antimatter asymmetry [21], and the Hubble tension [16], to just name a few of them.

*Dark matter and dark energy*

To explain these shortcomings of our fundamental theories, it appears necessary to add new particle species to the SM. Currently, there exist a lot of potential explanations for DM, the most famous one being the Weakly Interacting Massive Particle (WIMP) idea, which is however strongly constrained [22]. Thus, there is need for alternative explanations beyond the WIMP paradigm. DSs showed to be promising for

*Motivation for  
investigating dark  
sectors*

comprising new candidates for DM [23]. At the same time, the search for new physics at colliders is getting closer to the border of becoming economically unfeasible. All this, together with the observation that large parts of the already known history of the Universe showed to be a series of phase transitions and the upcoming possibilities to detect SGWBs, motivates the study of extensions to the SM testable by GW measurements. But before getting into details about the physics of cosmic phase transitions, it is necessary to understand how to describe quantitatively the thermodynamics of different particle species in an expanding Universe. The next section is aimed at providing the necessary background.

## 2.2 PARTICLE THERMODYNAMICS IN AN EXPANDING UNIVERSE

At early times, the evolution of the Universe was determined by local thermal equilibrium (LTE)—however, what makes life interesting are the departures from equilibrium. Without the deviations from it, the present Universe would likely just be homogeneous, cold and dull. To study what determined the particle dynamics in the early Universe, it is thus necessary to first describe the homogeneous Universe (subsection 2.2.1) that will act as a stage for what happens on it when one includes interacting particle species (subsection 2.2.2).

### 2.2.1 The expanding Universe

According to GR, our Universe can be described by the Einstein field equations

$$m_{\text{Pl}}^2 G_{\mu\nu} = T_{\mu\nu} . \quad (2.1)$$

Here,  $G_{\mu\nu}$  is the Einstein tensor which is a complicated, nonlinear function of the metric  $g_{\mu\nu}$  and its space-time derivatives, and  $T_{\mu\nu}$  is the energy-momentum tensor, describing the position and movement of energy densities. Since the existence of a cosmological constant  $\Lambda$  is irrelevant for the cosmology of the primordial Universe it is ignored in this discussion [15].

As all observations on large scales indicate that our Universe is homogeneous and isotropic, the metric and the energy-momentum tensor are both subject to tight constraints. Both quantities can depend only on time due to homogeneity, while isotropy requires them to be diagonal, where the remaining spacial components are equal to each other.

The most general metric that fulfills this criteria for the case of a flat Universe is the Friedmann–Lemaître–Robertson–Walker (FLRW) metric

*The FLRW metric*

$$(g_{\mu\nu})(t) = \text{diag}[1, -a(t), -a(t), -a(t)] . \quad (2.2)$$

Since in this metric the infinitesimal volume element is given by  $dV = a^3(t) d^3x$ , the function  $a(t)$  is called the “scale factor” which translates between physical and coordinate distances. The energy-momentum tensor is given by

$$(T_{\mu\nu})(t) = \text{diag}[\rho_{\text{tot}}(t), -P_{\text{tot}}(t), -P_{\text{tot}}(t), -P_{\text{tot}}(t)] , \quad (2.3)$$

where  $\rho_{\text{tot}}$  ( $P_{\text{tot}}$ ) is the energy density (pressure) of a perfect fluid by which the hot plasma of the early Universe is described [6]. Inserting these quantities into the Einstein field equation (2.1) yields two independent ordinary differential equations (ODEs) for the scale factor, which are called the first and second Friedmann equations. They can be written as

*The Friedmann equations*

$$H(t) \equiv \frac{\dot{a}(t)}{a(t)} = \sqrt{\frac{\rho_{\text{tot}}(t)}{3 m_{\text{Pl}}^2}} , \quad (2.4a)$$

$$\dot{H}(t) + H^2(t) = \frac{\ddot{a}(t)}{a(t)} = -\frac{\rho_{\text{tot}}(t) + 3 P_{\text{tot}}(t)}{6 m_{\text{Pl}}^2} . \quad (2.4b)$$

The first equation defines the Hubble rate  $H(t)$ , which works as a measure for the velocity of the expansion of the Universe. Today’s Hubble rate is commonly referred to as the Hubble parameter, which was measured to have a value of  $H_0 = 68 \text{ km s}^{-1} \text{ Mpc}^{-1} = 2.1 \cdot 10^{-42} \text{ GeV}$  [16]. A more familiar form of the second Friedmann equation can be obtained by differentiating the first Friedmann equation and then reinserting it into the second one. We obtain the relation

$$\dot{\rho}_{\text{tot}}(t) + 3 H(t) [\rho_{\text{tot}}(t) + P_{\text{tot}}(t)] = 0 , \quad (2.5)$$

describing energy and momentum conservation in the expanding Universe. This interpretation can be made clear by comparing to the  $\nu = 0$  component of the energy-momentum conservation  $\nabla^\mu T_{\mu\nu} = 0$  in GR, which contains the same relation [6]. In the following, equation (2.5) will be referred to as the second Friedmann equation. In the next subsection, it will become apparent why this expression is of particular importance when dealing with different interacting particle species.

*An alternative second Friedman equation*

### 2.2.2 Particle interactions in the Universe

The evolution of the scale factor can be obtained from the Friedmann equations once one knows how the energy density of the initially

*Describe particle species statistically*

hot plasma evolves with time. This section is aimed at giving an overview of how one can calculate this and other thermodynamic quantities. From the sheer number of individual particles it is already clear, that one cannot just keep track of them individually, but that one has to work with particle ensembles as they are defined in statistical mechanics: For high particle densities, the particle species' nature is fully characterized by its phase-space distribution function  $f_x(t, \mathbf{x}, \mathbf{p})$ , where  $x$  denotes the respective species. The total particle number in an infinitesimal phase-space volume is then encoded within the relation

$$dN_x = \frac{g_x}{(2\pi)^3} f_x(t, \mathbf{x}, \mathbf{p}) d^3p d^3x, \quad (2.6)$$

where the number of spin states of  $x$  is counted by  $g_x$ .

### 2.2.2.1 The relativistic Boltzmann equation in an expanding Universe

The evolution of  $f_x(t, \mathbf{x}, \mathbf{p})$  is governed by the relativistic Boltzmann equation [6, 24]

$$\underbrace{\left( p^\mu \frac{\partial}{\partial x^\mu} - \Gamma_{\alpha\beta}^\mu(t, \mathbf{x}) p^\alpha p^\beta \frac{\partial}{\partial p^\mu} \right) f_x(t, \mathbf{x}, \mathbf{p})}_{\equiv \mathcal{L}[f_x](t, \mathbf{x}, \mathbf{p})} = \mathcal{C}[f_x, \dots](t, \mathbf{x}, \mathbf{p}). \quad (2.7)$$

While the Liouville operator  $\mathcal{L}[f_x]$  encodes the change of  $f_x$  due to GR effects, the collision operator  $\mathcal{C}[f_x, \dots]$  encodes the effects of particle interactions as they are described in an underlying QFT. Since in general, multiple species interact with each other,  $\mathcal{C}[f_x, \dots]$  is not only a functional of  $f_x$  but further depends also on other distribution functions as indicated by the ellipsis.

*The Boltzmann equation in an expanding Universe*

For the case of the homogeneous and isotropic FLRW Universe, this equation simplifies considerably to [6]

$$\partial_t f_x(t, p) - H(t) p \partial_p f_x(t, p) = \frac{\mathcal{C}[f_x, \dots](t, p)}{E_x(p)} \quad (2.8)$$

with  $E_x = \sqrt{p^2 + m_x^2}$ . Note that the phase-space distribution function  $f_x$  only depends on time and the momentum's modulus  $p = |\mathbf{p}|$ , since due to homogeneity and isotropy all positions and directions in space should show equivalent physics. The Boltzmann equation as it is written in (2.8) can be used to describe the various processes of early-Universe cosmology, like the freeze-in or freeze-out of DM, BBN or the decay of a DS, as in our case.

### 2.2.2.2 The collision operator

For using the Boltzmann equation, it is crucial to understand the collision operator within and how to derive it from a given QFT. One can show that the collision operator can be written as [24]

$$\begin{aligned} \mathcal{C}[f_x, \dots](t, p_x) &= \frac{g_x^{-1}}{2} \sum_{r \in \mathcal{R}_x} \epsilon_r \int \prod_{s \in (\mathcal{I}_r \cup \mathcal{F}_r) \setminus \{x\}} \frac{d^3 p_s}{(2\pi)^3 2E_s} \\ &\times (2\pi)^4 \delta^{(4)} \left( \sum_{k \in \mathcal{I}_r} p_k - \sum_{l \in \mathcal{F}_r} p_l \right) \\ &\times |\mathcal{M}_r|^2 \prod_{m \in \mathcal{F}_r} (1 \pm f_m) \prod_{n \in \mathcal{I}_r} f_n. \end{aligned} \quad (2.9)$$

Therein,  $\mathcal{R}_x$  is the set of all possible particle interactions of the species  $x$  and the set  $\mathcal{I}_r$  ( $\mathcal{F}_r$ ) contains all species of the reaction  $r \in \mathcal{R}_x$  in the initial (final) state. To account for the increase or decrease of the phase-space distribution function when  $x$  particles are produced or destroyed, the factor  $\epsilon_r$  is equal to  $+1$  ( $-1$ ) if  $x$  is a final-state (initial-state) particle of  $r$ . Further, the occurring Dirac delta distribution  $\delta^{(4)}$  handles the conservation of four-momenta, such that its product with the squared matrix elements<sup>1</sup>  $|\mathcal{M}_r|^2$  works as a measure of probability for the reaction  $r$ . Finally, the  $\pm$  signs in the product of the final-state distribution functions evaluate to  $+$  ( $-$ ) when  $f_m$  describes a boson (fermion), encoding effects of quantum statistics [24].

*Understanding the right-hand side of the Boltzmann equation*

### 2.2.2.3 The Boltzmann equation for an (inverse) decay

In principle, once the corresponding matrix elements are known, the evolution of the particle content of the universe can now be calculated by a set of coupled Boltzmann equations describing each individual particle species and their respective interactions. In most cases, this is however computationally unfeasible. To nonetheless illustrate the evolution of an interacting particle species, it is worth setting up the Boltzmann equation for the (inverse) decay of a generic particle species  $x \leftrightarrow z\bar{z}$ . The presented calculation follows the one described in [24].

In our case, the set of relevant reactions is  $\mathcal{R}_x = \{x \rightarrow z\bar{z}, z\bar{z} \rightarrow x\}$ , where the sets of initial- and final-state particles are given by  $\mathcal{I}_{x \rightarrow z\bar{z}} = \mathcal{F}_{z\bar{z} \rightarrow x} = \{x\}$  and  $\mathcal{I}_{z\bar{z} \rightarrow x} = \mathcal{F}_{x \rightarrow z\bar{z}} = \{z, \bar{z}\}$ . Assuming time (or equivalently, CP) invariance, the matrix element  $|\overline{\mathcal{M}}| \equiv g_x^{-1} |\mathcal{M}|$  is the same

*Investigating the simple case of the reaction  $x \leftrightarrow z\bar{z}$*

<sup>1</sup> The matrix element  $|\mathcal{M}_r|^2$  is summed over the spins of all initial- and final-state particles. To compensate the sum over the spin of  $x$ , an additional factor of  $g_x^{-1}$  is included in equation (2.9). Further, all symmetry factors are assumed to be already included within the matrix element.

for both reactions and can be expressed in terms of a total lifetime of the species  $x$ :

$$\frac{1}{\tau_x} = \frac{\beta_z}{16 \pi m_x} |\overline{\mathcal{M}}|^2 \quad \text{with} \quad \beta_z \equiv \sqrt{1 - \frac{4 m_z^2}{m_x^2}}. \quad (2.10)$$

Upon performing the integration over the momentum space of the  $z$  particle, one ends up with the Boltzmann equation

$$\begin{aligned} \partial_t f_x(t, p) - H(t) p \partial_p f_x(t, p) \\ = -\frac{m_x}{E_x \tau_x} f_x(t, p) \\ + \frac{m_x}{E_x \tau_x} \frac{1}{\beta_z p} \int_{p_-}^{p_+} f_z(t, p_z) f_{\bar{z}}(t, p_{\bar{z}}) \frac{p_{\bar{z}} dp_{\bar{z}}}{E_{\bar{z}}} \\ \pm \frac{m_x}{E_x \tau_x} \frac{f_x(t, p)}{\beta_z p} \int_{p_-}^{p_+} [f_z(t, p_z) + f_{\bar{z}}(t, p_{\bar{z}})] \frac{p_{\bar{z}} dp_{\bar{z}}}{E_{\bar{z}}}. \end{aligned} \quad (2.11)$$

The first term on the right-hand side of this equation describes the expected relation  $\dot{N}_x \sim -N_x/\tau_x$  for the decaying particle species including an additional boost factor  $\gamma_x = E_x/m_x$  to account for relativistic decays. In accordance with special relativity, the lifetime  $\tau_x \gamma_x > \tau_x$  of the decaying species thus gets effectively increased in the lab frame. The remaining two terms describe effects from quantum statistics and inverse decays, explicitly depending on the distribution functions of  $z$  and  $\bar{z}$ , which would require additional Boltzmann equations for these particle species for a general solution. Therein,  $p_{\pm} = \sqrt{E_{\pm}^2 - m_z^2}$  are the extremal values of  $p_{\bar{z}}$  that are allowed kinematically by the decay, where  $2 E_{\pm} = E_x \pm p_x \beta_z$ .

Ignoring inverse decays for simplicity<sup>2</sup> leaves us with a considerably simpler Boltzmann equation. This equation can be solved analytically by using the method of characteristics, which transforms the partial differential equation (PDE) into an ODE. Assuming that  $H(t)$  is independent of  $f_x(t, p)$ , one can introduce a function  $s(t, p)$  which fulfills the properties  $\frac{dt}{ds} = 1$  and  $\frac{dp}{ds} = -H(t) p$ , such that

$$\begin{aligned} \frac{df_x(t, p)}{ds} &= \frac{\partial f_x}{\partial t} \frac{dt}{ds} + \frac{\partial f_x}{\partial p} \frac{dp}{ds} \\ &= \frac{\partial f}{\partial t} - \frac{\partial f}{\partial p} H(t) p = -\frac{m_x}{E_x \tau_x} f_x. \end{aligned} \quad (2.12)$$

*The Boltzmann equation becomes an easily solvable ODE*

Solving for  $s(t, p)$  and inserting it into the resulted ODE leads to

$$\frac{d}{dt} f_x \left( t, \frac{p}{a(t)} \right) = -\frac{m_x}{E_x \tau_x} f_x \left( t, \frac{p}{a(t)} \right), \quad (2.13)$$

<sup>2</sup> If one included inverse decays in the following discussion, one would end with a similar result, where the effective lifetime of the species  $x$  had to be modified accordingly [24].

which can be easily solved by integrating with an appropriate initial condition [24]. The physical interpretation of this equation is that the decay and the redshift of particle momenta can be considered independently. This equation will be solved once the initial conditions for the investigated problem at hand become clear in chapter 3.

#### 2.2.2.4 Momenta of the Boltzmann equation

In order to use the results of the solution of the Boltzmann equation within the context of the Friedmann equation, one has to translate from the distribution function  $f_x(t, p)$  to quantities like the energy density  $\rho_x(t)$  or the pressure  $P_x(t)$ . Beyond that, also the number density  $n_x(t)$  and the entropy density  $s_x(t)$  can be calculated by integrating the distribution function. In special cases, these quantities can even be inferred without the need to derive their underlying distribution functions before, as will be shown in section 2.2.2.5 for the case of ultra-relativistic and non-relativistic species in thermal equilibrium.

The number density can be obtained from the phase-space distribution function by an integration  $\int \cdot g_x d^3p / (2\pi)^3$  over the momentum space,

*The number density*

$$n_x(t) = \frac{g_x}{2\pi^2} \int_{\mathbb{R}} p^2 dp f_x(t, p). \quad (2.14)$$

Thus, integrating the Boltzmann equation (2.8) over momentum space yields<sup>3</sup>

$$\dot{n}_x(t) + 3H(t)n_x(t) = \frac{g_x}{2\pi^2} \int_{\mathbb{R}} p^2 dp \frac{\mathcal{C}[f_x, \dots](t, p)}{\sqrt{p^2 + m_x^2}}. \quad (2.15)$$

Like the number density, also the energy density and the pressure can be obtained by integrating the distribution function, this time after multiplying it with  $E_x(p)$  and  $p^2 / [3E_x(p)]$ , respectively [6]:

*Energy density and pressure*

$$\rho_x(t) = \frac{g_x}{2\pi^2} \int_{\mathbb{R}} p^2 dp \sqrt{p^2 + m_x^2} f_x(t, p), \quad (2.16a)$$

$$P_x(t) = \frac{g_x}{6\pi^2} \int_{\mathbb{R}} p^2 dp \frac{p^2}{\sqrt{p^2 + m_x^2}} f_x(t, p). \quad (2.16b)$$

By integrating the Boltzmann equation over  $\int \cdot E_x g_x d^3p / (2\pi)^3$ , one obtains

$$\dot{\rho}_x(t) + 3H(t)[\rho_x(t) + P_x(t)] = \frac{g_x}{2\pi^2} \int_{\mathbb{R}} p^2 dp \mathcal{C}[f_x, \dots](t, p). \quad (2.17)$$

<sup>3</sup> This and the following integrations can be done by parts, requiring the distribution function weighted with powers of  $p$  to vanish at  $p \rightarrow \infty$ . Since high momenta are typically exponentially suppressed, this condition is fulfilled.

A comparison with the second Friedmann equation (2.5) already gives an important result for the coming discussion on dark sectors: After having identified the volume heating rate as

$$\dot{q}_x(t) \equiv \dot{\rho}_x(t) + 3H(t) [\rho_x(t) + P_x(t)] , \quad (2.18)$$

*Total heat is conserved*

the second Friedmann equation tells us that the total heat of the Universe is conserved ( $\dot{q}_{\text{tot}} = 0$ ) and can only be transferred between different particle species and, eventually, interacting sectors of particle physics [24]. The discussion in chapter 3 will come back to this result.

*The entropy density*

Ultimately, the entropy density can be calculated as the integral over the Boltzmann entropy  $\mathcal{S}_B(t, p)$  [25]

$$s_x(t) = -\frac{g_x}{2\pi^2} \int_{\mathbb{R}} p^2 dp \underbrace{[f_x \ln(f_x) \mp (1 \pm f_x) \ln(1 \pm f_x)]}_{\equiv \mathcal{S}_B(t, p)} , \quad (2.19)$$

where the upper (lower) sign again describes bosons (fermions). Integrating over  $\int \cdot \ln[f_x / (1 + f_x)] g_x d^3p / (2\pi)^3$ , one finds

$$\begin{aligned} \dot{s}_x(t) + 3H(t) s_x(t) = \\ -\frac{g_x}{2\pi^2} \int_{\mathbb{R}} p^2 dp \ln \left( \frac{f_x(t, p)}{1 \pm f_x(t, p)} \right) \frac{\mathcal{C}[f_x, \dots](t, p)}{\sqrt{p^2 + m_x^2}} . \end{aligned} \quad (2.20)$$

Note that the obtained equations for  $\dot{n}_x$ ,  $\dot{\rho}_x$  and  $\dot{s}_x$  do not necessarily simplify the calculation. Only under certain assumptions, the integral on their respective right-hand side can be expressed analytically in terms of the thermodynamical quantities  $n_x$ ,  $\rho_x$  and  $s_x$ . When this is the case, the simplification is, however, substantial. Then, after having summed up the individual energy densities to  $\rho_{\text{tot}}(t) \equiv \sum_x \rho_x(t)$ , the first Friedmann equation (2.4a) can be solved without further ado.

So far, only intrinsic thermodynamic quantities have been discussed. The connection to extrinsic quantities is simple as the left-hand sides of the equations (2.15), (2.17) and (2.20) case can also be written as  $\dot{N}_x(t)$ ,  $\dot{Q}_x(t)$  and  $\dot{S}_x(t)$ , where  $N_x(t) \equiv n_x(t) a^3(t)$ ,  $S_x(t) \equiv s_x(t) a^3(t)$ , and the heating rate is defined as  $\dot{Q}_x(t) \equiv \dot{q}_x(t) a^3(t)$ .

### 2.2.2.5 Local thermal equilibrium

*Thermal distributions*

Everything presented so far can be used to calculate  $f_x(t, p)$  in full generality. The discussion can however be simplified significantly by considering tightly coupled species. Since particle species interact strongly after the end of inflation, they equilibrate and form an LTE. If one says that  $x$  is in LTE, one means that there is a unique temperature  $T_x(t)$  and the corresponding momentum spectrum is given by either a Bose-Einstein (−) or a Fermi-Dirac (+) distribution

$$f_x(t, p) = \left[ \exp \left( \frac{E_x(p) - \mu_x(t)}{T_x(t)} \right) \mp 1 \right]^{-1} , \quad (2.21)$$

with  $\mu_x(t)$  denoting the chemical potential of  $x$ . Inserting this distribution function into (2.20), it follows that

$$\begin{aligned} \dot{S}_x(t) &= a^3(t) \frac{g_x}{2\pi^2} \int_{\mathbb{R}} p^2 dp \frac{\mathcal{C}[f_x, \dots](t, p)}{E_x(p)} \frac{E_x(p) - \mu_x(t)}{T_x(t)} \\ &\stackrel{(2.15)}{=} \frac{\dot{Q}_x(t) - \mu_x(t) \dot{N}_x(t)}{T_x(t)} \end{aligned} \quad (2.22)$$

$$\Leftrightarrow T_x(t) \dot{S}_x(t) = \dot{Q}_x(t) - \mu_x(t) \dot{N}_x(t). \quad (2.23)$$

The second law of thermodynamics therefore holds for each individual particle species in LTE. Furthermore, one can conclude that a particle species' entropy is conserved, when there is no heat transfer to other particle species ( $\dot{Q}_x(t) = 0$ ) and the product  $\mu_x(t) \dot{N}_x(t)$  vanishes. The latter will be the case if either the chemical potential of  $x$  is zero ( $\mu_x(t) = 0$ ) or if its particle number is conserved in a comoving volume ( $\dot{N}_x(t) = a^3(t) [\dot{n}_x(t) + 3H(t)n_x(t)] = 0$ ).

*Recovering the second law of thermodynamics*

Inserting (2.21) into (2.20) and using (2.15) and (2.17) anew, one finds that

$$T_x(t) s_x(t) = \rho_x(t) + P_x(t) - \mu_x(t) n_x(t), \quad (2.24)$$

which connects all the calculated thermodynamical quantities and can be used to calculate the entropy density of a given species in LTE.

Moreover, it is possible to derive analytic expressions for  $n_x(t)$ ,  $\rho_x(t)$  and  $P_x(t)$  in the case of ultra-relativistic and non-relativistic particles [6]: For a relativistic species, the distribution function can be simplified using  $T_x(t) \gg m_x, \mu_x(t)$ . Integrating the resulting distribution function yields

*Radiation and dust*

$$n_x(t) \simeq \frac{\zeta(3)}{\pi^2} g_x T_x^3(t) \times \begin{cases} 1 & \text{for bosons} \\ 3/4 & \text{for fermions} \end{cases}, \quad (2.25a)$$

$$\rho_x(t) \simeq \frac{\pi^2}{30} g_x T_x^4(t) \times \begin{cases} 1 & \text{for bosons} \\ 7/8 & \text{for fermions} \end{cases}, \quad (2.25b)$$

$$P_x(t) \simeq \rho_x(t)/3. \quad (2.25c)$$

Conversely, for non-relativistic particles,  $T_x(t) \ll m_x$  and  $E_x(p)/T_x(t) \simeq m_x/T_x(t) + p^2/(2m_x T_x(t))$  hold, such that

$$n_x(t) \simeq g_x \left( \frac{m_x T_x(t)}{2\pi} \right)^{3/2} e^{(\mu_x(t) - m_x)/T_x(t)}, \quad (2.26a)$$

$$\rho_x(t) \simeq \left( m_x + \frac{3}{2} T_x(t) \right) n_x(t), \quad (2.26b)$$

$$P_x(t) \simeq T_x n_x(t) \ll \rho_x(t). \quad (2.26c)$$

In the relativistic case, the quantum nature of the particle species becomes obvious by the distinction of fermions and bosons. Also the

Stefan-Boltzmann-like  $\rho \propto T^4$  behavior is recovered. The ideal gas law can be identified in the non-relativistic energy density, where each particle carries a mean energy of  $\langle E_x \rangle = m_x + 3 T_x/2$ . In either case, the entropy density  $s_x(T_x)$  can be calculated using the relation (2.24).

Finally, applying the derived relations  $P_x = \rho_x/3$  and  $P_x \ll \rho_x$  to equation (2.17) for a vanishing collision term and then integrating over time, one can retrieve that  $\rho_{\text{mat}}(t) \propto a^{-3}(t)$  and  $\rho_{\text{rad}}(t) \propto a^{-4}(t)$ , as initially depicted in Figure 2.3.

## 2.3 FINITE-TEMPERATURE EFFECTS IN QUANTUM FIELD THEORY

The dynamics of a QFT is condensed within its tree-level Lagrangian density. While perturbation theory shows to be a useful tool (e. g., when using Feynman diagrams to calculate cross sections for particle interactions described in the Lagrangian density), there exist also non-perturbative solutions of the equations of motion that can be obtained by means of the principle of stationary action. For the case of static fields this reduces to the problem of minimizing the potential energy density defined by the QFT. If the position of the global potential minimum in field space is dependent on temperature, a phase transition can occur.

*Phase transitions are dictated by the stationary action*

Since the fields we are dealing with are quantized, there will be additional contributions to the so-called effective potential next to the tree-level potential term. These temperature-dependent quantum effects can be calculated using thermal field theory. In this section, first, the toolbox of thermal field theory will be introduced by recalling the textbook example of a harmonic oscillator in a thermal bath. The argument is then transferred and generalized to QFT, where it will be argued that the effect of thermal field theory is the introduction of so-called Matsubara sums. Afterwards, we will use the computational techniques from thermal field theory to describe a general recipe for the calculation of the one-loop effective potential of a given particle physics model. The general focus will be more on giving an overview rather than describing particular loop calculations in detail, which can also be found in the existing literature on that topic, see e. g. [26, 27].

### 2.3.1 The quantum harmonic oscillator in a thermal bath

The central object of canonical statistical mechanics is the partition function, from which one can derive all thermodynamic properties of a

system in equilibrium. For a discrete, quantum-mechanical, canonical ensemble with Hamiltonian  $\mathcal{H}$  the partition function is defined as the trace of the Boltzmann factor,  $Z(T) \equiv \text{Tr} [e^{-\beta \mathcal{H}}]$ . The parameter  $\beta \equiv T^{-1}$  denotes the inverse temperature of the bath with which the system is in thermal equilibrium. For the case of a single harmonic oscillator with a frequency  $\omega$ , the partition function reads [28]

*The partition function*

$$Z_{\text{ho}} = \begin{cases} \sum_{n=0}^{\infty} \exp[-\beta \omega (n + \frac{1}{2})] & \text{for bosons} \\ \sum_{n=0}^1 \exp[-\beta \omega (n + \frac{1}{2})] & \text{for fermions} \end{cases} \quad (2.27)$$

$$= \begin{cases} e^{-\beta \omega / 2} (1 - e^{-\beta \omega})^{-1} & \text{for bosons} \\ e^{\beta \omega / 2} (1 + e^{-\beta \omega / 2}) & \text{for fermions .} \end{cases} \quad (2.28)$$

A system whose temperature and volume are kept constant will eventually equilibrate in a state that minimizes its free energy  $F \equiv -T \ln Z(T)$ , as one can show from the second law of thermodynamics. For the harmonic oscillator this implies [28]

*The free energy*

$$F_{\text{ho}} = \begin{cases} \frac{\omega}{2} + T \ln (1 - e^{-\beta \omega}) & \text{for bosons} \\ -\frac{\omega}{2} - T \ln (1 + e^{-\beta \omega}) & \text{for fermions .} \end{cases} \quad (2.29)$$

We can thus see that the free energy of a quantum harmonic oscillator has two components: the first one fixes the ground state energy, being unequal to zero due to Heisenberg's uncertainty principle and independent of the temperature of the connected thermal bath. Its effect is thus completely quantum-mechanical. On the contrary, the second term depends explicitly on temperature and dominates for sufficiently high temperatures. While bosons have positive free energies, the free energy of fermions has a relative negative sign. We will recover qualitatively the same results in thermal field theory after a much longer discussion of the effective potential—in case that one has to again convince oneself that the calculations from QFT do not look too absurd, it can be helpful to come back to this toy example.

*Same contributions as in thermal field theory*

### 2.3.2 Thermal Field Theory

In a canonical ensemble with a Hamiltonian  $\mathcal{H}$  and energy eigenstates  $|n\rangle$ , the expectation value of an operator  $A$  is given by the thermally averaged sum

$$\langle A \rangle_T \equiv \frac{1}{Z} \text{Tr} [e^{-\beta \mathcal{H}} A] , \quad (2.30)$$

where the partition function  $Z$  acts as a normalization factor. The connection between statistical mechanics and QFT emerges when correlation functions are expressed as thermally averaged sums. If one

*Derivation of the  
KMS relation*

takes the two-point function of a quantum field  $\phi$ , one can permute the terms within the trace argument to arrive at the important Kubo-Martin-Schwinger (KMS) relation

$$\begin{aligned}
\langle \phi_{\mathbf{y}}(t) \phi_{\mathbf{x}}(0) \rangle_T &= \frac{1}{Z} \text{Tr} \left[ e^{-\beta \mathcal{H}} \phi_{\mathbf{y}}(t) \phi_{\mathbf{x}}(0) \right] \\
&= \frac{1}{Z} \text{Tr} \left[ \phi_{\mathbf{y}}(t) e^{-\beta \mathcal{H}} e^{i(-i\beta \mathcal{H})} \phi_{\mathbf{x}}(0) e^{-i(-i\beta \mathcal{H})} \right] \\
&= \frac{1}{Z} \text{Tr} \left[ \phi_{\mathbf{y}}(t) e^{-\beta \mathcal{H}} \phi_{\mathbf{x}}(-i\beta) \right] \\
&= \frac{1}{Z} \text{Tr} \left[ e^{-\beta \mathcal{H}} \phi_{\mathbf{x}}(-i\beta) \phi_{\mathbf{y}}(t) \right] \\
&= \langle \phi_{\mathbf{x}}(-i\beta) \phi_{\mathbf{y}}(t) \rangle_T, \\
&= \pm \langle \phi_{\mathbf{y}}(t) \phi_{\mathbf{x}}(-i\beta) \rangle_T, \tag{2.31}
\end{aligned}$$

where in the third line the time evolution  $\phi_{\mathbf{x}}(t) = e^{i\mathcal{H}t} \phi_{\mathbf{x}}(0) e^{-i\mathcal{H}t}$  was used and the final minus sign is for the fermionic case, where the fields  $\phi_{\mathbf{x}}$  and  $\phi_{\mathbf{y}}$  anti-commute [29]. The discovered equation requires a bosonic (fermionic) field  $\phi$  to be symmetric (anti-symmetric) and cyclic in time with the periodicity  $-i\beta$ :  $\phi_{\mathbf{x}}(0) = \pm \phi_{\mathbf{x}}(-i\beta)$ .

*Imaginary time =  
inverse temperature*

Now upon performing a Wick rotation  $t \rightarrow \tau = -it$  (as it is usually done to perform loop integrals in Euclidean space), one can observe that in thermal field theory imaginary time  $\tau$  can be identified with inverse temperature  $\beta$ . This is the (profoundly mysterious) central relationship between QFT and thermodynamics. The main result of this condition is that the time component in integrals of  $n$ -point functions over Euclidean four-momentum space becomes a discrete sum

$$\int \frac{d^4 k_E}{(2\pi)^4} f(k_E) \rightarrow T \sum_n \int \frac{d^3 k}{(2\pi)^3} f(\omega_n, \mathbf{k}) \tag{2.32}$$

over the so-called Matsubara frequencies

$$\omega_n = \begin{cases} 2n\pi T & \text{for bosons} \\ (2n+1)\pi T & \text{for fermions.} \end{cases} \tag{2.33}$$

*The essence of  
thermal field theory*

Thus, to study a field theory at finite temperature, all we have to do is rotate to Euclidean space and impose the correct boundary condition. Computationally, this leads to the following simple prescription for loop calculations: Perform a Wick rotation and replace the  $k_0^E$ -integration by an infinite sum over the Matsubara frequencies  $\omega_n$ . However, this sum often cannot be evaluated trivially. Using the residue theorem and a contour that encircles all the Matsubara poles can then be a very handy trick [27].

### 2.3.3 The effective potential

To illustrate the use of the replacement rule (2.32) in the calculation of an effective potential, consider the Lagrangian density of a complex scalar  $\Phi = (\phi + i\varphi)/\sqrt{2}$  and a Dirac fermion  $\psi$  that are both charged under a U(1) gauge symmetry with the covariant derivative  $D_\mu = \partial_\mu + igA_\mu$  and the corresponding field strength tensor  $B_{\mu\nu} = \partial_\mu A_\nu - \partial_\nu A_\mu$ :

*An exemplary U(1) gauge group*

$$\mathcal{L} = |D_\mu \Phi|^2 - \frac{1}{4} B_{\mu\nu} B^{\mu\nu} + \mu^2 |\Phi|^2 - \lambda |\Phi|^4 + i\bar{\psi} \not{D} \psi - y \Phi \bar{\psi} \psi + \text{h.c.} \quad (2.34)$$

$$\supset \frac{1}{2} (\partial_\mu \phi)^2 + \underbrace{\frac{\mu^2}{2} \phi^2 - \frac{\lambda}{4} \phi^4}_{=-V_{\text{tree}}(\phi)} + \frac{g^2}{2} \phi^2 A_\mu A^\mu + i\bar{\psi} \not{\partial} \psi + g\bar{\psi} \gamma^\mu \psi A_\mu - \frac{y}{\sqrt{2}} \phi \bar{\psi} \psi. \quad (2.35)$$

Since the VEV of  $\Phi$  can always be projected onto the field's real part, the imaginary part of the field can be ignored in the following calculations. The mass spectrum is given by  $m_\phi^2 = 3\lambda\phi^2 - \mu^2$ ,  $m_\varphi^2 = \lambda\phi^2 - \mu^2$ ,  $m_A^2 = g^2\phi^2$  and  $m_\psi^2 = y^2\phi^2/2$ . Requiring the minimum of  $V_{\text{tree}}(\phi)$  to lie at the tree-level VEV  $v = \phi$  gives the additional condition that  $\mu^2 = \lambda v^2$ . We will find that at high temperature the field  $\phi$  will have a vanishing VEV, such that the masses for the gauge boson and the fermion are zero. As the Universe cools,  $\phi$  will acquire its tree-level VEV  $v$  such that  $m_\phi^2 = 2\lambda v^2$ ,  $m_\varphi^2 = 0$ ,  $m_A^2 = g^2 v^2$ , and  $m_\psi^2 = y^2 v^2/2$ . This generation of gauge boson and fermion masses is known as the ‘‘Higgs mechanism’’, which is why the field  $\Phi$  can also be referred to as a Higgs field, even though it is not *the* Higgs field from the SM. We will thus also refer to the real part  $\phi$  of  $\Phi$  as a ‘‘dark Higgs boson’’ in analogy to the Higgs boson from the SM, itself also representing the real part of the corresponding complex scalar field.

*The Higgs mechanism*

A central result of the path integral formulation of a QFT is that the effective potential of the static scalar field generated by its self-interactions can be written as<sup>4</sup>

$$V_{\text{eff},\Phi}^{\ell\text{-loop}}(\phi) = - \sum_{n=0}^{\infty} \frac{\phi^n}{n!} \Gamma_\ell^{(n)}(p=0) \quad (2.36)$$

with the  $n$ -point,  $\ell$ -loop effective vertex  $\Gamma_\ell^{(n)}$  where all external momenta are set to zero [26, 27, 30]. This series represents a sum over all  $n$ -point interactions, where the individual interactions are at  $\ell$ -loop order. If, for example, the effective vertices correspond to the tree-level

<sup>4</sup> Only the potential of the scalar field is of importance here, since non-vanishing VEVs of fermionic or gauge boson fields would break the vacuum's Lorentz invariance. There will, however, of course be contributions to the effective potential from interactions with *all* the coupled fields, hence also from the gauge boson  $A_\mu$  and the fermion  $\psi$ .

The effective potential for  $\ell = 0$  and 1

( $\ell = 0$ ) interactions, the effective potential  $V_{\text{eff}}^{0\text{-loop}}$  is just the tree-level potential  $V_{\text{tree}}$ . If one instead considers interactions up to one-loop order, one obtains a sum over all diagrams with one loop and (in the case of the presented Lagrangian density)  $2n$  external legs. Hence, the 1-loop potential for the toy-Lagrangian given in equation (2.35) is given by

$$V_{\text{eff},\Phi}^{1\text{-loop}}(\phi) = \left[ \phi^2 \text{---} \text{---} \text{---} + \phi^4 \text{---} \text{---} \text{---} + \phi^6 \text{---} \text{---} \text{---} + \dots \right]_{p=0} . \quad (2.37)$$

Here and in the following, external, dashed lines in the Feynman graph indicate the real part  $\phi$  of the propagating dark Higgs field, whereas internal, solid lines depict the complex field  $\Phi$ . Since the  $n$ -th diagram in this resulting series has  $2n$  external legs,  $n$  propagators and symmetry factors of  $1/(2n)$  (for cyclic and anti-cyclic permutation of the vertices) and  $1/2^n$  (for interchanging the external lines at each vertex), the sum can be expressed as

$$V_{\text{eff},\Phi}^{1\text{-loop}}(\phi) = 2i \sum_{n=1}^{\infty} \int \frac{d^4k}{(2\pi)^4} \frac{1}{2n} \left[ \frac{6\lambda\phi^2/2}{k^2 + \mu^2 + i\epsilon} \right]^n . \quad (2.38)$$

The prefactor 2 accounts for the two degrees of freedom of the loop complex scalar. Each vertex contributes a factor  $-6i\lambda$  and each propagator comes with a factor  $i/(k^2 + \mu^2 + i\epsilon)$  [26]. The sum over all diagrams can be evaluated by comparing to the Taylor series of the function  $\ln(1+x)$ . Upon performing a Wick rotation, such that  $k^2 = -k_E^2$ , the effective potential can be written as

$$\begin{aligned} V_{\text{eff},\Phi}^{1\text{-loop}}(\phi) &= \int \frac{d^4k_E}{(2\pi)^4} \ln \left[ 1 + \frac{3\lambda\phi^2}{k_E^2 - \mu^2 - i\epsilon} \right] \\ &= \int \frac{d^4k_E}{(2\pi)^4} \ln \left[ k_E^2 + m_\phi^2(\phi) \right] . \end{aligned} \quad (2.39)$$

The effective one-loop potential for fermions and gauge bosons

One can show that the resulting expressions for contributions from gauge bosons and fermion loops all have a similar form, with the degrees of freedom changed accordingly and a respective negative sign coming from fermionic loops [27]. The combined expression thus reads

$$V_{\text{eff}}^{1\text{-loop}}(\phi) = \sum_x \frac{\eta_x n_x}{2} \int \frac{d^4k_E}{(2\pi)^4} \ln \left[ k_E^2 + m_x^2(\phi) \right] , \quad (2.40)$$

Adding a thermal bath

where  $\eta_x = +1$  ( $-1$ ) for bosons (fermions). The effect of embedding the quantum fields in a thermal environment with temperature  $T$  now sets periodic boundaries to the integral over imaginary time. Applying the replacement rule (2.32) yields

$$V_{\text{eff}}^{1\text{-loop}}(\phi, T) = \sum_x \frac{\eta_x n_x T}{2} \sum_n \int \frac{d^3k}{(2\pi)^3} \ln \left[ \omega_n^2 + \mathbf{k}^2 + m_x^2 \right]$$

$$\begin{aligned}
 &= \sum_x \frac{\eta_x n_x T}{2} \sum_n \int \frac{d^3k}{(2\pi)^3} \int dm_x^2 \frac{1}{\omega_n^2 + \omega_x^2} \\
 &= \sum_x \frac{\eta_x n_x}{2} \int \frac{d^3k}{(2\pi)^3} \int dm_x^2 \left[ \frac{1}{2\omega_x} + \frac{1}{\omega_x} \frac{\eta_x}{e^{\beta\omega_x} - \eta_x} \right] \\
 &= \sum_x \eta_x n_x \int \frac{d^3k}{(2\pi)^3} \left[ \frac{\omega_x}{2} + T \ln \left( 1 - \eta_x e^{-\beta\omega_x} \right) \right] \\
 &= V_{\text{eff}}^{1\text{-loop}}(\phi, T = 0) + V_{\text{eff}}^{1\text{-loop}}(\phi, T > 0). \quad (2.41)
 \end{aligned}$$

To simplify the Matsubara sum, the derivative of the expression in the integral with respect to  $m_x^2$  was taken and re-integrated after the sum has been calculated. Further, the variable  $\omega_x^2 \equiv \mathbf{k}^2 + m_x^2$  has been introduced to shorten the notation. One ends up with an integral over the 3-momentum space of a temperature-independent and a temperature-dependent term that remind of the free energy of a simple harmonic oscillator in a thermal bath. Therefore, the presented temperature-dependent, effective 1-loop potential  $V_{\text{eff}}^{1\text{-loop}}(\phi, T)$  can be interpreted as being analogous to the vacuum energy density of a quantum harmonic oscillator in a thermal bath, while the tree-level potential  $V_{\text{tree}}(\phi)$  is just the classical energy density contained in a background field  $\phi$  [26].

*Recovering the  
harmonic oscillator*

In fact, the dynamic nature of the field can be made mathematically clear by splitting it into a classically moving field  $\phi_c$  and a dynamical part  $\phi_d$ : While  $\phi_d$  fluctuates around the potential minimum,  $\phi_c$  is the background field that is just the VEV of the potential. Hence, the field-dependent masses  $m_x^2(\phi)$  should rather be called “VEV-dependent masses” and depend on  $\phi_c$  and not on  $\phi_c + \phi_d$ . However, one conventionally drops the subscript “c”. In any case, this mass works as a measure of the parabolicity of the tree-level potential at its minimum and thus dictates the frequency of oscillation of the quantum field  $\phi_d$  as it is described by the Klein-Gordon equation.

#### 2.3.4 Treatment of the effective potential's divergences

Before replacing the infinite sum over the number of external legs in equation (2.38), the integral diverges due to the diagrams with two and four external legs. Thus, the potential given in (2.41) is still ultraviolet (UV) divergent. Another breakdown of perturbativity can be predicted by the mere existence of two energy scales  $\mu$  and  $T$  within the second, temperature-dependent term [31]. Whereas the first divergences can be treated with the simple regularization of the integral and the introduction of counterterms, the latter case is more involved. Several procedures to deal with the resulting UV and infrared (IR) divergences have been described in the pertinent literature [32]. Moreover, one finds that higher loop-order effects

*UV and IR  
divergences in the  
effective potential*

dominate at temperatures around phase transitions. What can be done to take account of these peculiarities, is the resummation of so-called daisy diagrams. More accurate results could be obtained using computationally more advanced lattice QFT procedures [33]. Since our focus lies on the investigation of new effects concerning phase transitions in hot dark sectors rather than on precision calculations, we will stick with the resummation of daisy diagrams.

### 2.3.4.1 The Coleman-Weinberg contribution

The effective potential at  $T = 0$  can be shown to be equivalent to

$$\begin{aligned} V_{\text{eff}}^{1\text{-loop}}(\phi, T = 0) &= \sum_x \eta_x n_x \int \frac{d^3k}{(2\pi)^3} \frac{\omega_x}{2} \\ &= \sum_x \frac{\eta_x n_x}{2} \int \frac{d^4k_E}{(2\pi)^4} \ln [k_E^2 + m_x^2(\phi)] \end{aligned} \quad (2.42)$$

*Regularization of the  
Coleman-Weinberg  
potential*

by using the identity  $\omega/2 = \int_{-i\infty}^{+i\infty} dk \ln(k^2 + \omega^2) / (2\pi)$  [26]. The resultant UV divergent integral can be regularized dimensionally by formally shifting the dimension of the integral to  $4 - \epsilon$ . In doing so, the singularities will be isolated into terms  $\propto 1/\epsilon$ , which will be canceled upon the introduction of finite counterterms  $V_{\text{ct}}$ . The regularized one-loop potential for vanishing temperature eventually reads

$$V_{\text{CW}}(\phi) = \sum_x \eta_x n_x \frac{m_x^4(\phi)}{64\pi^2} \left[ \ln \frac{m_x^2(\phi)}{\Lambda^2} - C_x \right] \quad (2.43)$$

with  $C_x$  being equal to  $3/2$  ( $5/6$ ) for scalars and fermions (gauge bosons) [27]. Note that the renormalization scale  $\Lambda$  can be absorbed into a redefinition of the quartic coupling  $\lambda$  of a given QFT. In that sense the choice of  $\Lambda$  is arbitrary. Conventionally, the Higgs field's VEV  $v$  is chosen as a reference scale. The counterterms can be imposed by the renormalization conditions  $0 = \partial_\phi (V_{\text{CW}} + V_{\text{ct}})|_{\phi=v}$  and  $0 = \partial_\phi^2 (V_{\text{CW}} + V_{\text{ct}})|_{\phi=v}$ , effectively ensuring that the VEV and  $m_\phi$  remain unchanged with respect to the tree-level potential.

### 2.3.4.2 Hard thermal loops and daisy resummation

To understand the divergences of the  $T > 0$  contributions, consider the 1-loop corrections to the scalar and gauge boson propagator defined by the Lagrangian density in equation (2.35). These contributions are referred to as ‘‘hard thermal loops’’ and are listed in Figure 2.5. Just as before, their individual contributions can be calculated by applying the replacement rule from (2.32). They eventually each include a UV divergent term and a temperature-dependent term, which acts as an

(a)

(b)

(c)

(d)

(e)

**Figure 2.5:** The hard thermal loops for the scalar (a, b, and c) and the U(1) gauge boson (d and e) defined in equation (2.35). Note that only longitudinally polarized gauge bosons receive Debye masses and that the values are approximated in the regime  $T \gg m_x$ , where  $m_x$  is the mass of the particle constituting the loop. The prefactors account for the degrees of freedoms (DOFs) of the loop particle.

additional mass term in the propagator. Since the process in which these masses are generated is analogous to Debye screening, the polarization of plasmas and electrolytes leading to the screening of electrical charges, these masses are called “Debye masses”. An explicit calculation of them yields the values written next to the individual Feynman diagrams in Figure 2.5 [26]. As fermions will not contribute with their Debye masses to the effective potential, the respective diagrams are not of importance here.

*Debye masses and hard thermal loops*

To now see where the aforementioned IR divergences in the thermal corrections come from, consider the so-called “daisy diagram”

$$\sim \frac{(\lambda T) (\lambda T^2)^{N-1}}{\mu^{2N-3}} = \lambda^N \frac{T^{2N-1}}{\mu^{2N-3}} = \alpha^{N-3/2} \lambda^{3/2} T^2, \quad (2.44)$$

where in the last step the effective coupling  $\alpha \equiv \lambda T^2 / \mu^2$  has been introduced. The temperature dependence of the daisy diagram can be determined by dimensional analysis, i. e. by counting its superficial degrees of divergence, which are given by

$$D = 4 \# \text{loops} - 2 \# \text{boson prop.} - \# \text{fermion prop.} \quad (2.45)$$

due to the respective powers of the loop momentum occurring when adding a loop, a boson propagator or a fermionic propagator to a diagram. One can further see that a diagram scales as  $T^{\max(1,D)}$ , since every loop diagram has to be at least linear in  $T$  because of the prefactor in front of the Matsubara sum in (2.32) [31]. By this argument, it can also be understood why the hard thermal loops in Figure 2.5 are all proportional to  $T^2$ . The shown daisy diagram with  $N$  total loops hence scales in dependence of  $T$  as it is given in (2.44), where the factor  $\mu^{2N-3}$  fixes dimensionality. Close to a phase transition, when  $T \sim \mu/\sqrt{\lambda}$  such that the mass contributions  $-\mu^2$  and  $\lambda T^2$  cancel,  $\alpha \sim 1$  and the corrections by daisy diagrams scale as  $\Pi_{\text{daisy}} \sim \lambda^{3/2} T^2$ . This is in sharp contrast to the expected result from the perturbation series of a QFT at  $T = 0$ , since these corrections do not recede with increasing loop order.

*The breakdown of perturbativity in daisy graphs*

An explicit calculation of the shown daisy diagram for  $T \gg m_\phi$  yields

$$\begin{aligned} \Pi_{\text{daisy}} \sim & T \underbrace{\sum_n \int_0^\infty \frac{dk}{2\pi^2} \frac{k^2}{(\omega_n^2 + k^2)^{N-1}}}_{\text{main loop}} \\ & \times \underbrace{\left[ T \sum_n \int_0^\infty \frac{dk}{2\pi^2} \frac{k^2}{\omega_n^2 + k^2} \right]^{N-1}}_{\text{petals}}. \end{aligned} \quad (2.46)$$

One can see that the main loop is IR divergent as soon as  $N > 2$  when  $\omega_n = 0$ , which can only occur in bosonic daisy diagrams. This is the origin of the breakdown of perturbativity in the daisy diagram shown in (2.44) and the reason why fermion Debye masses had not have to be calculated before [26].

To now account for the effect of the daisy diagrams, the propagators for bosons with tree-level mass  $m(\phi)$  have to be resummed by adding up propagators with an increasing number of hard thermal loops with Debye mass  $\Pi(T)$ :

*Daisy resummation techniques*

$$\frac{1}{p^2 - m^2} + \frac{\Pi(T)}{(p^2 - m^2)^2} + \frac{\Pi^2(T)}{(p^2 - m^2)^3} + \dots = \frac{1}{p^2 - m^2 - \Pi(T)}, \quad (2.47a)$$

$$\text{---} + \text{---} \circ \text{---} + \text{---} \circ \circ \text{---} + \dots = \text{---} \bullet \text{---}, \quad (2.47b)$$

which can be shown using a geometric sum. The infinite sum hence results in the replacement

$$m^2(\phi) \rightarrow m^2(\phi) + \Pi(T) \quad (2.48)$$

in the effective potential for  $T > 0$  in (2.41) which dresses each of the boson loop propagators, such that they now effectively include

daisy contributions. This is referred to as the ‘‘Parwani method’’ [34, 35] or as ‘‘truncated full dressing’’, as opposed to ‘‘full dressing’’ where the Debye masses are not calculated in the high-temperature approximation, but in full generality [31]. However, in either case temperature-dependent counterterms would now be required, which is against physical intuition as it connects the UV with the IR regime [32]. What is often done to spare the calculation of these additional counterterms is to restrict the resummation only to the dominant bosonic zero-mode of the Matsubara sum like

$$\begin{aligned}
V_{\text{eff},\Phi}^{1\text{-loop}}(\phi, T > 0) &\rightarrow \frac{T}{2} \sum_{n \neq 0} \int \frac{d^3k}{(2\pi)^3} \ln [\omega_n^2 + \mathbf{k}^2 + m^2(\phi)] \\
&\quad + \frac{T}{2} \int \frac{d^3k}{(2\pi)^3} \ln [\mathbf{k}^2 + m^2(\phi) + \Pi(T)] \\
&= \frac{T}{2} \sum_n \int \frac{d^3k}{(2\pi)^3} \ln [\omega_n^2 + \mathbf{k}^2 + m^2(\phi)] \\
&\quad + \frac{T}{2} \int \frac{d^3k}{(2\pi)^3} \ln \left[ 1 + \frac{\Pi(T)}{\mathbf{k}^2 + m^2(\phi)} \right] \\
&= V_{\text{eff},\Phi}^{1\text{-loop}}(\phi, T > 0) + V_{\text{daisy},\Phi}(\phi, T), \quad (2.49)
\end{aligned}$$

where a new term has been isolated that can be rewritten as [36]

$$V_{\text{daisy},\Phi} = -\frac{T}{12\pi} \left[ (m^2(\phi) + \Pi(T))^{3/2} - (m^2(\phi))^{3/2} \right]. \quad (2.50)$$

This procedure is known as the ‘‘Arnold-Espinoza’’ method for resumming daisy diagrams and will also be used in this thesis [35, 37]. It has been checked that both procedures yield numerically similar, but not equivalent results<sup>5</sup>.

### 2.3.4.3 The cancellation of the potential barrier

The effective potential now includes all relevant effects to study phase transitions. A great simplification, however, can still be made by rewriting the original temperature-dependent part (without resummed daisy diagrams) as

$$\begin{aligned}
V_T(\phi, T) &\equiv V_{\text{eff}}^{1\text{-loop}}(\phi, T > 0) \\
&= T \sum_x \eta_x n_x \int \frac{d^3k}{(2\pi)^3} \ln \left( 1 - \eta_x e^{-\beta \omega_x} \right)
\end{aligned}$$

<sup>5</sup> It should further be noted that both the Parwani and the Arnold-Espinoza method are rather crude approximations and cannot be easily generalized to non-Abelian gauge theories. A precise calculation of the effective potential would thus require the use of more modern techniques which include for example a resummation of Goldstone modes, a proper treatment of gauges and higher-loop (called ‘‘sunset’’, ‘‘lollipop’’ and ‘‘super-daisy’’) diagrams. These diagrams do not have a decreasing importance with an increasing number of loops either and should therefore also be resummed [31].

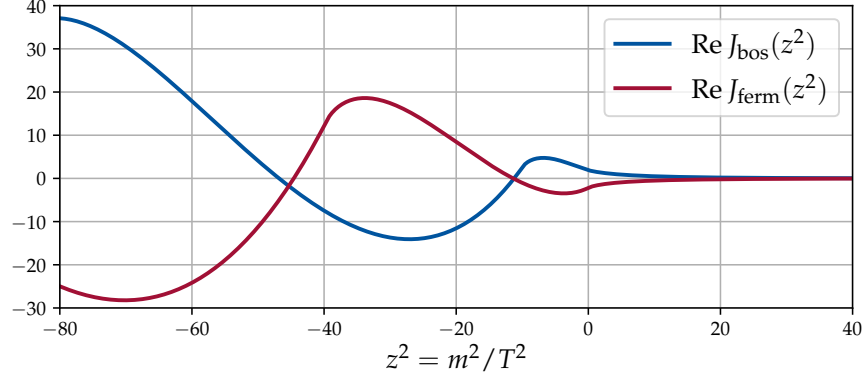


**Figure 2.6:** The real part of the thermal functions  $J_{\text{bos}}(z^2)$  and  $J_{\text{ferm}}(z^2)$ .

$$= \frac{T^4}{2\pi^2} \sum_x \eta_x n_x J_{\eta_x} \left( \frac{m_x^2(\phi)}{T^2} \right) \quad (2.51)$$

with the thermal functions

$$J_{\eta_x}(z^2) \equiv \int_0^\infty dy y^2 \ln \left[ 1 - \eta_x \exp \left( -\sqrt{y^2 + z^2} \right) \right]. \quad (2.52)$$

A plot of the thermal functions for positive and negative values of  $z^2$  can be found in Figure 2.6. For decreasing temperature, i. e. for  $z^2 \rightarrow \infty$ , the impact of the thermal functions vanishes, while for high temperatures, i. e. for  $z^2 \rightarrow 0$ , their effect gets non-negligible. The behavior for negative  $z^2$  is relevant since the complex scalar field will acquire an imaginary mass for field values where the system is unstable, i. e. where the effective potential has a negative curvature. This instability also becomes manifest in the thermal function developing an imaginary component, which is also the case for the daisy contributions in equation (2.50). The hypothetical particle that fulfills this unstable vacuum configuration is referred to as a “tachyon” as it would travel faster than light. An in-depth study of the occurrence of an imaginary component in the effective potential can be found in [32].

In the high-temperature regime  $T \gg m(\phi)$ , the thermal functions and the daisy potential term can be approximated as [27]

$$J_{\text{bos}}(z^2) \approx -\frac{\pi^4}{45} + \frac{\pi^2}{12} z^2 - \frac{\pi}{6} z^3 - \frac{z^4}{32} \ln(z^2) + \text{const}, \quad (2.53a)$$

$$J_{\text{ferm}}(z^2) \approx \frac{7\pi^4}{360} - \frac{\pi^2}{24} z^2 - \frac{z^4}{32} \ln(z^2) + \text{const}, \quad (2.53b)$$

$$\begin{aligned} V_{\text{daisy},\Phi} &\approx -\frac{T^4}{12\pi} \left[ \left( \frac{\Pi}{T^2} \right)^{3/2} + \frac{3}{2} \sqrt{\Pi} \frac{m^2(\phi)}{T^2} - \left( \frac{m^2(\phi)}{T^2} \right)^{3/2} \right] \\ &\supset \frac{T^4}{12\pi} \left( \frac{m^2(\phi)}{T^2} \right)^{3/2}. \end{aligned} \quad (2.53c)$$

The most important result of this comparison is that only bosonic degrees of freedom that are coupled to  $\phi$  contribute a term that scales as  $z^3$ . This term can thermally induce a barrier between competing potential minima, driving a possible transition into the first-order regime (as will be illustrated in the following section 2.4). The expansion of the daisy potential, however, reveals another term that scales as  $z^3$  and shows to have the same prefactor as the contribution from  $J_{\text{bos}}$  multiplied with  $T^4/(2\pi^2)$ , but carries a relative minus sign. The daisy term thus cancels the cubic terms and the thermally induced barrier! What eventually saves the first-order phase transition is that only longitudinally polarized gauge bosons receive Debye masses, such that the induced barriers by transverse modes survive. Therefore, in general, scalar fields with gauge charges are required to achieve first-order transitions when the barrier should be induced thermally. Otherwise, without gauge charges, the scalar would not couple with the gauge field, which therefore could not contribute the thermally induced barrier to the effective potential. One should note, however, that this is only a necessary condition since dominant tree-level effects (in the U(1) model controlled by  $\lambda$ ) can always dominate, making the barrier small in comparison [26].

*Avoiding the cancellation of a potential barrier*

#### 2.3.4.4 Summary

Summing over all the different contributions that have been considered, the general, 1-loop effective potential of an abelian QFT with daisies resummed using the Arnold-Espinoza procedure can be written as [26]

*An overview over all contributions*

$$V_{\text{eff}}^{1\text{-loop}}(\phi, T) = V_{\text{tree}} + V_{\text{CW}} + V_{\text{ct}} + V_T + V_{\text{daisy}} \quad (2.54)$$

with the individual contributions

$$V_{\text{CW}}(\phi) = \sum_x \eta_x n_x \frac{m_x^4(\phi)}{64\pi^2} \left[ \ln \frac{m_x^2(\phi)}{\Lambda^2} - C_a \right], \quad (2.55a)$$

$$V_T(\phi, T) = \frac{T^4}{2\pi^2} \sum_x \eta_x n_x J_{\eta_x} \left( \frac{m_x^2(\phi)}{T^2} \right), \quad (2.55b)$$

$$V_{\text{daisy}}(\phi, T) = -\frac{T}{12\pi} \sum_b n_b^L \left[ (m^2(\phi) + \Pi(T))_b^{3/2} - (m^2(\phi))_b^{3/2} \right], \quad (2.55c)$$

where  $n_x$  are the degrees of freedom of the fields coupled to  $\phi$ ,  $n_b^L$  are the longitudinal boson components thereof,  $\eta_x$  is  $+1$  ( $-1$ ) for bosons (fermions),  $\Lambda$  is the renormalization scale, which will be set to the tree-level VEV  $v$  of  $\phi$ ,  $C_x = 3/2$  are the renormalization constants for scalars and fermions while  $C_x = 5/6$  holds for gauge bosons, and  $J_{\eta_x}$  are the thermal functions as defined in equation (2.52). Further, Goldstone

modes have to be counted in addition<sup>6</sup> to the longitudinal gauge boson DOFs and generally, the expression  $(m^2(\phi) + \Pi(T))_b^{3/2}$  has to be understood as the  $b$ -th eigenvalue of the temperature-dependent mass matrix.

*Counterterms*

For a Lagrangian of a complex scalar field as in (2.35), the counterterm potential is given analogously to the tree-level potential by

$$V_{\text{ct}}(\phi) = -\frac{\delta\mu^2}{2}\phi^2 + \frac{\delta\lambda}{4}\phi^4, \quad (2.56)$$

where the counter-mass  $\delta\mu^2$  and the counter-coupling  $\delta\lambda$  can be calculated using

$$\delta\mu^2 = \left[ \frac{3}{2\phi} \frac{dV_{\text{CW}}(\phi)}{d\phi} - \frac{1}{2} \frac{d^2V_{\text{CW}}(\phi)}{d\phi^2} \right] \Big|_{\phi=\Lambda}, \quad (2.57a)$$

$$\delta\lambda = \left[ \frac{1}{2\phi^3} \frac{dV_{\text{CW}}(\phi)}{d\phi} - \frac{1}{2\phi^2} \frac{d^2V_{\text{CW}}(\phi)}{d\phi^2} \right] \Big|_{\phi=\Lambda}. \quad (2.57b)$$

## 2.4 FIRST-ORDER PHASE TRANSITIONS IN THE EARLY UNIVERSE

In this section we want to apply the introduced methods of thermal field theory to study phase transitions in the early Universe and show how bubbles of a new phase can emerge and expand in the hot primordial plasma. The Lagrange density presented in (2.35) without the fermion  $\psi$  is almost that of the DS model that will be introduced in chapter 4. Without the fermionic interactions, the Debye masses are given by  $\Pi_\Phi(T) = \left(\frac{\lambda}{3} + \frac{g^2}{4}\right) T^2$  and  $\Pi_A^L = \frac{g^2}{3} T^2$  (see Figure 2.5). The resulting effective potential is depicted in Figure 2.7 for a range of temperatures. While for high temperatures, the minimum of the potential and hence also the VEV is fixed to  $\phi = 0$ , at lower temperatures the VEV shifts to non-vanishing values and reaches the tree-level VEV  $\phi = v$  at  $T = 0$ .

*Restoring symmetry at high temperatures*

The breaking of symmetry can be understood qualitatively by comparing the tree-level potential terms which are  $\propto \phi^2$  and  $\propto \phi^4$  to the leading terms  $\propto z^2$  in the high-temperature approximation of  $J_{\text{bos}}(z^2)$  in (2.52). For high temperatures, the leading term in  $V_T(\phi)$  thus scales as  $\propto m^2(\phi) T^2 \propto \phi^2 T^2$ , which will eventually dominate over the tree-level potential for sufficiently high temperatures, yielding an approximately parabolic minimum at  $\phi = 0$ . When the temperature falls due to the expansion of the Universe, the thermal effects become less

<sup>6</sup> Even though this sounds as if degrees of freedom would be double-counted, this is not the case as it was argued in [32].

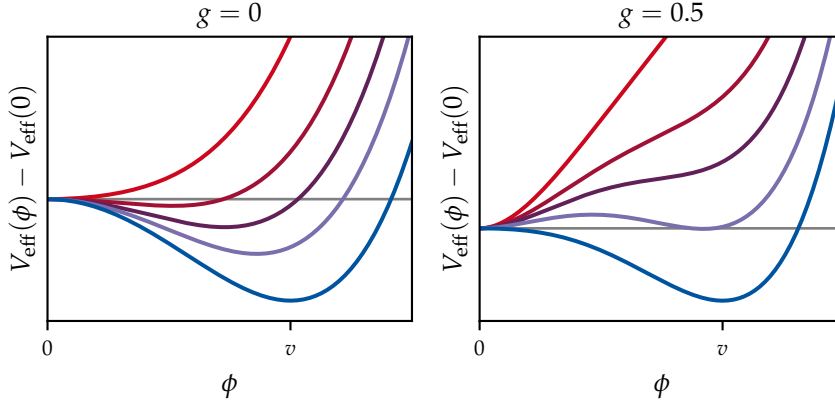


**Figure 2.7:** A comparison of the effective potential (2.54) for a complex scalar charged under the  $U(1)$  gauge group defined in (2.35) for a series of decreasing temperatures (red to blue curves) and different gauge couplings. The quartic coupling is set to  $\lambda = 1.5 \cdot 10^{-3}$  and the contributions from the fermion are neglected. For a vanishing gauge coupling  $g$  (left), the potential allows only for crossovers. For  $g = 0.5$  (right), a potential barrier forms, thus permitting FOPTs. The blue curves correspond to the zero-temperature effective potentials, while for the red curves  $T = 2v$  (left) and  $T = 0.3v$  (right) have been used.

important and, eventually, the tree-level potential dominates, breaking the underlying gauge symmetry spontaneously<sup>7</sup>.

The transition from one minimum to another can occur in two different fashions: continuously or discontinuously, as depicted in Figure 2.7 for  $g = 0$  and  $g = 0.5$ , respectively. Note that the formation of a thermally induced barrier can only happen if the gauge coupling does not vanish as has been argued in section 2.3: For  $g = 0.5$ ,  $V_{\Gamma}$  includes terms  $\propto z^3$  for all bosons coupled to  $\phi$ , i. e.  $\phi$  itself and the gauge boson. Out of these, only the contribution from the transversal gauge boson mode survives after having added  $V_{\text{daisy}}$  to the effective potential due to the aforementioned cancellation. In the  $g = 0$  case, the only contribution to a potential barrier comes from the complex scalar, which gets canceled exactly when including daisy diagrams. Thus, without a coupled gauge boson to the Higgs field, no thermal barrier can form and the field just rolls down to its new VEV. In the opposite case, the gauge coupling induces a thermal barrier through which the field has to tunnel to its new VEV. The objective of this section is to explain how to calculate the temperature at which this so-called first-order phase transition (FOPT) happens.

*First-order phase transitions*

<sup>7</sup> Turning this argument around, the restoration of symmetry at high temperatures, being a robust result of thermal field theory, can be seen as the fundamental reason for why people search for more symmetric theories with large gauge groups in which one can embed the SM.

*The critical temperature  $T_c$*

The temperature at which the minimum at  $\phi = 0$  degenerates due to the existence of a second minimum at  $\phi \neq 0$  of the same depth is referred to as the “critical temperature”  $T_c$  of an FOPT (see also the lower purple curve in 2.7 for  $g = 0.5$ ) [28]. Below this temperature, the Universe is trapped in the formerly global minimum, which is now a local one. The new global minimum is called the “true vacuum” or the “broken phase”. As long as there has not been a transition to the new vacuum state, the old minimum is referred to as being “super-cooled”. This term is used since a state with a lower free energy would exist, whereas the field is trapped in the old, energetically disfavored vacuum state<sup>8</sup>. Generally, as in the study of classical FOPTs, a system that is super-cooled more strongly will lead to a more violent phase transition [28]. This is the reason why high potential barriers will be favored for the production of GWs, as will be described in detail in section 2.5.

*The nucleation temperature  $T_n$*

The temperature at which the scalar field eventually tunnels to the true vacuum state and therewith ends the super-cooling is referred to as the “nucleation temperature”  $T_n \in [0, T_c]$ , which marks the onset of an FOPT. Already above this temperature, bubbles of the new phase form, but collapse immediately. Only below this temperature, the nucleating bubbles are large enough such that they can expand and permeate the Universe with the new phase. The existence of such a threshold radius can be understood in analogy to conventional thermodynamics: The potential energy of a bubble with radius  $r$  in a super-cooled liquid is proportional to  $-r^3$ , while its surface tension goes with  $+r^2$ . Hence, the bubble growth can only occur once the potential energy difference between the old and the new phase can account for sufficiently large bubbles [39]. An FOPT in cosmology now describes the formation of bubbles with non-zero VEVs of a scalar field in the hot plasma of the primordial Universe<sup>9</sup>.

The formation of bubbles can be understood quantitatively by considering the Euclidean action [42]

$$S[\phi] = \int d^4x_E \left[ \frac{1}{2} \left( \frac{\partial \phi}{\partial \tau} \right)^2 + \frac{(\nabla \phi)^2}{2} + V_{\text{eff}}(\phi) \right] \quad (2.58)$$

of the Higgs field  $\phi$ . Using the principle of extremal action, the Klein-Gordon equation in presence of a classical potential

$$\frac{\partial^2 \phi}{\partial \tau^2} + \Delta \phi = \frac{dV_{\text{eff}}}{d\phi} \equiv V'_{\text{eff}}(\phi) \quad (2.59)$$

<sup>8</sup> Under the right circumstances, a long enough period of super-cooling can lead to an intermediate phase of vacuum domination and inflation, possibly yielding other interesting effects for BSM physics [38].

<sup>9</sup> Note that there exist also more complex phase transitions with intermediate phases and more scalar fields [40, 41]. We will focus on the case with only one scalar with an initially vanishing VEV and one phase transition.

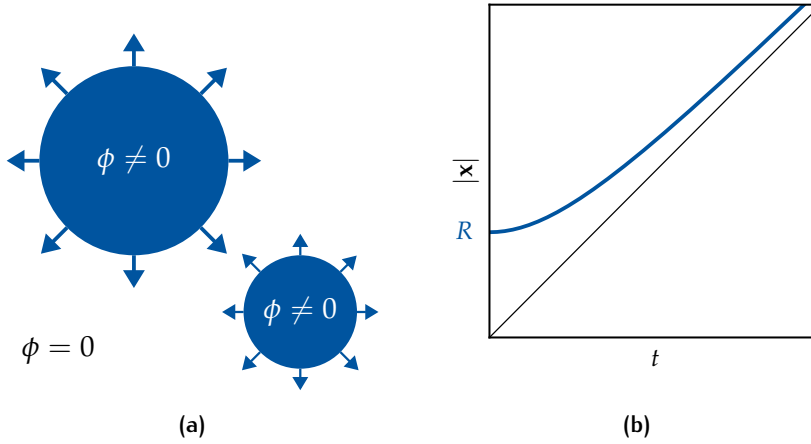


**Figure 2.8:** The nucleation and expansion of bubbles. *Left:* Sketch of the simultaneous nucleation of bubbles in which  $\phi \neq 0$  at different positions in the Universe. *Right:* Only bubbles larger than a critical size can expand. The Bubble wall accelerates towards the speed of light.

with the boundary conditions  $\phi(\rho \rightarrow \infty) \rightarrow 0$  and  $\phi'(\rho = 0) = 0$  is obtained, where  $\rho \equiv \sqrt{\tau^2 + \mathbf{x}^2}$ . Typically, the solutions of this PDE are  $O(4)$ -symmetric. Therefore, the equation of motion can be simplified to

$$\frac{d^2\phi}{d\rho^2} + \frac{3}{\rho} \frac{d\phi}{d\rho} = V'_{\text{eff}}(\phi). \quad (2.60)$$

This is the so-called “bounce equation”, which can be solved numerically using a shooting algorithm, resulting in the profile  $\phi(\rho)$  of a bubble wall. For  $O(4)$ -symmetric “bounce solutions” in Euclidean space, the bubbles form spheres with a radius  $\rho = R$  with a corresponding radius  $r = |\mathbf{x}| = \sqrt{R^2 + c^2 t^2}$  in the three-dimensional space. This radius can be interpreted as the radial distance from the bubble center at which the field value drops to a specific value, e. g. half the VEV. The time dependence of the profile describes a bubble with an initial radius  $R$  that expands subsequently with a bubble wall velocity that reaches the speed of light. A schematic plot of how bubbles nucleate and expand can be found in Figure 2.8.

*The bounce equation*

As we are dealing with a field  $\phi$  in a thermal bath, the effective potential  $V_{\text{eff}}(\phi, T)$  is also a function of the bath’s temperature and the KMS relation holds, which states that  $\phi$  is periodic in the imaginary time  $\tau$  with the frequency  $T^{-1}$ . Consequentially, the integral over imaginary time reduces to  $T^{-1}$  [39, 43] such that thermal tunneling can be described by the Euclidean action

*Thermal tunneling*

$$S[\phi, T] = \frac{S_3[\phi, T]}{T} = \frac{1}{T} \int d^3x \left[ \frac{(\nabla\phi)^2}{2} + V_{\text{eff}}(\phi, T) \right], \quad (2.61)$$

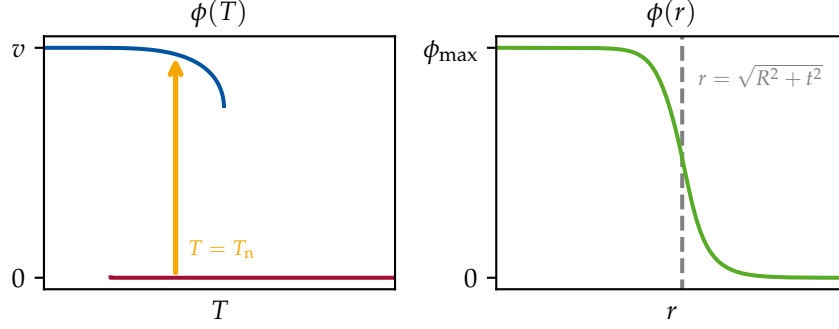


**Figure 2.9:** *Left:* Temperature dependence of the two minima of  $V_{\text{eff}}(\phi, T)$ . For sufficiently high temperatures, there is only the symmetric phase  $\phi = 0$  (red); as the Universe cools down, a second minimum (blue) appears. When  $T = T_n$ , bubbles nucleate in which  $\phi \neq 0$ . *Right:* Profile of a bubble as a function of the distance  $r$  to the bubble center. The field value decreases from  $\phi = \phi_{\text{max}} > 0$  within the bubble to  $\phi = 0$  outside of the bubble. For  $T \rightarrow 0$ , the maximal field value inside the bubble reaches the tree-level VEV  $\phi_{\text{max}} \rightarrow v$ , as can also be seen in the  $\phi(T)$  plot on the left.

which, upon imposing stationarity and  $O(3)$ -symmetric solutions, yields the bounce equation

$$\frac{d^2\phi}{dr^2} + \frac{2}{r} \frac{d\phi}{dr} = V'_{\text{eff}}(\phi, T) \quad (2.62)$$

with the boundary conditions  $\phi(r \rightarrow \infty) \rightarrow 0$  and  $\phi'(r=0) = 0$ . A plot of the competing VEVs in dependence of the bath's temperature and a generic bubble profile  $\phi(r)$  as a solution for the temperature-dependent bounce equation can be found in Figure 2.9.

*Calculation of the nucleation temperature  $T_n$*

To calculate the nucleation temperature numerically, one compares the bubble nucleation rate  $\Gamma(T) = \mathcal{A}(T) \exp(-S_3(T)/T)$ , where the solution  $\phi(r)$  of the bounce equation at a given temperature  $T$  was inserted into  $S_3[\phi, T]$  and  $\mathcal{A}(T) \sim T^4$  for dimensional reasons, to the Hubble volume  $H^{-3}(T)$ . The quantity  $S_3(T)/T$  is conventionally referred to as “the bounce action”. The condition, that the integrated number of bubbles since the end of inflation per Hubble volume is  $\mathcal{O}(1)$ , yields comparable results to the the conventionally used, computationally simpler nucleation condition  $\Gamma(T_n) H^{-4}(T_n) = 1$  [26]. The latter evaluates to

$$\left. \frac{S_3(T)}{T} \right|_{T=T_n} \sim 146 - 2 \ln \left( \frac{g_{\text{eff},\rho}^{\text{tot}}(T_n)}{100} \right) - 4 \ln \left( \frac{T_n}{100 \text{ GeV}} \right), \quad (2.63)$$

where  $g_{\text{eff},\rho}^{\text{tot}}(T)$  is the number of effective relativistic DOFs in the Universe at a temperature  $T$ , on which the Hubble parameter  $H^2(T) =$

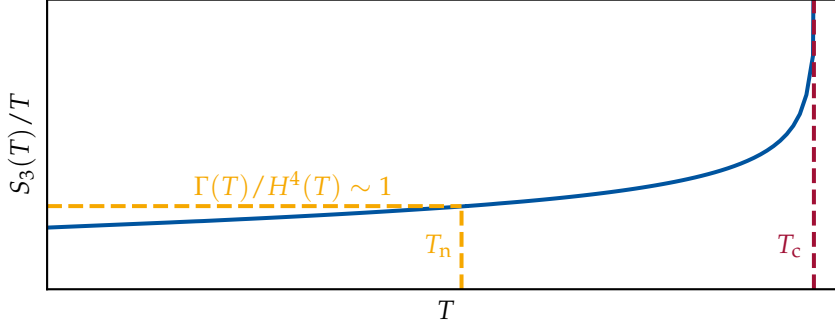


**Figure 2.10:** Plot of the Euclidean bounce action  $S_3(T)/T$  for a range of temperatures. At  $T_c$ , the bounce action diverges, rendering the transition rate  $\Gamma(T) \propto \exp[-S_3(T)/T]$  infinitely small. This is due to the vanishing of the difference in free energy (or, equivalently potential energy density) between the old and the new vacuum state, which makes the transition from one minimum to the other energetically disfavored [44]. For  $T = T_n$ , the bubble nucleation becomes so frequent that one bubble per Hubble volume can form.

$\frac{\pi^2}{30} g_{\text{eff},\rho}^{\text{tot}}(T) T^4$  depends [12]. A thorough definition of  $g_{\text{eff},\rho}^{\text{tot}}(T)$  will be given in chapter 3. To calculate the nucleation temperature of a given FOPT numerically, one thus has to find the temperature where the difference between the left- and right-hand side of (2.63) is minimized, calculating at each iteration the numerically expensive bounce action  $S_3(T)/T$ . A plot of the bounce action for the effective potential discussed in the last section 2.3 can be found in Figure 2.10.

The discussion of FOPTs is now finished: We found that the stationary action principle dictates phase transitions in which bubbles emerge into the hot primordial plasma due to the existence of competing minima in the effective 1-loop potential of a Higgs field coupled to a gauge field. Until now, however, the emission of gravitational waves had not been important, since the bubbles are spherically symmetric and expand likewise. This changes when bubbles of the new phase collide, as will be shown. The following section is aimed at explaining how GWs can be emitted in this process and how we can describe their resulting spectra.

## 2.5 GRAVITATIONAL WAVES FROM PHASE TRANSITIONS

In this section, we will first discuss how Einstein's GR predicts gravitational radiation and what its properties and some of its peculiarities

are. Using either some renormalization technique or Noether's theorem, it will then be possible to define consistently the energy and momentum of gravitational waves in chapter 2.5.2. With the knowledge of how to compute the energy density of a monochromatic wave, we will turn to the superposition of waves to a stochastic background in 2.5.3. In 2.5.4, the mechanism of production of such a background from the leftovers of a primordial FOPT will be examined. Ultimately, in 2.5.5, the detection of SGWBs will be described and a measure for a signal-to-noise ratio (SNR) will be provided. This measure will be used to quantify the observability of the investigated model in chapter 4. While the first three subsections follow the introduction to GWs presented in [45], the latter two subsections summarize the discussion of SGWBs from FOPTs in [12, 26].

### 2.5.1 Gravitational radiation

The Einstein equations (2.1) are manifestly invariant under the coordinate transformations  $x^\mu \rightarrow x'^\mu(x)$ , where  $x'^\mu$  is an arbitrary smooth function<sup>10</sup> of  $x^\mu$ . Under these transformations, the metric transforms as

$$g_{\mu\nu}(x) \rightarrow g'_{\mu\nu}(x') = \frac{\partial x^\rho}{\partial x'^\mu} \frac{\partial x^\sigma}{\partial x'^\nu} g_{\rho\sigma}(x), \quad (2.64)$$

*Small perturbations  
of the flat metric*

which can be seen as the gauge symmetry of GR. Now, consider small<sup>11</sup> perturbations around the Minkowski metric  $g_{\mu\nu}(x) = \eta_{\mu\nu} + h_{\mu\nu}(x)$  and the coordinate transformation  $x^\mu \rightarrow x'^\mu = x^\mu + \xi^\mu(x)$ . One finds that under this change of coordinates, the metric perturbation transforms to lowest order as

$$h_{\mu\nu}(x) \rightarrow h'_{\mu\nu}(x') = h_{\mu\nu}(x) - (\partial_\mu \xi_\nu + \partial_\nu \xi_\mu). \quad (2.65)$$

If  $\mathcal{O}(|\partial_\mu \xi_\nu|) \leq \mathcal{O}(|h_{\mu\nu}|)$ , the condition  $|h_{\mu\nu}| \ll 1$  is preserved and the coordinate transformation is a symmetry of the whole theory. Thus, the Riemann tensor is not only covariant under general coordinate transformations  $g_{\mu\nu}(x) \rightarrow g'_{\mu\nu}(x')$  but (to leading order) invariant under  $h_{\mu\nu}(x) \rightarrow h'_{\mu\nu}(x')$ . We can therefore evaluate the Einstein equations in dependence of  $h_{\mu\nu}$  instead of  $h'_{\mu\nu}$ . Defining  $h \equiv \eta^{\mu\nu} h_{\mu\nu}$  and  $\bar{h}_{\mu\nu} \equiv h_{\mu\nu} - \frac{1}{2} \eta_{\mu\nu} h$  allows us to write the linearized field equations as

$$\square \bar{h}_{\mu\nu} + \eta_{\mu\nu} \partial_\alpha \partial_\beta \bar{h}^{\alpha\beta} - \partial_\alpha \partial_\nu \bar{h}_\mu^\alpha - \partial_\alpha \partial_\mu \bar{h}_\nu^\alpha = -2 \frac{T_{\mu\nu}}{m_{\text{Pl}}^2} \quad (2.66)$$

<sup>10</sup> More precisely,  $x'^\mu$  has to be invertible, differentiable and its inverse has to be differentiable, i. e.  $x'^\mu(x)$  is an arbitrary diffeomorphism.

<sup>11</sup> Here, "small" means that there exists a frame in which  $|h_{\mu\nu}(x)| \ll 1$  holds in a sufficiently large region of space-time.

with the flat-space d'Alembertian  $\square = \partial_\mu \partial^\mu$ . We can further simplify this result by deploying the Lorentz<sup>12</sup> gauge  $\partial^\nu \bar{h}_{\mu\nu} = 0$ , under which the field equations become the simple wave equation

*Imposing the Lorentz gauge yields a wave equation*

$$\square \bar{h}_{\mu\nu} = -2 \frac{T_{\mu\nu}}{m_{\text{Pl}}^2}, \quad (2.67)$$

since partial derivatives commute. This gauge can be imposed here, since  $\bar{h}_{\mu\nu}$  transforms under the proposed change of coordinates as

$$\bar{h}_{\mu\nu} \rightarrow \bar{h}'_{\mu\nu} = \bar{h}_{\mu\nu} - (\partial_\mu \xi_\nu + \partial_\nu \xi_\mu - \eta_{\mu\nu} \partial_\alpha \xi^\alpha), \quad (2.68)$$

such that for its space-time derivative

$$\partial^\nu \bar{h}_{\mu\nu} \rightarrow (\partial^\nu \bar{h}'_{\mu\nu})' = \partial^\nu \bar{h}_{\mu\nu} - \square \xi_\mu \stackrel{!}{=} 0 \quad (2.69)$$

holds. The condition  $\square \xi_\mu = \partial^\nu \bar{h}_{\mu\nu}$  for the last equation to hold can be achieved by fixing the coordinate transformation to

$$\xi_\mu(y) = \int d^4x G(x-y) \partial^\nu \bar{h}_{\mu\nu}(y), \quad (2.70)$$

where  $G(x-y)$  is the Green's function of the d'Alembertian, so a solution of  $\square_x G(x-y) = \delta^4(x-y)$ . Note that imposing the Lorentz gauge by choosing the components of  $\xi_\mu$  according to (2.70) reduces the degrees of freedom of the symmetric tensor field  $\bar{h}_{\mu\nu}$  to  $10 - 4 = 6$ .

To study the free propagation of the waves described by (2.67), set  $T_{\mu\nu} = 0$ . The resulting equation  $\square \bar{h}_{\mu\nu} = 0$  already tells us that GWs in vacuum travel with the speed of light. To further discuss the physical effects of such a wave, it is worth noting that the imposed condition  $\partial^\nu \bar{h}_{\mu\nu} = 0$  did not fix the gauge completely as (2.69) is not spoiled by another coordinate transformation  $x^\mu \rightarrow x^\mu + \xi^\mu$  with  $\square \xi_\mu = 0$ . Under this condition, also the quantity  $\xi_{\mu\nu} \equiv \partial_\mu \xi_\nu + \partial_\nu \xi_\mu - \eta_{\mu\nu} \partial_\alpha \xi^\alpha$  fulfills  $\square \xi_{\mu\nu} = 0$ , such that (2.68) tells us that we can subtract  $\xi_{\mu\nu}$ , sufficing the four conditions  $\square \xi_\mu = 0$ , from the six independent components of  $\bar{h}_{\mu\nu}$  without changing the wave equation (2.67). Hence, we can choose the function  $\xi_\mu$  so as to impose four additional conditions on the metric perturbation.

*GWs in vacuum*

In particular, one can choose  $\xi^0$  such that the trace  $\bar{h} = 0$  vanishes and  $\bar{h}_{\mu\nu} = h_{\mu\nu}$  holds. Moreover, one can choose the three functions  $\xi^i$  such that  $h^{i0} = 0$ . The 0-component of the Lorentz gauge condition  $\partial^\nu \bar{h}_{\mu\nu} = 0$  now directly shows that  $\partial_t h_{00} = 0$ , which means that

<sup>12</sup> In GR, the gauge  $\partial_\mu (g^{\mu\nu} \sqrt{g}) = 0$  defined for a curved background  $g$  reduces to the Lorentz gauge for small metric perturbations. Amusingly, the usual term ‘‘Lorentz gauge’’ (analog to  $\partial_\mu A^\mu = 0$  in electromagnetism) is a misnomer. The gauge was first used by the Danish physicist Ludvig Valentin Lorenz when the more famous Dutch physicist Hendrik Antoon Lorentz was still a child. In fact it is even worse: None of these two invented the gauge used here, but in fact it was Willem De Sitter who suggested the (later called) ‘‘harmonic gauge’’ to Einstein [46].

$h_{00}$  (describing a Newtonian potential) is time-independent and thus a constant. The GW itself is the time-dependent part of the metric perturbation. One can therefore follow that also  $h^{00} = 0$  must hold in our case.

So, in total we are left with  $h_{0\mu} = 0$  and the only non-zero contributions to  $h_{\mu\nu}$  come from its spacial parts  $h_{ij}$ . Hence, the Lorentz gauge condition simplifies to  $\partial^i h_{ij} = 0$  and the condition of the vanishing trace becomes  $\bar{h} = \eta_{\mu\nu} h^{\mu\nu} = h^i_i = 0$ . This set of conditions is known as the transverse-traceless (TT) gauge:

The TT gauge

$$h^{0\mu} = 0, \quad h^i_i = 0, \quad \partial^i h_{ij} = 0, \quad (2.71)$$

leaving only two independent degrees of freedom to  $h_{\mu\nu}$ . Note that this gauge cannot be chosen in the presence of sources  $T_{\mu\nu}$ <sup>13</sup>.

The monochromatic plane wave solution of (2.67) in the absence of sources and in TT gauge reads  $h_{ij}(x) = e_{ij}(\mathbf{k}) e^{ikx}$ , where  $e_{ij}(\mathbf{k})$  is a polarization tensor to account for the two independent DOFs of a GW. The usual convention that the real part is taken after the calculation is implied and the wave vector is defined as  $k^\mu \equiv (\omega, \mathbf{k})$  with  $\omega = |\mathbf{k}|$ . For a plane wave the transversality condition  $\partial^i h_{ij} = 0$  from equation (2.71) becomes  $n^i h_{ij} = 0$  with  $\hat{\mathbf{n}} \equiv \mathbf{k}/|\mathbf{k}|$ . Choosing the wave vector  $k^\mu = (\omega, 0, 0, \omega)$  yields

The plane wave solution

$$(h_{\mu\nu})(t, z) = \begin{pmatrix} 0 & 0 & 0 & 0 \\ 0 & h_+ & h_\times & 0 \\ 0 & h_\times & -h_+ & 0 \\ 0 & 0 & 0 & 0 \end{pmatrix} \cos[\omega(t - z)] \quad (2.72)$$

with the two degrees of freedom of a GW described by a +- and a  $\times$ -polarization, leading to the infinitesimal line element

$$\begin{aligned} ds^2 = & dt^2 - dx^2 \{1 + h_+ \cos[\omega(t - z)]\} \\ & - dy^2 \{1 - h_+ \cos[\omega(t - z)]\} \\ & - 2 dx dy h_\times \cos[\omega(t - z)] - dz^2. \end{aligned} \quad (2.73)$$

The chosen wave vector now illustrates neatly the effect of an incoming monochromatic GW from the  $z$ -direction on two test masses (or events) at  $(t, x_1, 0, 0)$  and  $(t, x_2, 0, 0)$ : Their *coordinate distance*  $L = x_2 - x_1$  remains constant, while their *proper distance* changes periodically

$$s = L \sqrt{1 + h_+ \cos(\omega t)} \simeq L \left[ 1 + \frac{1}{2} h_+ \cos(\omega t) \right]. \quad (2.74)$$

<sup>13</sup> The procedure presented here is completely analog to the gauge fixing in electromagnetism: The classical equations of motion in the presence of sources read  $\partial_\mu (\partial^\mu A^\nu - \partial^\nu A^\mu) = j^\nu$ , simplifying to  $\square A^\mu = j^\mu$  after imposing the Lorentz gauge  $\partial_\mu A^\mu = 0$ , leaving untouched the residual gauge freedom  $A_\mu \rightarrow A_\mu - \partial_\mu \theta$  with  $\square \theta = 0$ . Outside the source,  $\square A^\mu = 0$  holds and the residual gauge freedom  $\square \theta = 0$  can be used to fix  $A^0 = 0$ , rendering the Lorentz condition effectively a transversality condition  $\partial_i A^i = 0$ . In the presence of a source  $j^0 \neq 0$  we see that  $\square A^0 \neq 0$  such that  $A^0$  cannot be set to zero using a function  $\theta$  that satisfies  $\square \theta = 0$ .

If the two test masses are mirrors reflecting a light beam back and forth, the calculated proper distance between these two masses describes an oscillation of the time difference between the reflections. This is the working principle of the interferometers used for GW detection<sup>14</sup>.

*The working principle of GW interferometry*

More generally, the proper distance of two test masses, whose spacial coordinates differ by a vector  $\mathbf{L}$  with modulus  $L$ , is given by  $s^2 = L^2 + h_{ij}(t) L_i L_j$ . Up to leading order in the metric perturbation the proper distance is given by  $s \simeq L + h_{ij}(t) L_i L_j / (2L)$ , implying

$$\ddot{s} \simeq \frac{1}{2} \ddot{h}_{ij} \frac{L_i}{L} L_j \quad \Rightarrow \quad \ddot{s}_i \simeq \frac{1}{2} \ddot{h}_{ij} L_j \simeq \frac{1}{2} \ddot{h}_{ij} s_j, \quad (2.75)$$

where  $s_i = s L / L_i$  has been introduced. Therefore, the physical effect of the two polarization modes can be made clear by considering the change in the proper distance of the spacial coordinate origin at  $(t, 0, 0, 0)$  and a test mass at  $(t, x_0, y_0, 0)$  when a GW with a certain polarization propagates through them. While a  $+$ -polarized GW leads to the shifts

$$\delta s_x \simeq \frac{h_+}{2} x_0 \cos(\omega t), \quad \delta s_y \simeq -\frac{h_+}{2} y_0 \cos(\omega t) \quad (2.76)$$

of the proper distance between the two bodies along the  $x$ - and  $y$ -axes, a  $\times$ -polarized GW results in the shifts

$$\delta s_x \simeq \frac{h_\times}{2} y_0 \cos(\omega t), \quad \delta s_y \simeq \frac{h_\times}{2} x_0 \cos(\omega t) \quad (2.77)$$

in the proper distance. A sketch of these effects on a ring of test masses can be found in Figure 2.11.

### 2.5.2 Energy and momentum of gravitational waves

It is already clear from the discussion of the effect of a GW on test masses, that also gravitational radiation must carry energy and momentum. In particular, this can be seen from the fact that the interaction with matter can be described as a Newtonian force giving kinetic energy to the test masses. To find the corresponding energy-momentum tensor, one can perform two independent calculations giving the same result. The details of these calculations are of no further interest here. Nonetheless, to get a feel for where the resulting energy-momentum tensor comes from, we describe briefly the general method of both calculations. A detailed description of the actual

<sup>14</sup> Interestingly, the same calculation can be made without the need to impose a TT gauge frame, in which the coordinates of the test masses are by definition constant, but in the proper frame of the detector with the same physical result: For two nearby test-masses moving along their geodesics  $x(\tau)$  and  $x(\tau) + \zeta(\tau)$  with a common proper time  $\tau$ , the effect of a passing GW can be described as a Newtonian force  $F_i = \frac{m}{2} \ddot{h}_{ij} \zeta^j$  [45].

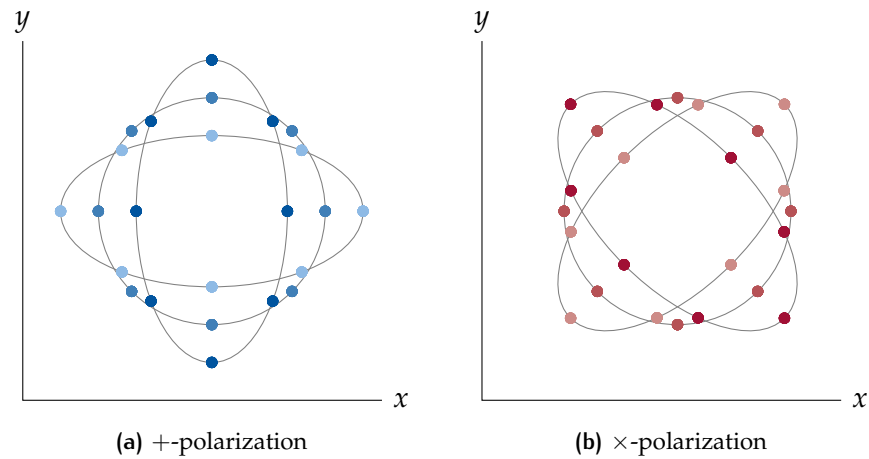


**Figure 2.11:** The influence of a GW propagating in  $z$ -direction on a ring of test masses lying in the  $x$ - $y$ -plane. The saturation of the colors indicates the time dependence of the test masses' positions.

computations can be found in the chapters 1.4 and 2.1 of reference [45].

First, one can calculate the space-time curvature due to the GWs themselves bending the background metric. One can then reuse the Einstein equations in a “backward” fashion to find the energy-momentum tensor corresponding to the evoked curvature. To do this, it is necessary to reformulate the already done calculations in terms of a generally dynamic background metric such that  $g_{\mu\nu}(x) = \bar{g}_{\mu\nu}(x) + h_{\mu\nu}(x)$ . This description is similar to the division of water waves in the sea into background waves coming from the incoherent superposition of waves of diverse origins and a single wave propagating in this background. Obviously, there exists some ambiguity of choice to define which part of the vertical motion of the sea's surface belongs to which origin. However, there are cases in which a natural splitting of the origins is possible. Of particular interest in our case is the splitting of frequency scales which leads to a kind of renormalization group procedure separating the high-frequency part of the metric (belonging to  $h_{\mu\nu}$ , i. e. the gravitational wave) and the low-frequency part (representing quasi-static Newtonian potentials). Using this method, one can effectively integrate out the short-wavelength degrees of freedom by performing a spatial average of the Einstein equations in volumes defined by some intermediate length scale to obtain the energy-momentum tensor of a GW.

The second method treats linearized gravity as a classical field theory and applies Noether's theorem to get the energy-momentum tensor as a conserved current related to the invariance under space-time translations. In this approach we forget about the interpretation of  $h_{\mu\nu}$  as a metric perturbation and deal with it as with any other classical

*How GWs curve the background metric*

*Treating linearized gravity as a classical field theory*

field living in flat space-time with the Minkowski metric  $\eta_{\mu\nu}$ . A general infinitesimal transformation  $x^\mu \rightarrow x^\mu + \epsilon^a A_a^\mu(x)$  under which the classical fields  $\phi_i$  transform as  $\phi_i(x) \rightarrow \phi_i(x) + \epsilon^a F_{i,a}(\phi, \partial\phi)$  is defined to be a symmetry transformation if it leaves the theory's action  $S[\phi]$  invariant. Therein  $A_a^\mu(x)$  is known as the generator of the symmetry as it specifies the symmetry transformation, and  $F_{i,a}$  is a function of the fields  $\phi_i$  and their derivatives. The symmetry is *global* for the parameters  $\epsilon^a$  being constants and *local* in the case when they are arbitrary functions of  $x$ . Noether's theorem then states that for every generator  $\epsilon^a$  of a global symmetry, there is a conserved current. In the most general case, this current is given by

$$j_a^\mu = \frac{\partial \mathcal{L}}{\partial (\partial_\mu \phi_i)} [A_a^\nu(x) \partial_\nu \phi_i - F_{i,a}(\phi, \partial\phi)] - A_a^\mu(x) \mathcal{L}, \quad (2.78)$$

where  $\mathcal{L}$  is the Lagrangian density of the classical field theory. If the action is globally invariant under space-time translations, this yields the energy-momentum tensor as a conserved Noether current. This is precisely the case in linearized gravity, since  $h_{\mu\nu}$  is invariant under transformations<sup>15</sup>  $x^\mu \rightarrow x^\mu + a^\mu$ , where  $a^\mu$  is not restricted to be infinitesimal, but can be finite as one can see from (2.64). However, since  $\mathcal{L}$  is only defined up to total divergences, Noether currents are not uniquely defined<sup>16</sup>. Hence, a conserved Noether current is not necessarily a physical observable but rather a quantity that, when integrated over space, gives unambiguously the physical conserved charge as long as the field configuration goes to zero sufficiently fast at the boundaries of the integrated region. Equivalently, instead of speaking about localized quantities, one can perform averages over large enough regions of space such that the ambiguity related to the total divergences disappears.

In the end of either of these calculations, one finds the following result:

*Energy-momentum  
tensor of a GW*

$$t_{\mu\nu} = \frac{m_{\text{Pl}}^2}{4} \langle \partial_\mu h_{\alpha\beta} \partial_\nu h^{\alpha\beta} \rangle, \quad (2.79)$$

which can be shown to be independent of the choice of gauge. The brackets  $\langle \cdot \rangle$  are understood to be a spacial average over many wavelengths in the case of  $\frac{\lambda}{2\pi} \ll L_B$  or analogously a time average over many periods  $1/f$  in the case of  $f \gg f_B$ , where  $\lambda$  and  $f$  are a characteristic wavelength and frequency of the GW while  $L_B$  and  $f_B$  are characteristic length and frequency scales of the background met-

<sup>15</sup> In fact, linearized gravity is symmetric also under finite Lorentz translations and rotations. The theory thus obeys a Poincaré symmetry in contrast to full GR. Therefore, not only energy and momenta are conserved, but also angular momenta and the center of mass of a GW.

<sup>16</sup> This is the reason why in electromagnetism there exist several conserved energy-momentum tensors out of which some are not even gauge-invariant.

ric. In particular, after choosing the TT gauge, this yields the (again, gauge-invariant) energy density

$$\rho_{\text{GW}} = t^{00} = \frac{m_{\text{Pl}}^2}{4} \langle \partial_t h_{ij} \partial_t h^{ij} \rangle. \quad (2.80)$$

### 2.5.3 Stochastic backgrounds

*Superposition of plane waves*

Using a plane wave expansion for the solution of the gravitational wave equation 2.67 in vacuum and employing the TT gauge, one can generally write [7, 45]

$$h_{ij}(t, \mathbf{x}) = \sum_{A=+, \times} \int_{-\infty}^{+\infty} df \int d^2 \hat{\mathbf{n}} \tilde{h}_A(f, \hat{\mathbf{n}}) e_{ij}^A(\hat{\mathbf{n}}) e^{-2\pi i f(t - \hat{\mathbf{n}} \cdot \mathbf{x})} \quad (2.81)$$

with  $e_{ij}^+(\hat{\mathbf{n}}) = \hat{\mathbf{u}}_i \hat{\mathbf{u}}_j - \hat{\mathbf{v}}_i \hat{\mathbf{v}}_j$  and  $e_{ij}^\times(\hat{\mathbf{n}}) = \hat{\mathbf{u}}_i \hat{\mathbf{v}}_j - \hat{\mathbf{v}}_i \hat{\mathbf{u}}_j$ , where  $\hat{\mathbf{u}}$  and  $\hat{\mathbf{v}}$  are unit vectors orthogonal to the propagation direction  $\hat{\mathbf{n}}$  of the GW and each other. A stochastic background is now defined as the case where the GW amplitudes  $\tilde{h}_A(f, \hat{\mathbf{n}})$  are random variables, characterized statistically by their ensemble averages. Since we obviously have only one realization of our Universe, this ensemble average is replaced by a temporal average by use of the ergodic hypothesis.

*Assumptions on SGWBs*

To simplify this general result, the following assumptions on stochastic backgrounds are usually made [45]:

**STATIONARITY:** The two-point correlator  $\langle h_A(t) h_{A'}(t') \rangle$  can only depend on the time difference  $t - t'$  and not separately on  $t$  and  $t'$ . This assumption is well justified<sup>17</sup> considering the different time scales of the detection (typically a few years) and the age of the signal (typically of the order of the age of the Universe). Stationarity also implies that  $\langle h_A(t) \rangle$  must be a constant (theoretically contributing to vacuum energy). However, since we are interested only in GWs, so the time-dependent part of metric fluctuations, we can set  $\langle h_A \rangle = 0$  in our analysis.

**GAUSSIANTY:** The central limit theorem states that a large ensemble of independent events produces a Gaussian stochastic process, regardless of the probability distribution of the individual events. This is expected to hold for cosmological backgrounds. As in the case of the CMB anisotropies, gaussianity states that all  $N$ -point correlators are functions of  $\langle h_A \rangle$  (which we have set to zero) and the two-point correlator  $\langle h_A(t) h_{A'}(t') \rangle$ . The assumption of gaussianity would not hold for the case of an astrophysical

<sup>17</sup> A detailed discussion of this assumption and what changes when dropping it can be found in reference [47].

stochastic background with only a few almost indistinguishable contributions. In that case, further information could be gained using higher-point correlators.

**ISOTROPY:** As in the case of the CMB (where the anisotropies are of order  $\mathcal{O}(\Delta T/T) \sim 10^{-5}$ ), we expect that a stochastic background of cosmological origin is isotropic in first approximation. Thus, waves coming from different directions should be uncorrelated such that in Fourier space  $\langle \tilde{h}_A^*(f, \hat{\mathbf{n}}) \tilde{h}_{A'}(f', \hat{\mathbf{n}}') \rangle$  is proportional to  $\delta^2(\hat{\mathbf{n}}, \hat{\mathbf{n}}') = \delta(\phi - \phi') \delta(\cos \theta - \cos \theta')$ , where  $\phi$  and  $\theta$  are the polar angles defining  $\hat{\mathbf{n}}$ . Further, the constant of proportionality should not depend on  $\hat{\mathbf{n}}$ . A potential dipole-term will tell us about our motion with respect to the CMB frame while higher-order poles can decode valuable information on the very early Universe. For the case of astrophysical backgrounds (especially when coming from our galactic plane) the assumption of isotropy has to be dropped.

**NO POLARIZATION:** It is natural to assume that a background of cosmological origin (or from many different astrophysical sources) is unpolarized. This means, that  $\langle \tilde{h}_A^*(f, \hat{\mathbf{n}}) \tilde{h}_{A'}(f', \hat{\mathbf{n}}') \rangle$  is proportional to  $\delta_{AA'}$  and that the respective prefactor is independent of the polarization index  $A$ .

Adopting these assumptions, a stochastic background is completely characterized by the so-called spectral density  $S_h(f)$  defined by

*Describing an SGWB with the spectral density  $S_h(f)$*

$$\begin{aligned} \langle \tilde{h}_A^*(f, \hat{\mathbf{n}}) \tilde{h}_{A'}(f', \hat{\mathbf{n}}') \rangle &= \frac{1}{4\pi} \delta_{AA'} \delta(f - f') \delta(\phi - \phi') \\ &\times \delta(\cos \theta - \cos \theta') \frac{1}{2} S_h(f), \end{aligned} \quad (2.82)$$

where the factor  $(4\pi)^{-1}$  was chosen as a choice of normalization for the integration over  $\hat{\mathbf{n}}$  and the factor  $\frac{1}{2}$  was chosen to be consistent with the definition of one-sided noise spectral densities. The spectral density  $S_h(f)$  has the unit  $\text{Hz}^{-1}$  and satisfies  $S_h(f) = S_h(-f)$ . Using the normalization of the polarization tensors  $\sum_A e_{ij}^A e_{ij}^A = 4$ , one thus obtains for  $h_{ij}(t) \equiv h_{ij}(t, \mathbf{x} = 0)$

$$\langle h_{ij}(t) h^{ij}(t) \rangle = 4 \int_0^\infty df S_h(f). \quad (2.83)$$

A better physical understanding of the spectral density for stochastic backgrounds  $S_h(f)$  can be achieved by finding its dependence on the energy density  $\rho_{\text{GW}}$  carried by a GW as defined in (2.80). The energy density  $\rho_{\text{GW}}$  can be normalized to the critical energy density  $\rho_c \equiv 3 m_{\text{Pl}}^2 H^2$  needed for closing the universe,

$$\Omega_{\text{GW}} \equiv \frac{\rho_{\text{GW}}}{\rho_c} = \int_{f=0}^{f=\infty} d(\log f) \frac{1}{\rho_c} \frac{d\rho_{\text{GW}}}{d \log f}$$

$$= \int_{f=0}^{f=\infty} d(\log f) \Omega_{\text{GW}}(f). \quad (2.84)$$

The spectral density  $d\rho_{\text{GW}}/d\log f$  for the energy density  $\rho_{\text{GW}}$  and the spectral density  $\Omega_{\text{GW}}(f)$  of the normalized energy density  $\Omega_{\text{GW}}$  have been introduced in their conventional notation. Note that  $d\rho_{\text{GW}}/d\log f$  is not an actual derivative but rather a symbol to denote the spectral density defined as energy per unit logarithmic interval of frequency. This has the advantage that the resulting quantity  $\Omega_{\text{GW}}(f)$  is dimensionless. This ambiguity of notation is tolerated here, since it is the conventional nomenclature in the literature. As discussed in the last section 2.5.2, the brackets  $\langle \cdot \rangle$  in the definition of  $\rho_{\text{GW}}$  in equation (2.80) denote a time average. However, under the ergodic assumption, this is equivalent to the ensemble average discussed above. After plugging in the plane wave expansion (2.81) into (2.80) and performing the ensemble average using (2.82), one finds

$$\rho_{\text{GW}} = m_{\text{Pl}}^2 \int_{f=0}^{f=\infty} d(\log f) f (2\pi f)^2 S_h(f), \quad (2.85)$$

The spectral energy density  $\Omega_{\text{GW}}(f)$

from which follows the wanted expression [45]

$$\Omega_{\text{GW}}(f) = \frac{4\pi^2}{3H^2} f^3 S_h(f). \quad (2.86)$$

#### 2.5.4 The spectrum of gravitational waves from first-order phase transitions

To connect the calculation of the spectral density  $\Omega_{\text{GW}}(f)$  with FOPTs it is still necessary to discuss how a metric perturbation  $h_{\mu\nu}$  can be generated. Using the method of Green's functions for the wave equation (2.67) and performing a multi-pole expansion of the source energy-momentum tensor  $T_{\mu\nu}$ , one can find that the metric perturbation in the TT gauge can be calculated to leading order as

Sources of GWs

$$h_{ij}(t, \mathbf{x}) = \frac{1}{4\pi r} \frac{\ddot{Q}_{ij}^{\text{TT}}(t-r)}{m_{\text{Pl}}^2}, \quad (2.87)$$

where  $r = |\mathbf{x}|$  is the distance to the source and  $Q_{ij}^{\text{TT}} = Q_{ij} - \frac{1}{3}\delta_{ij}Q_k^k$  is the TT representation of the quadrupole tensor [26, 45]

$$Q_{ij}(t) = \int d^3x' T_{00}(t, \mathbf{x}') x'_i x'_j. \quad (2.88)$$

Therefore, only the time-dependent and anisotropic, hence non-spherical motions of energy densities source GWs. This is the reason why the expansion of a bubble in an FOPT does not emit gravitational radiation, but why the collision of bubbles eventually will.

The careful analysis of the quadrupole tensor in computer simulations of FOPTs combined with analytical and numerical work showed that the SGWB spectrum from phase transitions can be calculated by summing over the contributions from bubble collisions, density (“sound”) waves in the plasma that later on also collide, and magnetohydrodynamic (MHD) turbulence. The resulting expression for the spectrum at its emission reads

$$\Omega_{\text{GW}}(f) \simeq \sum_{\text{sources}} \mathcal{N} \Delta \left( \frac{\kappa \alpha}{1 + \alpha} \right)^p \left( \frac{H}{\beta} \right)^q s(f), \quad (2.89)$$

where the parameters  $\mathcal{N}$ ,  $\kappa$ ,  $p$ ,  $q$ ,  $\Delta$ ,  $f_p$  and the power law spectral shape  $s(f)$  depend on the kind of GW source [12]. An overview of these quantities can be found in table 2.1. Note that the given values and formulas are rather to be understood as approximations and do not represent the most recent and precise methods to calculate GW spectra. An analysis of the theoretical uncertainties coming with this comparably low level of diligence can be found in reference [48], for instance.

	Collisions	Sound waves	MHD turbulence
$\mathcal{N}$	1	$1.59 \times 10^{-1}$	$2.01 \times 10^1$
$\kappa$	$\kappa_\phi$	$\kappa_{\text{sw}}$	$\epsilon_{\text{turb}} \kappa_{\text{sw}}$
$p$	2	2	$\frac{3}{2}$
$q$	2	1	1
$\Delta$	$\frac{0.11 v_w^3}{0.42 + v_w^2}$	$v_w$	$v_w$
$f_p$	$\frac{0.62 \beta}{1.8 - 0.1 v_w + v_w^2}$	$\frac{2 \beta}{\sqrt{3} v_w}$	$\frac{3.5 \beta}{2 v_w}$
$s(f)$	$\frac{3.8 (f/f_p)^{2.8}}{1 + 2.8 (f/f_p)^{3.8}}$	$\left( \frac{f}{f_p} \right)^3 \left( \frac{7}{4 + 3 (f/f_p)^2} \right)^{7/2}$	$\frac{(f/f_p)^3}{(1 + f/f_p)^{11/3} [1 + 8 \pi (f/H)]}$

**Table 2.1:** The SGWB of an FOPT has contributions from the collision of bubble walls, sound waves, and MHD turbulence. The quantity  $\mathcal{N}$  normalizes the spectrum,  $\kappa$  is an efficiency factor that describes how much of the phase transition’s latent heat is available for the respective process,  $p$  and  $q$  quantify the impact of the FOPT strength  $\alpha$  and the inverse timescale  $\beta/H$  on the GW spectrum,  $\Delta$  indicates the effect of the bubble wall velocities  $v_w$ , and  $f_p$  quantifies the peak of the power-law frequency spectrum of the different contributions. Ultimately,  $s(f)$  describes the general shape of the power-law spectra corresponding to the different sources. A detailed description of the origin of these quantities can be found in reference [49].

The quantity  $\alpha$  is a measure of the strength of the FOPT and is proportional to the amount of energy density released in the phase transition. As seen in section 2.3, the effective potential resembles a free energy density  $f = V_{\text{eff}}(\phi, T)$  that tends to be minimal by the principle of stationary action. Since (neglecting chemical potentials), the thermal

bath of particles can be described by a canonical ensemble, the thermodynamical relations  $s = -\partial_T f$  and  $\rho = f + T s$  hold. Hence, the latent heat of the phase transition is given by

$$\epsilon = -\Delta f - T_n \Delta s = \left( -\Delta V_{\text{eff}} + T_n \frac{\partial \Delta V_{\text{eff}}}{\partial T} \right) \Big|_{T=T_n} > 0, \quad (2.90)$$

where  $\Delta$  denotes the difference between the respective quantities before and after the transition from the false to the true vacuum state [12, 26]. The function  $\Delta V_{\text{eff}}(T) < 0$  denotes the difference in potential energy density between the two vacua. To receive a dimensionless quantity, the latent heat is normalized to the total energy density of the surrounding plasma of relativistic species  $\rho \simeq \rho_{\text{rad}}$  (assuming a radiation-dominated Universe), such that

$$\alpha \equiv \frac{\epsilon}{\rho_{\text{rad}}}. \quad (2.91)$$

The derivative of the logarithmized bubble nucleation rate  $\Gamma(T) \propto \exp[-S_3(T)/T]$  with respect to time at the nucleation temperature  $T_n$  corresponds to an inverse time-scale of an FOPT (see Figure 2.10). In the following, the inverse time-scale  $\beta/H$  is used, which is normalized to the inverse Hubble time  $H(T_n)$  at nucleation, giving a meaningful reference scale for cosmology. This normalization occurs naturally when switching from time to temperature derivatives:

$$\frac{\beta}{H} \equiv T_n \frac{d}{dT} \left( \frac{S_3(T)}{T} \right) \Big|_{T=T_n}. \quad (2.92)$$

A fast transition happens on a short time-scale and thus leads to a large  $\beta/H$ , which damps the resulting spectrum  $\Omega_{\text{GW}} \propto (H/\beta)^q$  with  $q = 1$  or  $q = 2$ , depending on the production mechanism of the GWs. This damping is due to the almost simultaneous production of bubbles in a fast transition, which will eventually collide while still being relatively small. In the opposite case of a slow transition, the bubble nucleation rate is low and eventually larger, more energetic bubbles collide. Since the small bubbles after a fast transition collide more frequently than in the opposite case, the corresponding spectrum will also peak at a higher frequency [12].

The efficiency factors  $\kappa$  of the three contributions are functions of the transition strength  $\alpha$  and depend further on the coupling between the plasma and the bubble wall. If  $\alpha$  exceeds a threshold strength  $\alpha_\infty$ , the bubble walls can accelerate continuously (i. e. the “runaway regime”), while in the opposed case there will be a terminal velocity (i. e. the “non-runaway regime”). In the non-runaway regime,  $\kappa_\phi = 0$  since the contribution from bubble collisions is negligible, as the latent energy of the phase transition can be efficiently converted into plasma motion. In that case  $\kappa_{\text{sw}}$  is given by

$$\kappa(\alpha) \simeq \frac{\alpha}{0.73 + 0.083 \sqrt{\alpha} + \alpha} \quad (2.93)$$

*The transition strength  $\alpha$*

*The inverse time-scale  $\beta/H$*

*Runaway bubbles*

for  $v_w \sim 1$  [49]. Conversely, in the runaway regime only a fraction  $\alpha_\infty/\alpha$  of  $\epsilon$  is converted into plasma motion and the remaining energy density accelerates the bubble walls. Hence,  $\kappa_\phi = 1 - \alpha_\infty/\alpha$  and  $\kappa_{\text{SW}} = \kappa(\alpha_\infty) \alpha_\infty/\alpha$  hold. In either case, a fraction of the bulk motion energy of  $\epsilon_{\text{turb}} \simeq 10\%$  is converted into turbulence. We employ this optimistic approximation as it is done in [12].

The bubble wall velocity  $v_w$  is the most intricate parameter, since its calculation requires knowledge of the diverse, highly model-dependent particle processes that happen at the bubble wall. In general, the collision of particles in the plasma with a bubble exerts a non-negligible pressure on its moving wall. Additionally, next to the mere change of momentum of particles being reflected, there is also an additional friction term due to transition radiation by gauge bosons, which is likely to dominate over the friction from particles colliding with the wall [50]. A detailed analysis of the processes happening at the bubble wall requires the solution of Boltzmann-like equations and is still a subject of current research. However, for sufficiently strong FOPTs, the bubble walls will quickly reach luminal velocities. Since strong phase transitions are favorable for detectable SGWB signals, we will focus on sufficiently strong transitions for which  $v_w \sim 1$ , and remain agnostic about the details of the bubble wall dynamics.

*The bubble wall velocity  $v_w$*

One central result from the balance of friction terms and forward driving pressure, however, is the critical transition strength  $\alpha_\infty$  for non-runaway bubbles. One eventually finds that the friction exerted by particles getting (more) massive in an FOPT is approximately given by

*The critical transition strength  $\alpha_\infty$*

$$P_{\text{fric}} \approx \Delta V_{\text{T}} \approx T^2 \left[ \sum_b \frac{n_b}{24} \Delta m_b^2(\phi) + \sum_f \frac{n_f}{48} \Delta m_f^2(\phi) \right]. \quad (2.94)$$

The condition  $\epsilon > P_{\text{fric}}$  for runaway bubbles is thus equivalent to  $\alpha > \alpha_\infty \equiv \Delta V_{\text{T}}/\rho_{\text{rad}}$ , which will be used as a definition for the threshold transition strength. Note that the expression in (2.94) is meant to sum over all changing physical particle masses, including longitudinal gauge boson modes, but excluding Goldstone boson modes [51].

After its emission, the SGWB propagates freely and undisturbed until today, effectively being a form of dark radiation<sup>18</sup>. The expansion of the Universe, however, redshifts both its amplitude and its frequency such that today's power spectrum,  $\Omega_{\text{GW}}^0(f)$ , can be expressed as

*The spectrum's redshift*

$$\Omega_{\text{GW}}^0(f) = \mathcal{R} \Omega_{\text{GW}} \left( \frac{a_0}{a_n} f \right), \quad (2.95)$$

where  $f$  denotes the spectrum's frequency in today's units, which is shifted to its value at nucleation by multiplication with the scale factor

<sup>18</sup> This is not precisely true, see e. g. [52]. Since the effects that change the propagation of the GW are subdominant, we will however stick to that nomenclature.

ratio  $a_0/a_n$ , where  $a_n$  ( $a_0$ ) is the scale factor at nucleation (today) [12]. The amplitude of the spectrum redshifts like  $a^{-4} H^{-2}$ , since the energy density of radiation scales with  $a^{-4}$ , while the critical energy density  $\rho_c$  with which  $\rho_{\text{GW}}$  is normalized scales with  $H^2$ . The prefactor  $\mathcal{R}$  is thus defined as

$$\mathcal{R} \equiv \left(\frac{a_n}{a_0}\right)^4 \left(\frac{H_n}{H_0}\right)^2. \quad (2.96)$$

In the following chapter 3, we will see how the dilution effect by the out-of-equilibrium decay of a dark sector into SM particles can contribute to the the ratio  $a_0/a_n$  and the quantity  $\mathcal{R}$ . We will then discuss the impact of the phase transition parameters  $\alpha$ ,  $\beta/H$  and  $T_n$  on the spectrum and show exemplary plots of the calculated signal strengths including the additional dilution effect. In the following, we will omit the index “0” in  $\Omega_{\text{GW}}^0(f)$ , as we will always refer to red-shifted spectra.

### 2.5.5 Detection of stochastic backgrounds

To quantify the detectability of an SGWB, several measures have been invented. We will follow a frequentist approach by calculating SNRs. The optimal-filter cross-correlated SNR is given by

*Signal-to-noise ratios*

$$\rho^2 = 2 t_{\text{obs}} \int_{f_{\text{min}}}^{f_{\text{max}}} df \left[ \frac{h^2 \Omega_{\text{GW}}(f)}{h^2 \Omega_{\text{eff}}(f)} \right]^2, \quad (2.97)$$

where  $t_{\text{obs}}$  is the duration of the observation,  $(f_{\text{min}}, f_{\text{max}})$  is the detector’s frequency band, and  $h^2 \Omega_{\text{eff}}(f)$  is the effective noise spectrum expressed in the same units as the spectral gravitational wave energy density [12]. The constant  $h \equiv H_0/(100 \text{ km s}^{-1} \text{ Mpc}^{-1}) \simeq 0.68$  denotes the dimensionless Hubble constant, which is introduced to make the signal spectra independent of the physical value of the Hubble constant  $H_0$  [16]. The effective noise spectrum  $h^2 \Omega_{\text{eff}}(f)$  quantifies not only detector noises but includes also contributions from other unresolved backgrounds, e. g. expected astrophysical SGWBs. If the experiment consists of only a single detector, the factor 2 in (2.97) has to be dropped to account for an auto-correlation rather than a cross-correlation. We will refer to an SGWB as being observable if  $\rho$  is greater than a certain threshold value  $\rho_{\text{thr}}$ . A list of threshold SNRs for experiments with a range of detectable frequencies relevant for the following analysis can be found in table 2.2.

*Power-law integrated sensitivity curves*

For power-law spectra it has become standard to also quote so-called power-law integrated (PLI) curves  $h^2 \Omega_{\text{PLI}}(f)$ , which allow for an immediate decision whether a signal  $h^2 \Omega_{\text{GW}}(f)$  is observable or not by

Experiment	Frequency range	$\rho_{\text{thr}}$	$t_{\text{obs}}$	Auto-correlated?
LISA	$10^{-5} - 1$ Hz	10	4 yrs	✓
B-DECIGO	$10^{-2} - 10^2$ Hz	8	4 yrs	✓
DECIGO	$10^{-3} - 10^2$ Hz	10	4 yrs	✗
BBO	$10^{-3} - 10^2$ Hz	10	4 yrs	✗
ET	$1 - 10^4$ Hz	5	5 yrs	✓

**Table 2.2:** Assumed threshold SNRs  $\rho_{\text{thr}}$  of future space-based and ground-based interferometers for SGWBs as well as their expected duration of observation  $t_{\text{obs}}$  and frequency range. While DECIGO and BBO will consist of networks of GW detectors, LISA, B-DECIGO and ET will be single-detector observatories. In these cases, the cross-correlation SNR in (2.97) has to be replaced by an auto-correlation measure. The corresponding expression is found to be the same, but with the prefactor  $2t_{\text{obs}}$  replaced by  $t_{\text{obs}}$ . The values and assumptions in this table are taken from [12].

just looking for intersections of the two curves. Assuming that the latter follows a power-law with spectral index  $b$ , i. e.

$$h^2 \Omega_{\text{GW}}(f) = h^2 \Omega_b \left( \frac{f}{\bar{f}} \right)^b, \quad (2.98)$$

where  $h^2 \Omega_b$  is the GW spectral energy density at an arbitrarily chosen pivot frequency  $\bar{f}$ , the SGWB will be observable if

$$h^2 \Omega_b > h^2 \Omega_b^{\text{thr}} \equiv \frac{\rho_{\text{thr}}}{\sqrt{2t_{\text{obs}}}} \left[ \int_{f_{\text{min}}}^{f_{\text{max}}} df \left( \frac{(f/\bar{f})^b}{h^2 \Omega_{\text{eff}}(f)} \right)^2 \right]^{-\frac{1}{2}}. \quad (2.99)$$

The PLI sensitivity function  $h^2 \Omega_{\text{PLI}}(f)$  can then be obtained by evaluating the right-hand side of (2.99) in dependence of the spectral index  $b$  to determine the envelope of the corresponding power-law spectra as the sensitivity limit of the experiment. Thus, the PLI sensitivity curve can be expressed as

$$h^2 \Omega_{\text{PLI}}(f) = \max_b \left[ h^2 \Omega_b^{\text{thr}} \left( \frac{f}{\bar{f}} \right)^b \right]. \quad (2.100)$$

Strictly speaking, the interpretation that  $h^2 \Omega_{\text{PLI}}(f)$  describes the experimentally accessible region of a detector is only true for spectra that follow a power-law in the whole frequency range of the detector [12]. However, as we have seen, SGWBs from FOPTs follow at least approximately broken power-laws. Therefore, this method is useful but not precise. This is why we will still use the direct calculation (2.97) to calculate SNRs and investigate the detectability of signals, but why plots with PLI instead of spectral noise curves will be presented. In Figure 2.12, the effective noise spectra  $h^2 \Omega_{\text{eff}}(f)$  and the PLI curves  $h^2 \Omega_{\text{PLI}}(f)$  for the GW observatories from Table 2.2 are shown.

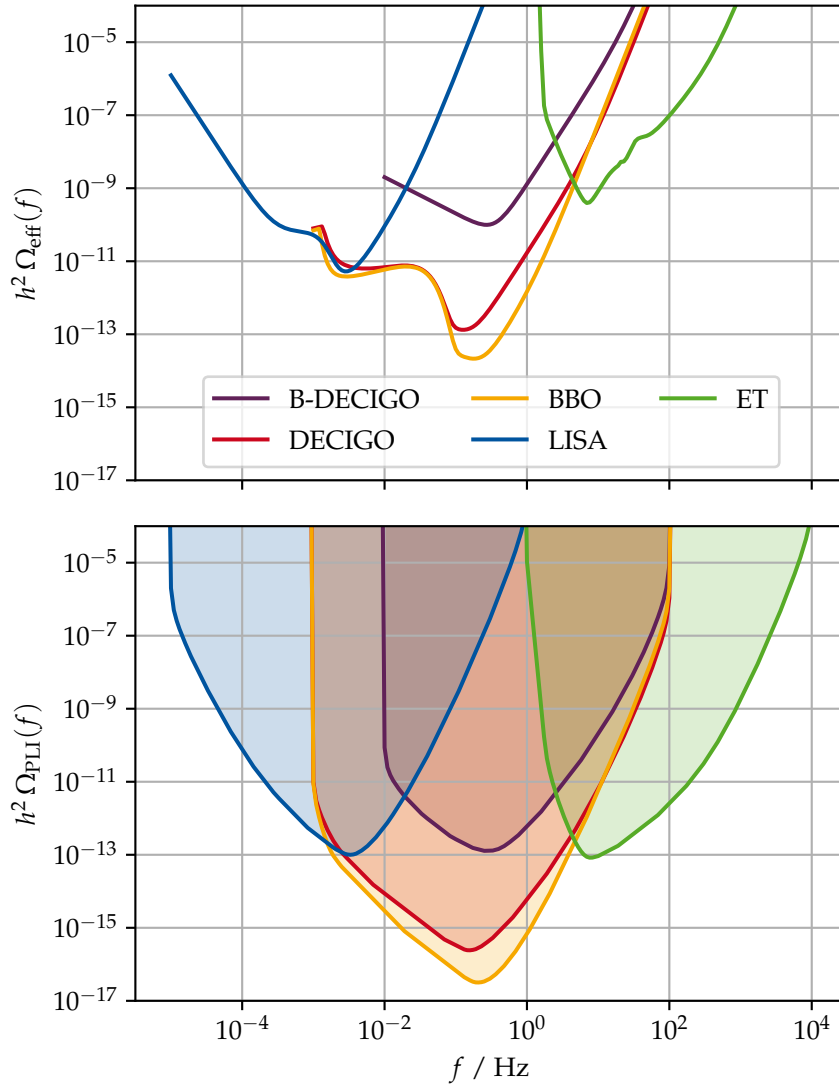


**Figure 2.12:** Plots of the expected effective noise energy spectrum  $h^2 \Omega_{\text{eff}}$  and the corresponding PLI sensitivities for future space- and ground-based GW observatories. The dips in  $h^2 \Omega_{\text{eff}}$  for LISA, B-DECIGO and DECIGO stem from the expected unresolved background from galactic and extra-galactic compact binaries, i. e. white dwarfs orbiting each other and emitting gravitational radiation, resulting in an astrophysical SGWB. The data underlying these curves has been taken from the ancillary material of [12]. Note that these curves represent only speculative estimates of experimental sensitivities, since the corresponding observatories still have to be built before they can start taking data.

# 3

## THE DECAY OF A HOT DARK SECTOR

The general description of particle cosmology, phase transitions, and SGWBs is now finished and we can go over to the investigation of DSs. This chapter is aimed at being as general as possible in the description of the evolution of a DS, even though some assumptions on a specific dark sector model will be made. To be more precise, we will focus on the case of a DS that has previously featured an FOPT due to the thermal tunneling of a dark Higgs field to a new VEV as described in detail in the last chapter. Moreover, we assume the DS to be decoupled from the particle species of the SM since some point in time before the phase transition, until it (re-)enters into contact with the SM thermal bath upon its decay. We further assume that the decaying DS consists of only one leftover species. Therefore, all other DS species are assumed to become Boltzmann-suppressed sufficiently long before the lightest dark sector species decays, to which we will refer as “the mediator” in this chapter. To be able to ignore the inverse decays from SM particles to the mediator, we will only consider non-relativistic decays thereof [24].

*Limits of this general description of the DS evolution*

### 3.1 WHAT IS A HOT DARK SECTOR?

We will start this chapter by defining what we precisely mean when we speak about “decaying hot dark sectors” and what the origin of experimental constraints on DSs are. Prior to that, it will prove to be useful to revisit the thermal bath formed by the frequent interactions of the SM photon.

Unlike most of the elementary particle species of the SM, photons are still abundant in the current Universe. Conversely, massive gauge bosons decayed as they are short-lived particles, quarks quickly became confined by forming bound states, and charged leptons and anti-leptons annihilated or bound to ionized nuclei. Moreover, contrary to neutrinos, photons were always<sup>1</sup> tightly coupled to other electrically charged particles, thus forming an LTE with the other species during large parts of the Hot Big Bang scenario. We will therefore refer to the

*The thermal bath of SM particles*

<sup>1</sup> Technically, this argument holds only after the EWPT, as before photons did not exist. At higher temperatures, however, the same argument would hold for the photons’ predecessors, the massless gauge bosons for weak isospin and hypercharge.

thermal bath that forms by the interaction of photons as the “SM bath” and denote its temperature with  $T_{\text{SM}}$ . Using this quantity, we can refer to different times in the primordial Universe. In fact, we already did so in the introduction, when we associated temperatures as well as times with the different epochs in the chronology of the Universe in Figure 2.2.

*Our definition of a hot dark sector*

Analogously to the SM bath, there can exist other, still unobserved sectors of particle physics without large couplings to the SM bath that form a distinct thermal bath with a different temperature. In fact, considering the amount of DM, it appears probable that sectors with BSM physics exist or had been important at some point in the evolution of the Universe [23]. We will thus define a thermal bath with a temperature  $T_{\text{DS}}$  with sufficiently low thermal contact to the particles of the SM as a dark sector. Further, if  $T_{\text{DS}} > T_{\text{SM}}$ , we say that the DS is “hot”.

*Two separate effects on  $\Lambda$ CDM cosmology*

The effect of a DS on the evolution of our Universe can in theory be due to two possible causes [24]: First, a DS contributes to the total energy density  $\rho_{\text{tot}}$  and will thus enlarge the Hubble parameter, effectively shortening the time-scales on which different processes in the Universe can take place. The second effect of a DS on cosmology is due to the possible interactions with SM particle species. While in the case of a perfectly secluded DS this point does not occur, an interaction between the sectors can lead to interesting effects. One example of a simple and rather well-understood dark sector are sterile neutrinos [23], which carry no SM charges and might explain some of the gaps in our theories, like DM, neutrino masses or baryogenesis.

*Experimental constraints on generic DSs*

Due to these two possible impacts on the  $\Lambda$ CDM cosmology, the parameter space of possible DSs can be constrained. First,  $\rho_{\text{tot}}$  cannot exceed the critical energy density  $\rho_c \equiv 3 m_{\text{pl}}^2 H^2$  as it would overclose the Universe (i. e., prevent it from attaining its present age through its early collapse). This constraint can be evaded by giving the lightest DS species, which could eventually dominate  $\rho_{\text{tot}}$  and exceed  $\rho_c$ , a decay channel to SM particles. However, if we evade this constraint by letting the DS decay to dispose of its energy density, there still exist stringent bounds on when this decay must have happened. In reference [12], it is argued that for sub-MeV DSs the main constraints come from CMB and BBN, as relativistic dark particles would change the dynamics of these processes by setting a different time-scale  $H^{-1}$  or reheating the photon or neutrino bath.

The constraints on account of these effects can be parameterized by the effective number of neutrino species, whose most conservative constraint  $N_{\text{eff}} = 2.99^{+0.34}_{-0.33}$  was obtained by the Planck collaboration in 2018 by combining several individual measurements of the CMB anisotropies and polarization, and baryon acoustic oscillations [16].

The constraints on  $N_{\text{eff}}$ , which stem from the changes in the predicted light element abundance by additional relativistic particles at BBN still being consistent with observations, are of similar strength [16]. A detailed analysis shows that due to these tight constraints, light thermal relics decoupling after the QCD phase transition can be ruled out at 95 % significance (see Figure 36 in reference [16]). While Breitbach et al. incorporate these constraints by focusing on DSs colder than the SM bath [12], our approach will be to let the hot DS decay sufficiently long before the QCD phase transition starts. The mass scale of the DS in the following analysis in chapter 4 will therefore lie above 1 GeV.

*Evading constraints through an early DS decay*

To study the effects of an additional DS on the evolution of the Universe, we have to follow the procedure described in chapter 2: After having added an additional energy density  $\rho_{\text{DS}}$  (including the contributions from all DS particle species) to  $\rho_{\text{tot}}$  within the first Friedmann equation (2.4a), we will have to describe the effects of possible interactions of DS particles with each other and SM particles. As we concentrate on the specific case of an initially completely secluded DS, the only relevant interactions are between DS states. Assuming sufficiently strong interactions between the DS species, an LTE forms between them such that the discussion from chapter 2.2.2.5 holds. This will allow us to describe the two sectors as two individual thermal baths whose dynamics can be expressed using effective DOFs, which will be the aim of the following section 3.2.

*The structure of this chapter*

At some point, only the lightest DS species survives, as the heavier DS particles become Boltzmann suppressed (see equation (2.26a)). The DS temperature at which this chemical decoupling occurs is denoted by  $T_{\text{DS}}^{\text{cd}}$ . After the chemical decoupling, the mediator evolution will therefore deviate by what would be dictated by an LTE. We will investigate its out-of-equilibrium evolution in section 3.3. Finally, the mediator will live up to its name and decay into SM particles, bringing the two thermal baths into contact. The equations underlying this process will be derived and solved numerically in section 3.4. The overall effect of the decay of the DS on the earlier produced SGWB will then be investigated in section 3.5.

## 3.2 LOCAL THERMAL EQUILIBRIUM OF THE DARK SECTOR

As mentioned before, we can introduce effective DOFs to elegantly refer to more than one particle species at once contributing to a thermodynamic quantity like the energy or entropy density. The usual notion of effective DOFs is the mere sum of the bosonic and fermionic DOFs (the latter coming with a respective prefactor of 7/8) of particles

*Why introduce effective DOFs?*

being relativistic at a given temperature  $T_{\text{SM}}$ , see e. g. equation (3.62) in reference [6]. We will extend this concept to a more general expression. This specification is of particular importance when dealing with particles which move too slow to be referred to as ultra-relativistic or too fast to be considered non-relativistic. Additionally, it allows us to specify the impact of the temperature ratio between the DS and SM bath, which we will denote by

$$\zeta(T_{\text{SM}}) \equiv \frac{T_{\text{DS}}}{T_{\text{SM}}}. \quad (3.1)$$

*Definition of the temperature ratio  $\zeta$*

Note that this quantity is in general not a constant, but rather a function of time or, equivalently,  $T_{\text{SM}}$ . This is due to the separate conservation of entropy in the two sectors until the mediator decays. When in one of the sectors a particle species drops out of LTE, its entropy gets dumped into the coupled, remaining species which therefore get reheated. In fact, as we will see, the introduction of effective DOFs will allow us to quantify and calculate the time dependence of the temperature ratio  $\zeta$ .

The energy density and the pressure of an individual species  $x$  in LTE can be calculated by integrating over its thermal (Bose-Einstein or Fermi-Dirac) distribution function as it was shown in section 2.2.2.5. If the chemical potential  $\mu_x$  vanishes, the calculations simplify to

$$\rho_x(T_x) = \frac{g_x T_x^4}{2 \pi^2} \int_{z_x}^{\infty} du_x \frac{u_x^2 \sqrt{u_x^2 - z_x^2}}{e^{u_x} \pm 1}, \quad (3.2a)$$

$$P_x(T_x) = \frac{g_x T_x^4}{6 \pi^2} \int_{z_x}^{\infty} du_x \frac{(u_x^2 - z_x^2)^{3/2}}{e^{u_x} \pm 1}, \quad (3.2b)$$

$$\begin{aligned} s_x(T_x) &= \frac{\rho_x(T_x) + P_x(T_x)}{T_x} \\ &= \frac{g_x T_x^3}{2 \pi^2} \int_{z_x}^{\infty} du_x \left[ \frac{u_x^2 \sqrt{u_x^2 - z_x^2}}{e^{u_x} \pm 1} + \frac{1}{3} \frac{(u_x^2 - z_x^2)^{3/2}}{e^{u_x} \pm 1} \right], \end{aligned} \quad (3.2c)$$

where the substitutions  $u_x = \sqrt{m_x^2 + p^2}/T_x$ , and  $z_x = m_x/T_x$  are employed, a + (−) sign refers to a fermionic (bosonic) species  $x$  and the penultimate line follows from equation (2.24). Comparing to equation (2.25b), we can now define the effective DOF of an individual species by dividing these thermodynamic quantities by the respective quantity that one would obtain for an ultra-relativistic bosonic species with the same temperature and one intrinsic DOF, hence [53]

*Definition of effective DOFs for a single species in LTE*

$$g_{\text{eff},\rho}^x(T_x) \equiv \frac{\rho_x(T_x)}{\rho_{\text{bos}}^{\text{rel}}(T_x)|_{g=1}} = g_x \frac{15}{\pi^4} \int_{z_x}^{\infty} du_x \frac{u_x^2 \sqrt{u_x^2 - z_x^2}}{e^{u_x} \pm 1}, \quad (3.3a)$$

$$g_{\text{eff},P}^x(T_x) \equiv \frac{P_x(T_x)}{P_{\text{bos}}^{\text{rel}}(T_x)|_{g=1}} = g_x \frac{15}{\pi^4} \int_{z_x}^{\infty} du_x \frac{(u_x^2 - z_x^2)^{3/2}}{e^{u_x} \pm 1}, \quad (3.3b)$$

$$g_{\text{eff},s}^x(T_x) = \frac{3g_{\text{eff},\rho}^x(T_x) + g_{\text{eff},P}^x(T_x)}{4}, \quad (3.3c)$$

where  $\rho_{\text{bos}}^{\text{rel}}(T_x)|_{g=1} = \frac{\pi^2}{30} T_x^4$  and  $P_{\text{bos}}^{\text{rel}}(T_x)|_{g=1} = \frac{\pi^2}{90} T_x^4$ .

The effective DOFs for a thermal bath of particles with a common temperature can now be defined as the sum over the individual effective DOFs of its constituents. In our case, where the total system is given by a thermal bath of SM and DS particles, we therefore obtain the following expressions for the total energy and entropy densities

$$\begin{aligned} \rho_{\text{tot}}(T_{\text{SM}}) &= \rho_{\text{SM}}(T_{\text{SM}}) + \rho_{\text{DS}}(T_{\text{SM}}) \\ &= \left[ g_{\text{eff},\rho}^{\text{SM}}(T_{\text{SM}}) + g_{\text{eff},\rho}^{\text{DS}}(T_{\text{SM}}) \zeta^4(T_{\text{SM}}) \right] \frac{\pi^2}{30} T_{\text{SM}}^4, \end{aligned} \quad (3.4a)$$

$$\begin{aligned} s_{\text{tot}}(T_{\text{SM}}) &= s_{\text{SM}}(T_{\text{SM}}) + s_{\text{DS}}(T_{\text{SM}}) \\ &= \left[ g_{\text{eff},s}^{\text{SM}}(T_{\text{SM}}) + g_{\text{eff},s}^{\text{DS}}(T_{\text{SM}}) \zeta^3(T_{\text{SM}}) \right] \frac{2\pi^2}{45} T_{\text{SM}}^3, \end{aligned} \quad (3.4b)$$

where  $g_{\text{eff},\rho}^{\text{SM}}$  ( $g_{\text{eff},s}^{\text{SM}}$ ) denote the effective energy (entropy) DOFs for the photon bath. The analog notation is used for the DOFs of the DS. Note, however, that the dark DOFs have a much higher influence on  $\rho_{\text{tot}}$  and  $s_{\text{tot}}$  than SM particles in the case of a hot DS (i. e.,  $\zeta > 1$ ). This effect is shown in Figure 3.1 for two hot dark sector species in addition to the particles of the SM bath for  $\zeta = 2$ . There and in the following, the quantities in square brackets in (3.4a) and (3.4b) are referred to as  $g_{\text{eff},\rho}^{\text{tot}}(T_{\text{SM}})$  and  $g_{\text{eff},s}^{\text{tot}}(T_{\text{SM}})$ , respectively.

To calculate the temperature dependence of  $\zeta(T_{\text{SM}})$ , remember that from equation (2.18) follows that the entropy of the two decoupled baths is conserved individually. Thus,  $S_y = \frac{2\pi^2}{45} g_{\text{eff},s}^y T_y^3 a^3$  is a constant, where  $y$  denotes the SM bath or the DS. Dividing  $S_{\text{DS}}$  by  $S_{\text{SM}}$ , replacing  $T_{\text{DS}}/T_{\text{SM}}$  by  $\zeta$  and then solving for  $\zeta$  leads to

$$\zeta(T_{\text{SM}}) = \tilde{\zeta} \left( \frac{g_{\text{eff},s}^{\text{SM}}}{\tilde{g}_{\text{eff},s}^{\text{SM}}} \right)^{1/3} \left( \frac{\tilde{g}_{\text{eff},s}^{\text{DS}}}{g_{\text{eff},s}^{\text{DS}}} \right)^{1/3}. \quad (3.5)$$

Here, the quantities with a tilde specify a point in time where the sectors have already been decoupled and  $\tilde{\zeta}$ ,  $\tilde{g}_{\text{eff},s}^{\text{SM}}$ , and  $\tilde{g}_{\text{eff},s}^{\text{DS}}$  are known, while the quantities without a tilde are evaluated at  $T_{\text{SM}}$ . Note that this equation cannot be used immediately to calculate the temperature ratio  $\zeta$  at a given temperature  $T_{\text{SM}}$  since  $\tilde{g}_{\text{eff},s}^{\text{DS}}$  and  $\tilde{g}_{\text{eff},s}^{\text{SM}}$  have to be known at  $T_{\text{SM}}$ . This, however, is not trivial since  $T_{\text{DS}} = \zeta T_{\text{SM}}$  would already had to be known to calculate the effective DOFs of the DS. Therefore, equation (3.5) is a self-consistent relation and has to be solved numerically. This can be done for a given temperature  $T_{\text{SM}}$  by minimizing the difference of the left- and right-hand side by varying  $\zeta(T_{\text{SM}})$ . The general result of this discussion is that the temperature of the DS increases (decreases) when the dark DOFs  $\tilde{g}_{\text{eff},s}^{\text{DS}}$  (the DOFs of the SM  $\tilde{g}_{\text{eff},s}^{\text{SM}}$ ) decrease.

*Effective DOFs of thermal baths*

*Why the temperature ratio  $\zeta$  is important*

*The time evolution of the temperature ratio*

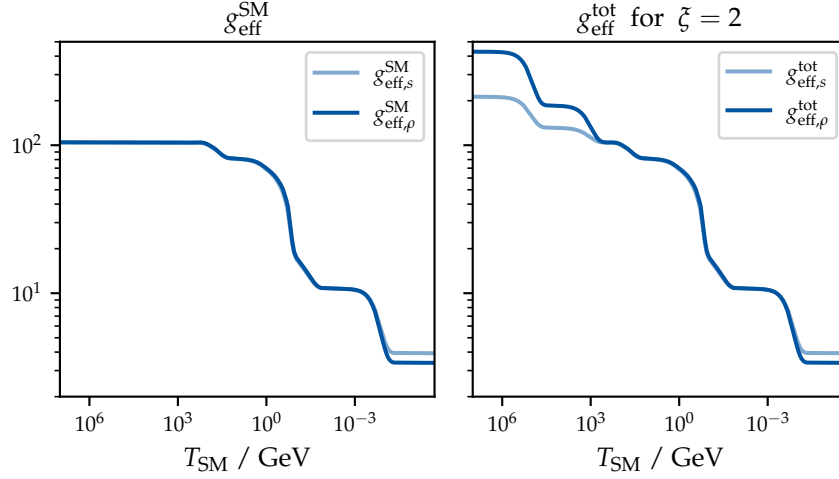


**Figure 3.1:** The temperature evolution of the effective DOFs of the SM (*left*) and the total system, including also a DS (*right*), assuming that the DS particle species follow their equilibrium distributions for all times. This dark sector consists of a dark photon with mass  $m_{\text{DP}} = 10^6 \text{ GeV}$  (and three internal DOFs) and a dark Higgs with mass  $m_{\text{DH}} = 10^4 \text{ GeV}$  (and one internal DOF). The temperature ratio between the two thermal baths was fixed to  $\zeta = 2$  to show that a DS slightly hotter than the SM bath can already yield interesting new dynamics. A possible temperature dependence of  $\zeta(T_{\text{SM}})$  as it would arise from the reheating of either sector was ignored here. The data for the effective DOFs of the SM has been taken from the ancillary material of reference [54].

A final remark should be added concerning the assumption that the DS species follow an LTE: While for large parts of its evolution the description using effective DOFs is meaningful, a detailed study of out-of-equilibrium processes is necessary when there is left only one massive particle species in the DS without available decay channels. Given a sufficiently long lifetime, this species will therefore leave equilibrium and can no longer be described by the methods presented in this chapter. The discussion of the mediator's out-of-equilibrium decay will be given in section 3.4, while the next chapter will focus on the evolution of the mediator species before its decay. The description will start at the point when the other DS species become Boltzmann-suppressed, freeze out of the LTE and therefore decouple from the mediator.

*The breakdown of the assumption of LTE*

### 3.3 OUT-OF-EQUILIBRIUM EVOLUTION OF THE MEDIATOR SPECIES

As described in section 2.2.2.3, in the case of a decay, the Boltzmann equation for the evolution of the decaying species is a simple ODE that can be integrated, when the scale factor-time dependence  $a(t)$  is known. Assuming a particular evolution of the scale factor  $a(t)$ , we can thus obtain  $\rho_{\text{med}}(t)$  for our dark mediator by further integrating its distribution function over momentum space as it was presented in equation (2.16a). This procedure is, however, numerically expensive, since every point in time requires an individual integration over momentum space, see equation (4.7) in reference [24]. The aim of this section will be to derive a simple approximation that we can use to describe the thermal history of the mediator species since its chemical decoupling until its decay.

*Integrating the Boltzmann equation is numerically expensive*

#### 3.3.1 A first approximation for non-relativistic decays

Motivated by the approach presented in reference [13] and extending it to also allow for an initially relativistic mediator, we will start our discussion using the approximation

$$\frac{d\rho_{\text{med}}}{dt} = -3\zeta(t)H(t)\rho_{\text{med}}(t) - \Gamma\rho_{\text{med}}(t), \quad (3.6)$$

where  $\Gamma$  is the decay width of the mediator species,  $\zeta(t) = 4/3$  when the mediator behaves relativistically, and  $\zeta(t) = 1$  if it moves non-relativistically. Moreover, equation (3.2a) can be used to calculate a starting condition  $\rho_{\text{med}}^{\text{cd}} \equiv \rho_{\text{med}}(T_{\text{SM}}^{\text{cd}})$  for the ODE specified in equation (3.6). Here and in the following, the index “cd” denotes the chemical decoupling of the heavier DS particle species from the mediator. We introduce the dimensionless time measure  $\theta \equiv \Gamma t$  and the normalized scale factor  $\bar{a} \equiv a/a_{\text{cd}}$ . Denoting derivatives with respect to  $\theta$  by a prime, the approximation can be written as

*Approximation, assuming non-relativistic decays*

$$\rho'_{\text{med}}(\theta) = -3\zeta(\theta)\frac{\bar{a}'}{\bar{a}}\rho_{\text{med}}(\theta) - \rho_{\text{med}}(\theta). \quad (3.7)$$

A plot of the resulting  $\rho_{\text{med}}(\theta)$  can be found in Figure 3.2, where we compare it to the curve obtained by integrating the corresponding Boltzmann equation. We found that a good overall agreement between the curves can be achieved, when we perform the transition from  $\zeta = 4/3$  to  $\zeta = 1$  at the dimensionless time of  $\tilde{\theta} = 7\theta_{\text{cd}}(T_{\text{DS}}^{\text{cd}}/m_{\text{med}})^2$ . For  $\theta < \tilde{\theta}$ , the mediator behaves as a relativistic particle species, whose energy density scales with  $\rho_{\text{med}} \propto a^{-4}$ , while for  $\theta > \tilde{\theta}$  its energy density scales with  $\rho_{\text{med}} \propto a^{-3}$ , since it behaves as non-relativistic

matter. For  $\theta \gtrsim 1$ , the decay of the mediator becomes relevant such that the energy density decreases exponentially as  $\rho_{\text{med}} \bar{a}^3 \propto \exp(-\theta)$ .

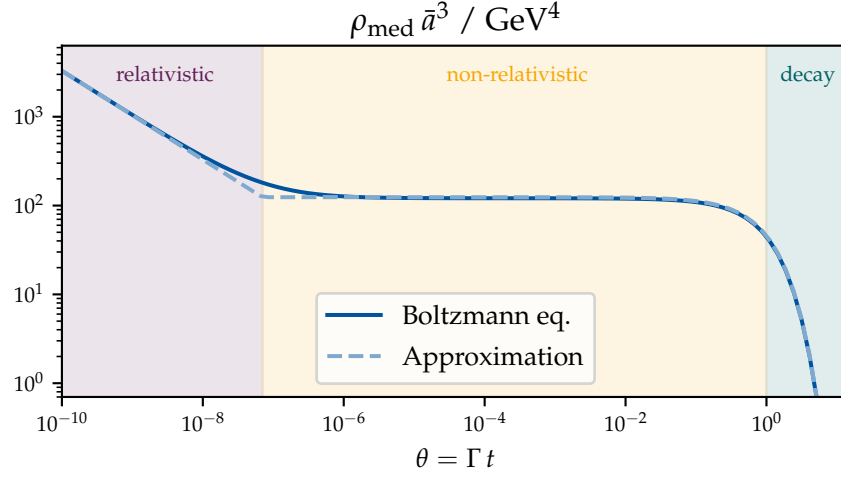


**Figure 3.2:** Time evolution of the comoving energy density  $\rho_{\text{med}} \bar{a}^3$  of a dark Higgs with mass  $m_{\text{DH}} = 1 \text{ GeV}$  acting as a mediator between the DS and the SM particles. The decoupling of other DS species from the mediator occurs at  $\theta_{\text{cd}} = 10^{-10}$  when  $T_{\text{DS}}^{\text{cd}} = 10 \text{ GeV}$ . The time parameter, after which the mediator no longer behaves as a relativistic particle species, therefore amounts to  $\tilde{\theta} = 7 \cdot 10^{-8}$ . The solid line refers to the subsequent evolution of  $\rho_{\text{med}}$  obtained by integrating the Boltzmann equation (2.13), whereas the dashed line shows the result of the integration of the employed approximation (3.7). The approximation matches the results of the Boltzmann equation for times  $\theta$  sufficiently far away from  $\tilde{\theta}$ , when the mediator is still relativistic or has already become non-relativistic. The calculation assumed that the scale factor behaves as in radiation domination at all times, i. e.  $a \propto \sqrt{t}$ , such that  $\bar{a} = \sqrt{\theta/\theta_{\text{cd}}}$  and  $\bar{a}'/\bar{a} = (2\theta)^{-1}$ .

Note that the assumed time dependence of  $\rho'_{\text{med}}$  only describes the evolution of  $\rho_{\text{med}}$ , as it is encoded in the Boltzmann equation, well in the regions that lie sufficiently far from  $\theta \simeq \tilde{\theta}$ . Additionally, it should be noted that the used approximation only holds well for the case of non-relativistic decays. If  $\theta_{\text{cd}} \gtrsim 1$ , the mediator's lifetime is so short, that it will decay just after having dropped out of equilibrium with the other DS species. In that case, the mediator would decay while still being relativistic and we would have to account for the time dilation between the mediator's rest frame and the comoving frame of the expanding FLRW metric, which would result in an exponential decay with a lifetime effectively prolonged by a time-averaged Lorentz factor [24]. We will therefore focus on the case where  $\theta_{\text{cd}} < 1$ .

*Validity of our approximation*

### 3.3.2 Cannibalism

So far, we ignored self-interactions of the mediator and focused on its decay to SM particles to describe its time evolution. This description is, however, incomplete. As was first argued in reference [55], a secluded particle species can perform number-changing processes like  $3 \rightarrow 2$  or  $4 \rightarrow 2$ , thereby reducing its comoving number density while conserving its entropy. This leads to an unusual relationship between its energy density and the scale factor until the number-changing processes become ineffective. Since in this process the species consumes itself to keep warm<sup>2</sup> for a longer period of time than usually, it is casually referred to as “cannibalistic” [56].

*The mediator becomes a cannibal to keep warm*

Self-interactions of the mediator have not been included into the Boltzmann equation (2.13) and thus did not lead to any visible effect in Figure 3.2. We will directly include cannibalism into our approximation by modifying the function  $\zeta(\theta)$ . To do so, we split our description in two parts: First, there is a period of chemical equilibrium in which the chemical potential of the mediator vanishes, such that number-changing processes can be effective. Since the chemical potential eventually increases until  $\mu_{\text{med}} = m_{\text{med}}$  is reached, when the mediator gets non-relativistic, its number density is fixed in a second period that we will consider separately. A detailed overview of the different processes and how a phase of cannibalism could be included into the description of  $\rho_{\text{med}}$  using a Boltzmann equation can be found in reference [25].

*Simplification:  
 $\mu_{\text{med}} = 0$  is followed  
by  $\dot{N}_{\text{med}} = 0$*

At early times and high temperatures, the mediator’s chemical potential can be neglected. Therefore, equations (3.2a), and (3.2c) hold, where  $x$  now describes the mediator species. Since the integrals in these functions only depend on  $z_{\text{med}} \equiv m_{\text{med}}/T_{\text{DS}}$ , we can obtain a function  $\bar{s}_{\text{med}}(\bar{\rho}_{\text{med}})$ , where  $\bar{s}_{\text{med}} \equiv 2\pi^2 s_{\text{med}}/(g_{\text{med}} T_{\text{DS}}^3)$  and  $\bar{\rho}_{\text{med}} \equiv 2\pi^2 \rho_{\text{med}}/(g_{\text{med}} T_{\text{DS}}^4)$ , by eliminating  $z_{\text{med}}$ . In fact, as  $z_{\text{med}}$  was the only quantity that specified the physical properties of the mediator, the function  $\bar{s}_{\text{med}}(\bar{\rho}_{\text{med}}) = \bar{s}(\bar{\rho})$  is completely general and can be used for arbitrary particle species with vanishing chemical potential. Knowing that the DS entropy is conserved before the sectors equilibrate through the mediator’s decay, we can use this function to calculate the energy density of the mediator species. To do so, note that the conservation of the comoving mediator entropy  $s_{\text{med}} a^3 = \text{const}$  can be expressed as

*When  $\mu_{\text{med}} = 0$ , the function  $\bar{s}(\bar{\rho})$  exists, since  $z_{\text{med}}$  can be eliminated*

$$\frac{d \ln s_{\text{med}}}{dt} = \frac{d \ln s_{\text{med}}}{d \ln \rho_{\text{med}}} \frac{\dot{\rho}_{\text{med}}}{\rho_{\text{med}}} = -3 H(t), \quad (3.8)$$

from which it follows that

$$\dot{\rho}_{\text{med}} = -3 \frac{d \ln \rho_{\text{med}}}{d \ln s_{\text{med}}} H(t) \rho_{\text{med}}(t). \quad (3.9)$$

<sup>2</sup> “Warm” in this context denotes a particle species that is neither relativistic nor non-relativistic, but somewhere in between with  $m \sim T$ .

Since

$$\frac{d \ln \rho_{\text{med}}}{d \ln s_{\text{med}}} = \frac{d \rho_{\text{med}} s_{\text{med}}}{d s_{\text{med}} \rho_{\text{med}}} = \frac{d \bar{\rho}_{\text{med}} \bar{s}_{\text{med}}}{d \bar{s}_{\text{med}} \bar{\rho}_{\text{med}}} = \frac{d \ln \bar{\rho}_{\text{med}}}{d \ln \bar{s}_{\text{med}}} = \frac{d \ln \bar{\rho}}{d \ln \bar{s}}, \quad (3.10)$$

*Smooth transition to non-relativistic behavior described by  $\frac{d \ln \bar{\rho}}{d \ln \bar{s}}$*

we can replace the differential in equation (3.9) by the smooth function  $\frac{d \ln \bar{\rho}}{d \ln \bar{s}}(\rho_{\text{med}})$ . This function is close to  $4/3$  for large energy densities  $\rho_{\text{med}}$ , corresponding to high temperatures and relativistic species, and approaches  $1$  for low energy densities  $\rho_{\text{med}}$ , corresponding to non-relativistic species. These limits can be understood by comparing equation (3.9) to the mediator's volume heating rate  $\dot{q}_{\text{med}} \equiv \dot{\rho}_{\text{med}} + 3 H [\rho_{\text{med}} + P_{\text{med}}] = 0$ , which vanishes without heat exchange between the dark sector and the SM bath (see the comment below equation (2.18)). Thus, we can identify the function with  $\frac{d \ln \bar{\rho}}{d \ln \bar{s}}(\rho_{\text{med}}) = 1 + \frac{P_{\text{med}}}{\rho_{\text{med}}}$ . From the evaluation of the relativistic and non-relativistic limits in section 2.2.2.5 we moreover know that the pressure of a non-relativistic fluid becomes negligible compared to its energy density (i. e.,  $P_{\text{med}}/\rho_{\text{med}} \ll 1$ ) and that for a relativistic fluid  $P_{\text{med}}/\rho_{\text{med}} \simeq 1/3$  holds. Hence,  $\frac{d \ln \bar{\rho}}{d \ln \bar{s}}$  can be seen as a function describing the smooth transition from the relativistic to the non-relativistic behavior of a particle species, as long as its chemical potential vanishes.

*When  $\dot{N}_{\text{med}} = 0$ , the previous discussion holds*

Conversely, when number-changing processes become inefficient, the chemical potential  $\mu_{\text{med}}$  can no longer be neglected. Thus, the function  $\bar{s}_{\text{med}}(\bar{\rho}_{\text{med}})$  cannot be easily obtained by eliminating  $z_{\text{med}}$  or replaced by a generic function  $\bar{\rho}(\bar{s})$ . However, when number-changing processes are inefficient, the comoving number density of the mediator is conserved, such that our description from the previous section holds.

To account for a cannibalistic phase in the evolution of the mediator, we can therefore define<sup>3</sup>

$$\zeta(\theta) = \begin{cases} \frac{d \ln \bar{\rho}}{d \ln \bar{s}}(\rho_{\text{med}}) & \text{for } \Gamma_{\text{nc}}(\theta) \geq H(\theta) \\ \frac{4}{3} & \text{for } \Gamma_{\text{nc}}(\theta) < H(\theta), \quad \theta < \tilde{\theta} \\ 1 & \text{for } \Gamma_{\text{nc}}(\theta) < H(\theta), \quad \theta \geq \tilde{\theta} \end{cases}, \quad (3.11)$$

*Extend previous approximation by modifying  $\zeta(\theta)$*

which can be used in equation (3.7) instead of the previously used function  $\zeta(\theta)$  that implicitly assumed  $\Gamma_{\text{nc}} < H$  for all time parameters  $\theta$ . Here,  $\Gamma_{\text{nc}}$  denotes the rate with which number-changing processes occur, which can be approximated by the  $3 \rightarrow 2$  rate  $\Gamma_{32} \simeq \langle \sigma_{32} v^2 \rangle n_{\text{med}}^2$

<sup>3</sup> The case where  $\theta < \tilde{\theta}$  for  $\Gamma_{\text{nc}} < H$  should never occur, since in that case the number-changing processes end while the mediator is still relativistic. While scanning over the parameter space of the model described in chapter 4, we could not identify a single case where this condition is fulfilled. This case is therefore noted only for completeness, here.

[57]. The thermally averaged cross section of the  $3 \rightarrow 2$  process is given by

$$\langle \sigma_{32} v^2 \rangle = \frac{25 \sqrt{5} \alpha_{32}^3}{3072 \pi m_{\text{med}}^5} + \mathcal{O} \left( \frac{T_{\text{DS}}}{m_{\text{med}}} \right) \quad (3.12)$$

for a scalar mediator. If the scalar's potential is specified as  $V(\phi) = \frac{m^2}{2} \phi^2 + \frac{\kappa_3}{3!} \phi^3 + \frac{\kappa_4}{4!} \phi^4$ , the effective  $3 \rightarrow 2$  coupling is fixed by [56, 57]

$$(4 \pi \alpha_{32})^3 \equiv \left( \frac{\kappa_3}{m} \right)^2 \left[ \left( \frac{\kappa_3}{m} \right)^2 + 3 \kappa_4 \right]^2. \quad (3.13)$$

In the case of the dark Higgs described by the Lagrangian density in equation (2.35), the effective  $3 \rightarrow 2$  coupling therefore reads  $\alpha_{32} = 9 \lambda / (2^{1/3} \pi) \simeq 2.3 \lambda$  due to the effective  $\phi^3$  term produced in the phase transition with a coupling  $\kappa_3/3! = \lambda v$ , the quartic coupling  $\kappa_4/4! = \lambda/4$  and the dark Higgs mass reading  $m = \sqrt{2} \lambda v$ .

*Assume  $\mu_{\text{med}} = 0$  as long as  $\Gamma_{32} > H$*

To calculate the rate of number-changing processes  $\Gamma_{\text{nc}} \simeq \Gamma_{32}$  to define an ending condition for the cannibalistic phase, the mediator's number density has to be known. Since the end of cannibalism is expected to eventuate when the mediator species is non-relativistic (see footnote 3), this quantity can be calculated approximately using the result from equation (2.26b),  $n_{\text{med}} \simeq \rho_{\text{med}}/m_{\text{med}}$ .

A plot of the resulting time evolution of  $\rho_{\text{med}} \bar{a}^3$  and  $s_{\text{med}} \bar{a}^3$  including an intermediate phase of cannibalism (with the same set of parameters used already in Figure 3.2) can be found in Figure 3.3. In the violet and red shaded areas,  $\Gamma_{\text{nc}} \geq H$  holds, such that number-changing processes can occur, the effect of  $\mu_{\text{med}}$  on the mediator energy and entropy density is negligible, and  $\zeta(\theta)$  follows the gradual decrease from  $4/3$  to  $1$  as described above. The end of the violet area is marked by  $\theta = \tilde{\theta}$ . Since  $3 \rightarrow 2$  processes are efficient, however, the mediator energy density does not follow the  $\propto a^{-3}$  scaling of non-relativistic matter, but rather scales as  $\rho_{\text{med}} \bar{a}^3 \propto 1/\ln \bar{a}$  afterwards [25]. The end of the cannibalistic period is fixed by the number-changing processes becoming ineffective (i. e.,  $\Gamma_{\text{nc}} < H$ ), as soon as the mediator number density  $n_{\text{med}}$  sinks below a certain threshold value fixed by the effective coupling  $\alpha_{32}$ , the mediator mass and the Hubble parameter. From this point in time on, the expected behavior for a non-relativistic decay,  $\rho_{\text{med}} \propto a^{-3} \exp(-\theta)$ , is restored. As one can see on the right-hand side of Figure 3.3, entropy is conserved throughout these phases and only decreases upon the decay of the dark sector. Comparing to Figure 3.2, for which the same physical parameters had been used, shows that the non-relativistic mediator energy density is lower when an intermediate phase of cannibalism occurred beforehand. This is due to a longer period in which the mediator energy density can decrease due to its redshift. Eventually, this leads to less energy that can be injected into the SM bath and a less severe reheating of the SM bath, as will be shown in the next section.

*Exponential decrease of  $\rho_{\text{med}} \bar{a}^3$  during cannibalism*

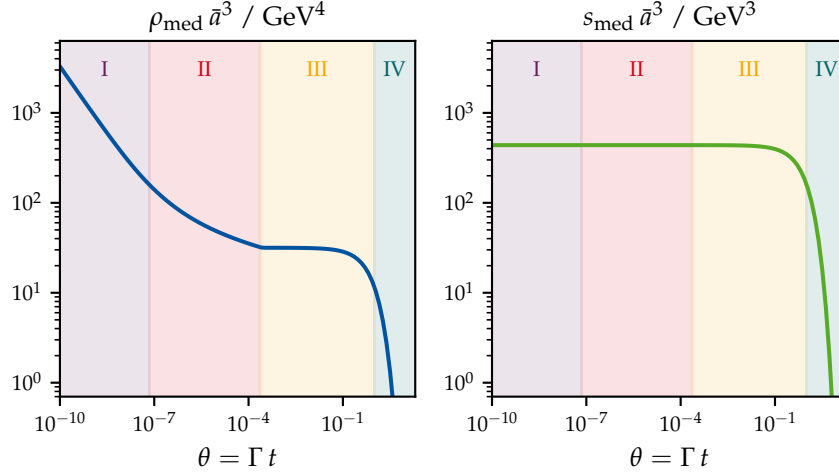


**Figure 3.3:** *Left:* Plot of time evolution of the dark Higgs mediator species with the same specifications as in Figure 3.2, but with an intermediate phase of cannibalism. In the area shaded in violet (I), the mediator species is still relativistic, such that  $\rho_{\text{med}} \propto \bar{a}^{-4}$ , while in the red area (II), number-changing processes lead to a decrease of  $\rho_{\text{med}} \bar{a}^3 \propto 1/\ln \bar{a}$  with the normalized scale factor  $\bar{a}$ . In the area shaded yellow (III), the mediator starts to decay non-relativistically, i. e.  $\rho_{\text{med}} \bar{a}^3 \propto e^{-\theta}$ , and in the blue shaded area (IV), we have  $\theta > 1$ , indicating the decay of the mediator becoming the dominant effect. The effective  $3 \rightarrow 2$  coupling was fixed to  $\alpha_{32} = 10^{-2}$ . *Right:* The entropy  $s_{\text{med}} \bar{a}^3$  is conserved until the mediator species decays.

### 3.4 INJECTING ENTROPY INTO THE SM

Until now, we always assumed a background evolution of the scale factor as it would be the case in radiation domination, that is  $a \propto \sqrt{t}$ . However, this does not have to be the case when we add a non-relativistic species to the particle content of the  $\Lambda$ CDM model. In fact, given a sufficiently long lifetime of the mediator species, the Universe will inevitably go through a period of early matter domination until it reenters into the radiation domination described by the  $\Lambda$ CDM model. Such an intermediate period can have profound impacts on a frozen out abundance of DM [13] and, as we will show, on the SGWB that has been produced before. The general reason behind this is that the secluded mediator will not follow its equilibrium distribution as described in equation (2.26a), since it cannot dispose of its energy into less massive particle particles in the DS and cannot become Boltzmann suppressed. The mediator can therefore dominate the total energy density of the Universe and inject a considerable amount of entropy into the SM bath upon its decay [6, 58]. To describe the interplay between the scale factor and the evolution of the different sources of

*The DS can lead to an early matter domination*

energy, namely the SM radiation, the decaying DS and possibly also decoupled DM, we will couple the presented ODE for the evolution of  $\dot{\rho}_{\text{med}}$  with the first Friedmann equation and solve the resulting set of coupled differential equations numerically.

### 3.4.1 Derivation of the equations governing the entropy injection

We start the derivation by noting that the entropy of the SM in a comoving volume  $a^3$  is given by  $S_{\text{SM}}(t) = \frac{2\pi^2}{45} g_{\text{eff},s}^{\text{SM}}(t) T_{\text{SM}}^3(t) a^3(t)$  in accordance with equation (3.4b). From this, we find that the temperature of the SM bath can be obtained by rearranging

$$T_{\text{SM}}(t) = \left( \frac{45}{2\pi^2} \right)^{1/3} \left( \frac{S_{\text{SM}}(t)}{g_{\text{eff},s}^{\text{SM}}(t)} \right)^{1/3} \frac{1}{a(t)}. \quad (3.14)$$

Using this, the energy density of the SM radiation can be expressed as

$$\rho_{\text{rad}}(t) = \frac{\pi^2}{30} g_{\text{eff},\rho}^{\text{SM}}(t) T_{\text{SM}}^4(t) \quad (3.15)$$

$$= \frac{3}{4} \left( \frac{45}{2\pi^2} \right)^{1/3} \left( \frac{S_{\text{SM}}(t)}{g_{\text{eff},s}^{\text{SM}}(t)} \right)^{4/3} \frac{g_{\text{eff},\rho}^{\text{SM}}(t)}{a^4(t)}. \quad (3.16)$$

The increase in the radiation energy density since the chemical decoupling of the mediator from the other DS particles can therefore be quantified by

$$\frac{\rho_{\text{rad}}(t)}{\rho_{\text{rad}}^{\text{cd}}} = \frac{g_{\text{eff},\rho}^{\text{SM}}(t)}{g_{\text{eff},\rho}^{\text{SM,cd}}} \left( \frac{g_{\text{eff},s}^{\text{SM,cd}}}{g_{\text{eff},s}^{\text{SM}}(t)} \right)^{4/3} \left( \frac{S_{\text{SM}}(t)}{S_{\text{SM}}^{\text{cd}}} \right)^{4/3} \bar{a}^{-4}. \quad (3.17)$$

Employing the dimensionless time parameter  $\theta = \Gamma t$ , the first Friedmann equation (2.4a) reads  $H^2 = \Gamma^2 \left( \frac{\bar{a}'}{\bar{a}} \right)^2 = \frac{\rho_{\text{tot}}}{3 m_{\text{pl}}^2}$ . Neglecting curvature and dark energy, whose effects are not of importance in the early Universe, the total energy density is given by  $\rho_{\text{tot}} = \rho_{\text{med}} + \rho_{\text{mat}} + \rho_{\text{rad}}$ . Here,  $\rho_{\text{mat}}$  describes the influence of an already frozen-out DM density<sup>4</sup>, which therefore scales as  $\rho_{\text{mat}} = \rho_{\text{mat}}^{\text{cd}} \bar{a}^{-3}$ . The Friedmann equation thus reads

$$\begin{aligned} \bar{a}'(\theta) &= \bar{a}(\theta) \sqrt{\frac{\rho_{\text{med}}(\theta) + \rho_{\text{mat}}(\theta) + \rho_{\text{rad}}(\theta)}{3 m_{\text{pl}}^2 \Gamma^2}} \\ &= \frac{\bar{a}(\theta)}{\theta_{\text{H}}} \sqrt{\frac{\rho_{\text{med}}(\theta)}{\rho_{\text{med}}^{\text{cd}}} + \frac{\rho_{\text{mat}}^{\text{cd}} \rho_{\text{mat}}(\theta)}{\rho_{\text{med}}^{\text{cd}} \rho_{\text{mat}}^{\text{cd}}} + \frac{\rho_{\text{rad}}^{\text{cd}} \rho_{\text{rad}}(\theta)}{\rho_{\text{med}}^{\text{cd}} \rho_{\text{rad}}^{\text{cd}}}}, \quad (3.18) \end{aligned}$$

<sup>4</sup> Since our model investigated in chapter 4 does not include a DM candidate and we are describing processes in the very early Universe, we will assume that  $\rho_{\text{mat}}$  is negligible in all of the following numerical calculations. In the analytical work presented in this chapter, we will however also show the impact of a frozen-out matter density to facilitate further investigations.

*The first Friedmann equation, including a DS injecting entropy to the SM*

where the time scale  $\theta_H \equiv \sqrt{3 m_{\text{Pl}}^2 \Gamma^2 / \rho_{\text{med}}^{\text{cd}}}$  has been introduced in the last step. We define the first quantity in the square root as  $r(\theta) \equiv \rho_{\text{med}}(\theta) / \rho_{\text{med}}^{\text{cd}}$ , to be able to refer to the mediator energy density as a dimensionless quantity. To simplify the last two terms in the square root, we further introduce the constants  $f_{\text{mat}} \equiv \rho_{\text{mat}}^{\text{cd}} / \rho_{\text{med}}^{\text{cd}}$  and  $f_{\text{rad}} \equiv \rho_{\text{rad}}^{\text{cd}} / \rho_{\text{med}}^{\text{cd}}$ . Employing equation (3.17), the first Friedmann equation can be expressed as

$$\bar{a}' = \frac{\bar{a}}{\theta_H} \sqrt{r + \frac{f_{\text{mat}}}{\bar{a}^3} + \frac{f_{\text{rad}}}{\bar{a}^4} \frac{g_{\text{eff},\rho}^{\text{SM}}}{g_{\text{eff},\rho}^{\text{SM,cd}}} \left( \frac{g_{\text{eff},s}^{\text{SM,cd}}}{g_{\text{eff},s}^{\text{SM}}} \right)^{4/3} \left( \frac{S_{\text{SM}}}{S_{\text{SM}}^{\text{cd}}} \right)^{4/3}}, \quad (3.19)$$

where the dependence of  $\bar{a}$ ,  $r$ ,  $g_{\text{eff},\rho}^{\text{SM}}$ ,  $g_{\text{eff},s}^{\text{SM}}$  and  $S_{\text{SM}}$  on  $\theta$  has been omitted for brevity. Before we get to relating  $r(\theta)$  with the evolution of  $\rho_{\text{med}}$ , as described in section 3.3, we focus on the last term in (3.19) which describes the amount of entropy that has been injected into the SM bath since  $T_{\text{SM}} = T_{\text{SM}}^{\text{cd}}$ , thus increasing the radiation energy density therein. For coupling a second ODE to the Friedmann equation that quantifies the entropy injection, observe that

$$\frac{d}{d\theta} \left[ \left( \frac{S_{\text{SM}}(\theta)}{S_{\text{SM}}^{\text{cd}}} \right)^{4/3} \right] = \frac{4}{3} \left( \frac{S_{\text{SM}}(\theta)}{S_{\text{SM}}^{\text{cd}}} \right)^{1/3} \frac{S'_{\text{SM}}(\theta)}{S_{\text{SM}}^{\text{cd}}}. \quad (3.20)$$

From the discussion below equation (2.18) we know that the total heat is conserved, such that  $Q'_{\text{tot}} = Q'_{\text{SM}} + Q'_{\text{DS}} = 0$ . Since  $Q'_{\text{DS}} = q'_{\text{DS}} a^3$ , the derivative of  $S_{\text{SM}}$  with respect to the time parameter  $\theta$  thus reads

$$\begin{aligned} S'_{\text{SM}}(\theta) &= \frac{Q'_{\text{SM}}(\theta)}{T_{\text{SM}}(\theta)} = -\frac{Q'_{\text{DS}}(\theta)}{T_{\text{SM}}(\theta)} = -\frac{q'_{\text{DS}}(\theta) a^3(\theta)}{T_{\text{SM}}(\theta)} \\ &= -\left( \frac{2\pi^2}{45} \right)^{1/3} \left( \frac{g_{\text{eff},s}^{\text{SM}}(\theta)}{S_{\text{SM}}(\theta)} \right)^{1/3} q'_{\text{DS}}(\theta) a^4(\theta), \end{aligned} \quad (3.21)$$

*Quantifying the amount of injected entropy*

where equation (3.14) has been used in the last step. Inserting this expression into equation (3.20) and identifying the leftover numerical factors with those in equation (3.16) evaluated at  $\theta = \theta_{\text{cd}}$ , we find

$$\begin{aligned} \frac{d}{d\theta} \left[ \left( \frac{S_{\text{SM}}}{S_{\text{SM}}^{\text{cd}}} \right)^{4/3} \right] &= -\frac{4}{3} \left( \frac{2\pi^2}{45} \right)^{1/3} \left[ \frac{g_{\text{eff},s}^{\text{SM}}}{(S_{\text{SM}}^{\text{cd}})^4} \right]^{1/3} a^4 q'_{\text{DS}} \quad (3.22) \\ &= -\left[ \frac{g_{\text{eff},s}^{\text{SM}}(\theta)}{g_{\text{eff},s}^{\text{SM,cd}}} \right]^{1/3} \frac{g_{\text{eff},\rho}^{\text{SM,cd}}}{g_{\text{eff},\rho}^{\text{SM}}(\theta)} \frac{q'_{\text{DS}}(\theta)}{\rho_{\text{rad}}^{\text{cd}}} \bar{a}^4(\theta). \end{aligned} \quad (3.23)$$

Together with the Friedmann equation (3.19), we have a set of coupled ODEs that describe the evolution of the scale factor and the entropy in the SM bath. The system is, however, still under-determined since the

time evolution of the DOFs is not trivial. To close this gap and simplify the notation, we introduce the functions

$$\gamma(\theta) \equiv \frac{g_{\text{eff},\rho}^{\text{SM}}(\theta)}{g_{\text{eff},s}^{\text{SM}}(\theta)}, \quad \mathcal{G}(\theta) \equiv \frac{g_{\text{eff},s}^{\text{SM}}(\theta)}{g_{\text{eff},s}^{\text{SM},\text{cd}}}, \quad \mathcal{S}(\theta) \equiv \left( \frac{S_{\text{SM}}(\theta)}{S_{\text{SM}}^{\text{cd}}} \right)^{4/3} \quad (3.24)$$

and note that the time evolution of the first two functions is described by

$$\gamma'(\theta) = \frac{d}{dT_{\text{SM}}} \left[ \frac{g_{\text{eff},\rho}^{\text{SM}}(T_{\text{SM}})}{g_{\text{eff},s}^{\text{SM}}(T_{\text{SM}})} \right] \Big|_{T_{\text{SM}}(\theta)} T'_{\text{SM}} = \hat{\gamma}(\theta) T'_{\text{SM}}(\theta), \quad (3.25a)$$

$$\mathcal{G}'(\theta) = \frac{d}{dT_{\text{SM}}} \left[ \frac{g_{\text{eff},s}^{\text{SM}}(T_{\text{SM}})}{g_{\text{eff},s}^{\text{SM},\text{cd}}} \right] \Big|_{T_{\text{SM}}(\theta)} T'_{\text{SM}} = \hat{\mathcal{G}}(\theta) T'_{\text{SM}}(\theta). \quad (3.25b)$$

Note that  $\hat{\gamma}$  and  $\hat{\mathcal{G}}$  can both be calculated from the known temperature evolution of the effective SM DOFs and the equation (3.14) for a given time  $\theta$ . In order to use these expressions to close the system of coupled ODEs, we further need to describe  $T'_{\text{SM}}$ . Dividing equation (3.14) by itself evaluated at  $\theta = \theta_{\text{cd}}$  leaves us with

$$\frac{T_{\text{SM}}(\theta)}{T_{\text{SM}}^{\text{cd}}} = \frac{a}{a_{\text{cd}}} \left( \frac{S_{\text{SM}}}{S_{\text{SM}}^{\text{cd}}} \right)^{1/3} \left( \frac{g_{\text{eff},s}^{\text{SM},\text{cd}}}{g_{\text{eff},s}^{\text{SM}}} \right)^{1/3} = \bar{a} \mathcal{S}^{1/4} \quad (3.26)$$

$$\Rightarrow \frac{d}{d\theta} \frac{T_{\text{SM}}(\theta)}{T_{\text{SM}}^{\text{cd}}} = \frac{3 \mathcal{G} \bar{a} \mathcal{S}' - 12 \mathcal{G} \bar{a}' \mathcal{S} - 4 \mathcal{G}' \bar{a} \mathcal{S}}{12 \mathcal{G}^{4/3} \mathcal{S}^{3/4} \bar{a}^2}. \quad (3.27)$$

Note that this expression itself depends on  $\mathcal{G}'$ . Inserting the expression we just obtained into equation (3.25b) and solving for  $\mathcal{G}'$  yields

$$\mathcal{G}'(\theta) = -\frac{3}{4} \frac{T_{\text{SM}}^{\text{cd}} \mathcal{G} \hat{\mathcal{G}}}{\mathcal{S}^{3/4} \bar{a}} \frac{4 \mathcal{S} \bar{a}' - \mathcal{S}' \bar{a}}{T_{\text{SM}}^{\text{cd}} \hat{\mathcal{G}} \mathcal{S}^{1/4} + 3 \mathcal{G}^{4/3} \bar{a}}. \quad (3.28)$$

Since  $\mathcal{G}'$  is now determined, we can also use equation (3.25a) to describe the time evolution of  $\gamma(\theta)$ :

$$\gamma'(\theta) = \hat{\gamma} T_{\text{SM}}^{\text{cd}} \frac{3 \mathcal{G} \bar{a} \mathcal{S}' - 12 \mathcal{G} \bar{a}' \mathcal{S} - 4 \mathcal{G}' \bar{a} \mathcal{S}}{12 \mathcal{G}^{4/3} \mathcal{S}^{3/4} \bar{a}^2}. \quad (3.29)$$

The last piece to receive a completely determined set of ODEs can be obtained by including a specific time evolution of the mediator species, as it has been discussed in section 3.3. Consider that the volume heat rate of our dark sector is given by

$$q'_{\text{DS}}(\theta) = \rho'_{\text{med}}(\theta) + 3 \frac{\bar{a}'(\theta)}{\bar{a}(\theta)} \zeta(\theta) \rho_{\text{med}}(\theta) = -\rho_{\text{med}}(\theta). \quad (3.30)$$

*The evolution of the SM temperature and DOFs.*

*Including the evolution of the mediator*

The factor  $q'_{\text{DS}}/\rho_{\text{rad}}^{\text{cd}}$  in equation (3.23) describing the entropy injection can therefore be simplified to

$$\frac{q'_{\text{DS}}(\theta)}{\rho_{\text{rad}}^{\text{cd}}} = -\frac{\rho_{\text{med}}(\theta)}{\rho_{\text{rad}}^{\text{cd}}} = -\frac{\rho_{\text{med}}^{\text{cd}}}{\rho_{\text{rad}}^{\text{cd}}} r(\theta) = -\frac{r(\theta)}{f_{\text{rad}}}, \quad (3.31)$$

where

$$r'(\theta) = -r(\theta) - 3 \frac{\bar{a}'(\theta)}{\bar{a}(\theta)} \zeta(\theta) r(\theta). \quad (3.32)$$

The time evolution of the scale factor, the SM entropy, the mediator energy density and the effective DOFs in the SM bath can therefore be described by the following set of coupled ODEs:

$$\begin{aligned} \bar{a}' &= \frac{\bar{a}}{\theta_{\text{H}}} \sqrt{r + \frac{f_{\text{mat}}}{\bar{a}^3} + \frac{f_{\text{rad}}}{\bar{a}^4} \frac{\gamma}{\gamma_{\text{cd}}} \frac{\mathcal{S}}{\mathcal{G}^{1/3}}}, \\ \mathcal{S}' &= \frac{r \bar{a}^4}{f_{\text{rad}}} \mathcal{G}^{1/3} \gamma_{\text{cd}}, \\ r' &= -r - 3 \frac{\bar{a}'}{\bar{a}} \zeta r, \\ \mathcal{G}' &= -\frac{3}{4} \frac{T_{\text{SM}}^{\text{cd}} \mathcal{G} \hat{\mathcal{G}}}{\mathcal{S}^{3/4} \bar{a}} \frac{4 \mathcal{S} \bar{a}' - \mathcal{S}' \bar{a}}{T_{\text{SM}}^{\text{cd}} \hat{\mathcal{G}} \mathcal{S}^{1/4} + 3 \mathcal{G}^{4/3} \bar{a}}, \\ \gamma' &= \hat{\gamma} T_{\text{SM}}^{\text{cd}} \frac{3 \mathcal{G} \bar{a} \mathcal{S}' - 12 \mathcal{G} \bar{a}' \mathcal{S} - 4 \mathcal{G}' \bar{a} \mathcal{S}}{12 \mathcal{G}^{4/3} \mathcal{S}^{3/4} \bar{a}^2}. \end{aligned} \quad (3.33)$$

The corresponding initial values are fixed by  $\bar{a}_{\text{cd}} = \mathcal{S}_{\text{cd}} = r_{\text{cd}} = \mathcal{G}_{\text{cd}} = 1$  and  $\gamma_{\text{cd}}$ , which will be close to 1 as can be seen in Figure 3.1. A full interpretation of this set of equations will become possible as soon as we will consider its solutions. However, a first interpretation of them is already possible now: The first line connects the evolution of the normalized scale factor with the matter content of the Universe. The characteristic time scale of its change is fixed by  $\theta_{\text{H}}$ , whereas the actual dynamics comes from the normalized mediator energy density  $r$ . If  $r$  remains small, there will be only a minor entropy injection, such that  $\mathcal{S}$  will remain close to 1. The immediate interpretation of the latter two equations, connected to the evolution of  $g_{\text{eff},s}^{\text{SM}}(\theta)$  and  $g_{\text{eff},\rho}^{\text{SM}}(\theta)$ , is more involved, but since they will be of negligible importance in most cases, we do not discuss them further at this point. Only in extreme scenarios that include the description of temperatures close to or below the QCD phase transition where the relativistic DOFs in the SM bath decrease considerably (see Figure 3.1), there can be a visible effect on the overall time evolution of the energy densities considered. In the model we will be describing in chapter 4,  $\gamma$  and  $\mathcal{G}$  will always remain close to 1.

*Interpreting the full set of coupled ODEs for the DS evolution, decay and the entropy injection*

*Choosing a set of physical input parameters*

Hence, the only relevant quantities that specify the evolution of our DS are the constants  $f_{\text{mat}}$ ,  $f_{\text{rad}}$ , the temperature of the SM bath  $T_{\text{SM}}^{\text{cd}}$  when the mediator decouples from other particle species, the time

scale  $\theta_H$  (fixed by  $\rho_{\text{med}}^{\text{cd}}$  and the mediator decay width  $\Gamma$ ), as well as  $\tilde{\theta}$  and  $\alpha_{32}$ , fixing the function  $\zeta(\theta)$  defined in equation (3.11). This choice of parameters was natural in deriving the set of equations (3.33), but is not very handy when trying to interpret the effect of changing the mediator mass, for instance. We therefore re-express these input quantities for the numerical evaluation of the ODEs in terms of  $T_{\text{SM}}^{\text{cd}}$ ,  $\Gamma$ ,  $\alpha_{32}$ , as well as the mediator mass  $m_{\text{med}}$ , the temperature ratio  $\tilde{\zeta}_{\text{cd}} \equiv \zeta(T_{\text{SM}}^{\text{cd}})$  between the two sectors at the chemical decoupling, the intrinsic mediator degrees of freedom  $g_{\text{med}}$ , and the normalized matter energy density  $f_{\text{mat}}$  at chemical decoupling. The latter will be set to zero in the following analysis, since any matter density will be much smaller than the mediator energy density at the considered early period of the Universe. Moreover, focusing on the case with  $g_{\text{med}} = 1$ , we are left with five physical parameters describing the evolution of the mediator species as well as the scale factor and the SM entropy ratio generated during the decay.

From these five parameters, the initial mediator energy density  $\rho_{\text{med}}^{\text{cd}}$  can be obtained by integrating equation (2.16a) by assuming an LTE<sup>5</sup> at chemical decoupling and setting  $T_{\text{DS}}^{\text{cd}} = \tilde{\zeta}_{\text{cd}} T_{\text{SM}}^{\text{cd}}$ . The initial SM radiation energy density can be calculated by using equation (3.16), after having determined  $g_{\text{eff},\rho}^{\text{SM,cd}}$ , which can be done using  $T_{\text{SM}}^{\text{cd}}$  and an interpolation of the tabulated DOFs of the SM bath. Using the same technique, the temperature derivatives in  $\hat{\gamma}$  and  $\hat{\mathcal{G}}$  can be obtained as well. Knowing the different sources of energy density<sup>6</sup>, the age of the Universe at chemical decoupling  $t_{\text{cd}}$  can be computed by integrating the first Friedmann equation (2.4a) [59]. Then, both the time parameters, that were defined as  $\tilde{\theta} \equiv 7 \theta_{\text{cd}} (T_{\text{DS}}^{\text{cd}}/m_{\text{med}})^2$  and  $\theta_H \equiv \sqrt{3 m_{\text{Pl}}^2 \Gamma^2 / \rho_{\text{med}}^{\text{cd}}}$ , and the normalized initial energy density  $f_{\text{rad}} \equiv \rho_{\text{rad}}^{\text{cd}} / \rho_{\text{med}}^{\text{cd}}$  can be determined.

Five input  
parameters:  $T_{\text{SM}}^{\text{cd}}$ ,  
 $m_{\text{med}}$ ,  $\tilde{\zeta}_{\text{cd}}$ ,  $\Gamma$ ,  $\alpha_{32}$

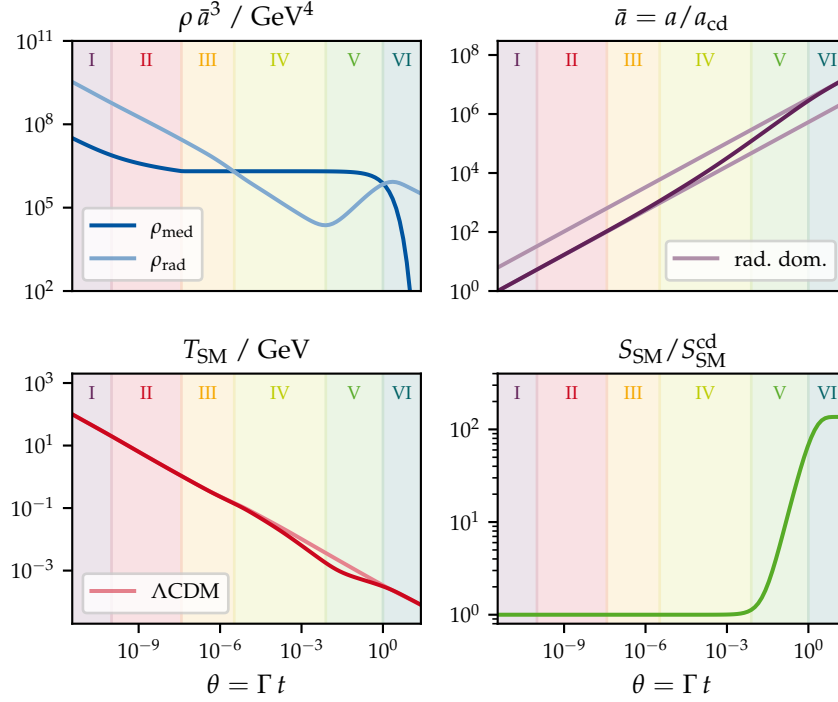
### 3.4.2 Numerical solution of the equations governing the entropy injection

Figure 3.4 shows an overview of the evolution of the energy densities  $\rho_{\text{med}}$  and  $\rho_{\text{rad}}$ , the normalized scale factor  $\bar{a}$ , the temperature of the SM bath  $T_{\text{SM}}$ , and the amount of injected entropy  $S_{\text{SM}}/S_{\text{SM}}^{\text{cd}}$  into the SM bath as functions of the dimensionless time parameter  $\theta = \Gamma t$ . The five physical input parameters used for solving the system of coupled ODEs numerically are  $T_{\text{SM}}^{\text{cd}} = 100 \text{ GeV}$ ,  $m_{\text{med}} = 50 \text{ GeV}$ ,  $\Gamma = 10^{-25} \text{ GeV}$

An overview of the  
six phases shown in  
Figure 3.4

<sup>5</sup> This assumption is well-founded, since the mediator initially retains a thermal distribution in the process of chemical decoupling as was discussed in reference [24].

<sup>6</sup> There exists some ambiguity in counting the mediator energy density as matter or radiation during this integration when  $m_{\text{med}}/T_{\text{DS}}^{\text{cd}} = \mathcal{O}(1)$ . We chose to count the mediator species as radiation if  $m_{\text{med}}/T_{\text{DS}}^{\text{cd}} < 1$ .



**Figure 3.4:** Starting from the top left (clockwise): Time evolution of the comoving energy densities  $\rho \bar{a}^3$  of the mediator species and the SM radiation, the normalized scale factor  $\bar{a}$ , the entropy  $S_{\text{SM}}/S_{\text{SM}}^{\text{cd}}$  of the SM bath, as well as its temperature  $T_{\text{SM}}$ . The evolution can be obtained by numerically solving the set of ODEs defined in equation (3.33) and can be ordered into the different phases, which are referred to with roman numerals in the plot: Relativistic mediator (I), cannibalism (II), non-relativistic mediator (III), early matter domination (IV), entropy injection (V), and decay (VI). A detailed description of the individual phases and the physical parameters used to generate these plots is given in the text.

(corresponding to a mediator lifetime of about 7 s),  $\zeta_{\text{cd}} = 1$ , and  $\alpha_{32} = 2 \cdot 10^{-3}$  (corresponding to the quartic coupling  $\lambda \simeq 10^{-3}$  within the Lagrangian density defined in equation (2.35)). To obtain all the possible details from this specific case, let us go through the individual phases marked with roman numerals and background areas shaded in diverse colors.

#### Phase I

We start to integrate the equations (3.33) from the point in time on where  $T_{\text{SM}} = 100 \text{ GeV}$ , so when top and anti-top quarks already annihilated and the EWPT just happened. At that point, the Universe is dominated by the SM radiation, which is why the scale factor has the proportionality  $a \propto \sqrt{t}$  as expected by the  $\Lambda\text{CDM}$  model. Moreover, the temperature drops due to the expansion of the Universe with  $T_{\text{SM}} \propto 1/a$ . Since  $\zeta_{\text{cd}} = 1$ , the temperature of the DS coincides with

the temperature of the SM bath, when the heavier DS particle species decouple from the mediator, i. e.  $T_{\text{DS}}^{\text{cd}} = T_{\text{SM}}^{\text{cd}}$ . Because the mass of the mediator is only a factor of 2 larger than  $T_{\text{DS}}^{\text{cd}}$ , it is almost non-relativistic at chemical decoupling, such that the mediator quickly enters in the phase II.

This phase shows a smooth transition from the relativistic  $\rho_{\text{med}} \propto \bar{a}^{-4}$  behavior to the non-relativistic  $\rho_{\text{med}} \propto \bar{a}^{-3}$  behavior, as dictated by the conservation of entropy, when number-changing processes can occur in the DS. We have checked for a few examples that this phase indeed shows the expected scale factor dependence of a cannibalistic era by fitting the law  $\rho_{\text{med}} \bar{a}^3 \propto 1/\ln \bar{a}$  to the curve. Without this phase of cannibalism, the mediator energy density would be considerably larger and phase III would have started immediately after phase I.

*Phase II*

At some point, the mediator does not undergo further number-changing processes, which means that its cannibalistic era ends. From now on, its energy density follows the expected decay law of a non-relativistic species  $\rho_{\text{med}} a^3 \propto \exp(-\theta)$ . Since the energy density of the SM radiation however still scales with  $\rho_{\text{rad}} \propto a^{-4}$ , the mediator will inevitably dominate the energy density of the Universe, which also marks the end of phase III and the onset of phase IV.

*Phase III*

Now, a few processes happen simultaneously: First, since the mediator density scales as  $a^{-3}$  and dominates the Universe's energy content, we find ourselves in a phase of early matter domination. This means that the scale factor no longer scales as  $a \propto t^{1/2}$ , but rather with  $a \propto t^{2/3}$ . Therefore, we can see that  $\bar{a}$  starts to deviate from its initial time evolution as marked in light violet in the upper right plot. Consequently, since the scale factor increases faster, there is a (slightly visible) change in the rate with which  $\rho_{\text{rad}} \bar{a}^3$  decreases. For the same reason, the temperature of the SM bath falls off slightly more quickly ( $T_{\text{SM}} \propto t^{-2/3}$ ) than predicted in the  $\Lambda$ CDM model ( $T_{\text{SM}} \propto t^{-1/2}$ ). This change in the decrease stems from the fact that the Universe expands more quickly (as described by  $\bar{a}$ ) rather than the other factors  $\mathcal{S}^{1/4}$  and  $\mathcal{G}^{1/3}$  in equation (3.26). This changes when we transition from phase IV to phase V.

*Phase IV*

In phase V, the mediator decay and the injection of entropy into the SM bath become relevant. Therefore, we can see a change in the curve  $S_{\text{SM}}/S_{\text{SM}}^{\text{cd}}$  for the first time when  $\theta \simeq 10^{-2}$ . Now, the energy density of the mediator slowly starts to decrease as a result of its decay, reheating the SM bath due to the factor  $\mathcal{S}^{1/4}$  in equation (3.26). Note, however, that there is no literal "reheating" but rather a decrease of the SM temperature that is less than  $T_{\text{SM}} \propto a^{-1}$ . As shown in reference [13], the scaling in this period reads  $T_{\text{SM}} \propto a^{-3/8}$ . With the decrease of mediator energy density, the radiation energy density increases, until

*Phase V*

it dominates over the leftover mediator again. Therefore, the initial radiation domination is restored.

*Phase VI*

The final phase VI describes the ongoing decay of the mediator after the end of the early matter domination. At  $\theta \sim 1$ , the two energy densities considered here are again equal and the temperature has almost reached its  $\Lambda$ CDM evolution, as described by the curve in light red. This curve was calculated using equation (3.26), but therein setting  $a \propto \sqrt{t}$  (as in radiation domination) and  $\mathcal{S} = 1$  (for no entropy injection). Now, the temperature of the SM bath lies below the MeV scale such that the  $g_{\text{eff},s}^{\text{SM}}$  in total decreased by one order of magnitude. Since  $T_{\text{SM}}$  nevertheless scales only with  $\mathcal{G}^{-1/3}$ , the effect of the annihilation of SM particles species and particularly the QCD phase transition could not be observed visually. Only a closer look at the curves for  $T_{\text{SM}}$  and  $\rho_{\text{rad}}$  would allow us to tell, that due to the decrease of  $g_{\text{eff},s}^{\text{SM}}$ , the SM bath reheats slightly for every annihilating particle species therein. Since, in either case, the decaying mediator cannot inject more entropy into the SM bath, at some point the curve for  $S_{\text{SM}}/S_{\text{SM}}^{\text{cd}}$  saturates and the radiation energy density decreases because of the expansion of the Universe in radiation domination, as it was the case initially.

### 3.4.3 The dilution of dark matter and gravitational waves

The out-of-equilibrium decay of the mediator can result in a considerable injection of entropy and energy into the SM bath, as we have observed in Figure 3.4, where the comoving entropy of the SM bath is more than 100 times higher after the DS decay than before. While the thermal evolution as described in the  $\Lambda$ CDM model will take over after that, there is nevertheless one main consequence of the entropy injection, i. e. the dilution of frozen-out abundances. As the comoving entropy density  $s_{\text{SM}} a^3$  is not conserved during the decay, also a comoving DM yield  $Y \equiv n_{\text{DM}}/s_{\text{SM}}$  will not be conserved. In fact, the yield of a DM freeze-out calculation would be diluted by the factor  $S_{\text{SM}}^{\text{FO}}/S_{\text{SM}}^0$  [13], where the index 0 denotes today and FO denotes the point in time when the freeze-out happened.

*The injected entropy is diluting DM and the SGWB*

We will transfer this dilution to the generated SGWB, which can be interpreted as a form of dark radiation. In that case, the relevant quantity to quantify the dilution is the scale factor ratio between its nucleation and today. Using equation (3.14), we obtain

$$\frac{a_n}{a_0} = \left( \frac{S_{\text{SM}}^n}{S_{\text{SM}}^0} \right)^{1/3} \left( \frac{g_{\text{eff},s}^{\text{SM},0}}{g_{\text{eff},s}^{\text{SM},n}} \right)^{1/3} \frac{T_{\text{SM}}^0}{T_{\text{SM}}^n}, \quad (3.34)$$

*Introducing the dilution factor  $D_{\text{SM}}$*

where the indices “0” and “n” denote today and the respective quantity at the nucleation of bubbles in the FOPT. Assuming that the comoving

SM entropy is separately conserved before and after the mediator decay, we can identify the first factor as  $D_{\text{SM}}^{-1/3}$  with

$$D_{\text{SM}} \equiv \frac{S_{\text{SM}}(\theta \gg 1)}{S_{\text{SM}}^{\text{cd}}}. \quad (3.35)$$

Apart from a mere redshift due to the decrease in  $T_{\text{SM}}$  since the generation of the SGWB and an  $\mathcal{O}(1)$  factor due to the decrease in DOFs, we thereby see that the scale factor ratio also decreases due to  $D_{\text{SM}} \geq 1$ . The frequency spectrum of an SGWB generated before the decay of the mediator will therefore be lower than expected without the dilution effect. Vice versa, if we observe an SGWB with a given frequency spectrum, its spectrum at generation must have been shifted towards higher frequencies than one would expect without an additional dilution in between:

$$\frac{a_0}{a_n} f = D_{\text{SM}}^{1/3} \left( \frac{g_{\text{eff},s}^{\text{SM},n}}{g_{\text{eff},s}^{\text{SM},0}} \right)^{1/3} \frac{T_{\text{SM}}^n}{T_{\text{SM}}^0} f. \quad (3.36)$$

This expression will be used to calculate the red-shifted frequency in equation (2.95). The redshift of the signal's amplitude also undergoes a redshift, which we denoted by  $\mathcal{R}$  in equation (2.96). Since the Hubble parameter is fixed by  $H^2(T) = \frac{\pi^2}{90} g_{\text{eff},\rho}^{\text{tot}}(T) \frac{T^4}{m_{\text{Pl}}^2}$ , we obtain

$$\begin{aligned} \mathcal{R} &= \frac{1}{D_{\text{SM}}^{4/3}} \left( \frac{g_{\text{eff},s}^{\text{SM},0}}{g_{\text{eff},s}^{\text{SM},n}} \right)^{4/3} \left( \frac{T_{\text{SM}}^0}{T_{\text{SM}}^{\text{nuc}}} \right)^4 \left( \frac{H_n}{H_0} \right)^2 \\ &= \frac{1}{D_{\text{SM}}^{4/3}} \left( \frac{g_{\text{eff},s}^{\text{SM},0}}{g_{\text{eff},s}^{\text{SM},n}} \right)^{4/3} \frac{\pi^2 g_{\text{eff},\rho}^{\text{tot},n} (T_{\text{SM}}^0)^4}{90 m_{\text{Pl}}^2 H_0^2}. \end{aligned} \quad (3.37)$$

Since we wish to condense the effect of the temperature ratio  $\xi$  into one quantity, we further introduce

*Introducing the dilution factor  $D$*

$$D \equiv \frac{g_{\text{eff},s}^{\text{SM},n}}{g_{\text{eff},s}^{\text{tot},n}} D_{\text{SM}}, \quad (3.38)$$

which saturates when increasing  $\xi_{\text{cd}}$ , as shown in reference [13]. Using this quantity and setting  $T_{\text{SM}}^0 = 2.35 \cdot 10^{-13} \text{ GeV}$ , the redshift of the SGWB amplitude can be expressed as

$$\mathcal{R} h^2 \simeq \frac{2.473 \cdot 10^{-5}}{D^{4/3}} \left( \frac{g_{\text{eff},s}^{\text{SM},0}}{g_{\text{eff},s}^{\text{tot},n}} \right)^{4/3} \frac{g_{\text{eff},\rho}^{\text{tot},n}}{2}, \quad (3.39)$$

which corresponds to the expression given in reference [26], but with an additional factor of  $D^{-4/3}$ , allowing also for a dilution of the signal. Note that the dependences of  $\left( \frac{g_{\text{eff},s}^{\text{tot},n}}{g_{\text{eff},s}^{\text{SM},0}} \right)^{-4/3}$  and  $g_{\text{eff},\rho}^{\text{tot},n}$  on  $\xi_n$  now cancel in the limit of high temperature ratios. The effect of the temperature

ratio between the DS and the SM bath during the generation of the SGWB is therefore (almost) isolated in  $D$ .

We can now describe the effect of the mediator decay on the SGWB by investigating the dependence of the dilution factor  $D_{\text{SM}}$  (or analogously,  $D$ ) on the input parameters defined at the end of subsection 3.4.1. To get a feeling for the impact of these different quantities that specify the DS and its decay, a scan over different planes in the resulting parameter space is shown in Figure 3.5. The left column of plots shows the dependence of  $D_{\text{SM}}$  on the temperature of the SM bath at decoupling  $T_{\text{SM}}^{\text{cd}}$ , the mediator mass  $m_{\text{med}}$ , the temperature ratio at chemical decoupling  $\xi_{\text{cd}}$ , the effective  $3 \rightarrow 2$  coupling  $\alpha_{32}$  and the mediator decay width  $\Gamma$ , whereas the right column specifies the temperature  $T_{\text{SM}}^{\text{fin}} \equiv T_{\text{SM}}(\theta = 5)$ , at which the mediator has decayed. The mediator decay width ranges from  $10^{-30}$  GeV to  $10^{-15}$  GeV in the shared horizontal axis among all plots, corresponding to mediator lifetimes between about one week and a few nanoseconds. This broad range of decay widths is of course constrained and should rather be interpreted as an overview of the possible solutions of the equations (3.33), than as an attempt to build a feasible model for a DS.

*Dependence of  $D_{\text{SM}}$  and  $T_{\text{SM}}^{\text{fin}}$  on the five independent DS parameters*

The most striking feature is the independence of the SM temperature after the decay on all the parameters except for  $\Gamma$ . This reflects the result that we already saw in Figure 3.4, when  $T_{\text{SM}}$  approached the prediction of the  $\Lambda$ CDM curve. Given that the decay of the dark sector should be finished before the QCD phase transition, we have to focus on mediator lifetimes below  $\mathcal{O}(1 \text{ s})$ . The only influence of the four parameters next to  $\Gamma$  that determine  $T_{\text{SM}}^{\text{fin}}$  is thus on the limits, in which our underlying assumptions are fulfilled. Explicitly, only the regions for which  $\theta_{\text{cd}} < 1$  are shown in the plots, since for  $\theta_{\text{cd}} \geq 1$  (white background area) the lifetime of the mediator is so short that it is already decaying at chemical decoupling.

*The SM temperature after the decay is fixed by  $\Gamma$*

The scan over the initial temperature (in the first row) shows that the dilution factor  $D_{\text{SM}}$  remains close to 1 in large parts of the parameter space. There can only be a sizable entropy injection, when the mediator lifetime is large enough. Moreover, this can only be the case when the mediator is not already Boltzmann suppressed<sup>7</sup> at chemical decoupling. In this plot, the mediator mass was set to  $m_{\text{med}} = 1 \text{ GeV}$  and  $\xi_{\text{cd}} = 1$ , such that the Boltzmann suppression occurs for temperatures  $T_{\text{SM}}^{\text{cd}} \lesssim 1 \text{ GeV}$ . For temperatures  $T_{\text{SM}}^{\text{cd}} \gtrsim 1 \text{ GeV}$ , the dilution factor almost saturates since the physical situation at the mediator decay does not change. The slight decrease in  $D_{\text{SM}}$  when going to higher

*Boltzmann suppression for  $T_{\text{DS}}^{\text{cd}} \lesssim m_{\text{med}}$*

<sup>7</sup> Note that a Boltzmann suppression of the mediator at chemical decoupling is not possible in our physical scenario: If the mediator would be Boltzmann suppressed at chemical decoupling, it could not be the mediator, as it would not be the single lightest DS particle species, which is in conflict with the assumptions that we made at the beginning of this chapter.

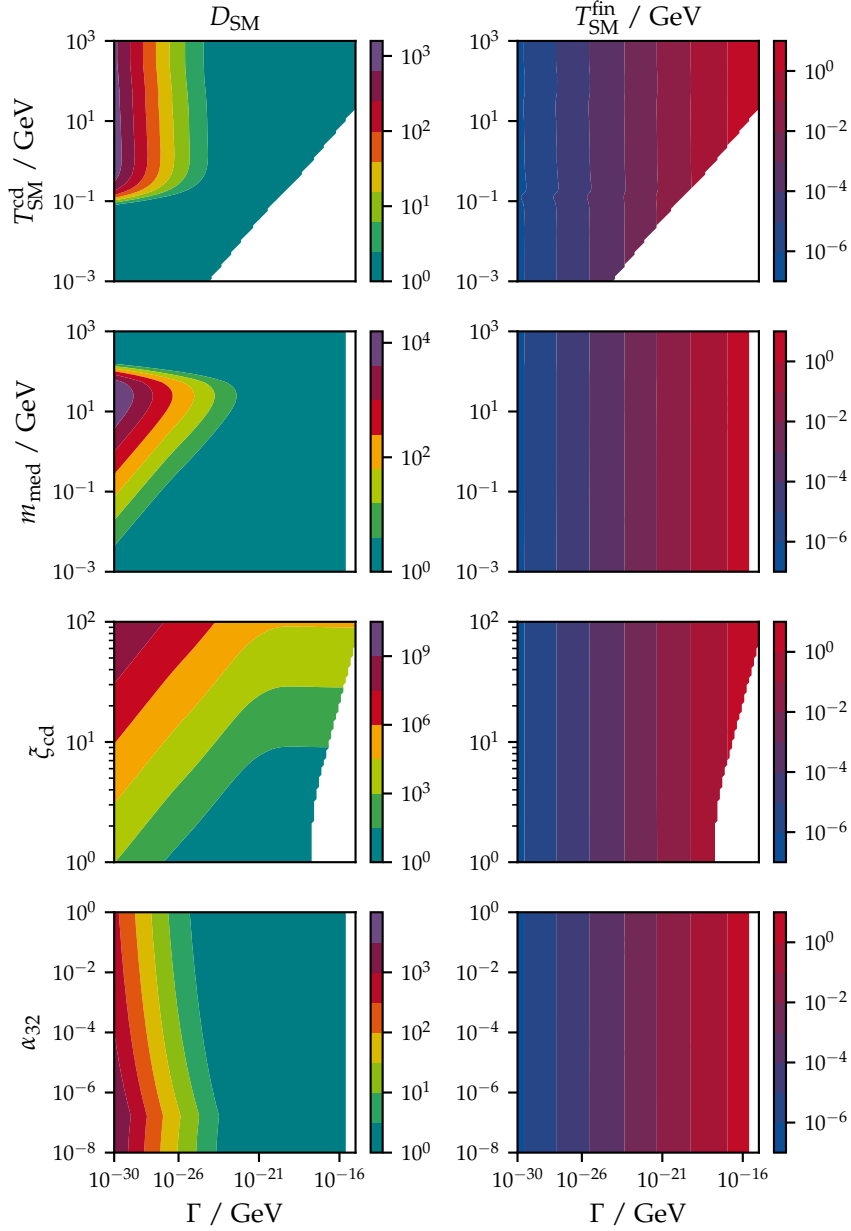


**Figure 3.5:** Scan over the five DS parameters which determine the dilution factor  $D_{\text{SM}}$  and the final temperatures  $T_{\text{SM}}^{\text{fin}} \equiv T_{\text{SM}}(\theta = 5)$ , when the decay of the mediator has happened. In the first row,  $m_{\text{med}} = 1 \text{ GeV}$ ,  $\xi_{\text{cd}} = 1$ , and  $\alpha_{32} = 10^{-4}$  are fixed. In the second row, the same parameters as in the first row are used, except that  $T_{\text{SM}}^{\text{cd}} = 10 \text{ GeV}$  is held constant. In the third row,  $m_{\text{med}} = T_{\text{SM}}^{\text{cd}} = 1 \text{ GeV}$  and  $\alpha_{32} = 10^{-4}$  are chosen to be constant, whereas in the fourth row  $\xi_{\text{cd}} = 1$ ,  $m_{\text{med}} = 1 \text{ GeV}$  and  $T_{\text{SM}}^{\text{cd}} = 10 \text{ GeV}$ . In the white areas of the plots,  $\theta_{\text{cd}} > 1$ , indicating the immediate decay of the mediator at chemical decoupling. A detailed description of the different effects explaining the shown dependences can be found in the text.

$T_{\text{SM}}^{\text{cd}}$  can be explained by the initially greater number of effective DOFs in the SM radiation, decreasing the ratio between the initial mediator and radiation energy density.

*Smaller  $m_{\text{med}}$  lead to weaker early matter dominations*

The effect of the Boltzmann suppression can also be seen in the scan over the mediator mass (in the second row). Here, for masses above 10 GeV the dilution factor decreases quickly due to the Boltzmann suppression of the initial mediator energy density, since  $T_{\text{SM}}^{\text{cd}} = 10$  GeV and  $\zeta_{\text{cd}} = 1$ . Below this mass, the dilution factor decreases as well, this time however due to a weakened effect of the early matter domination: For a smaller mass, the mediator has a longer period of relativistic and cannibalistic evolution, such that the duration of the early matter domination and thus also the deviation from the scale factor evolution in radiation domination becomes smaller, eventually resulting in a decreased dilution factor.

*A hotter DS injects more entropy*

The plot in the third row shows the effect of varying the DS temperature with respect to the SM temperature at chemical decoupling. Since an increase in  $\zeta_{\text{cd}}$  also results in an increase in the energy and entropy stored in the DS, the later on injected entropy scales accordingly. Therefore  $D_{\text{SM}}$  increases when  $\zeta_{\text{cd}}$  is larger. Interestingly, there exists a threshold mediator decay width above which  $D_{\text{SM}}$  depends no more on  $\Gamma$ . This, however, is a relic of our assumption that the mediator decays while being non-relativistic. In fact, in the regions in which the dependence on  $\Gamma$  drops, we identified that  $\tilde{\theta} > 1$ , indicating that the mediator becomes non-relativistic only after  $\theta = 1$ , which is in contrast to the used assumptions of non-relativistic decays. Furthermore, in this case, inverse decays from SM particles to the DS will become important, which could moreover tamper with our most fundamental assumption that the coupling is sufficiently small to guarantee separate thermal baths. For these two reasons, we cannot trust our predictions for non-relativistic decays in this region of parameter space. Therefore, we will have to separately assure in our following analysis of chapter 4 that the mediator species decays as a cold relic.

*With cannibalism, the early matter domination is shorter and less severe*

The general effect of the cannibalistic era can be observed in the left plot in the fourth row, describing the dependence of  $D_{\text{SM}}$  on  $\alpha_{32}$ . A large effective  $3 \rightarrow 2$  coupling means that the number-changing processes become inefficient later than for small  $\alpha_{32}$ . Since during a cannibalistic era the comoving mediator energy density  $\rho_{\text{med}} a^3$  decreases, the Universe will thus enter into a possible phase of early matter domination only relatively late, if  $\alpha_{32}$  is large. The saturation of  $D_{\text{SM}}$  towards low  $\alpha_{32}$  is caused by the immediate switch from  $\zeta(\theta) = 4/3$  to  $\zeta(\theta) = 1$ , when no number-changing processes can take place when  $\theta = \tilde{\theta}$ , as  $\Gamma_{32} < H$  already is fulfilled by the smallness of  $\alpha_{32}$ .

### 3.5 PARAMETERIZING SGWBs FROM HOT DARK SECTORS

The description of the dynamics of the entropy injection is now finished. We have seen that the out-of-equilibrium decay of the mediator species can lead to a sizable entropy injection, leading to the dilution of SGWBs. Since the DS in our investigated model will itself generate the SGWB through an FOPT of the dark Higgs, we can connect the already introduced quantities shown in Figure 3.5, especially the temperature ratio, to the quantities determining the GW spectrum.

*What is the influence of  $\zeta$  on the SGWB?*

Including the DOFs going into the calculation of the redshift  $\mathcal{R}h^2$  and  $a_n/a_0$ , we find that ten parameters are necessary to calculate the spectrum of the SGWB produced in an FOPT: The transition strength  $\alpha$ , the critical transition strength  $\alpha_\infty$  for runaway bubbles, the inverse time scale  $\beta/H$ , the dilution factor  $D$ , the nucleation temperature  $T_{SM}^n$ , the DOFs  $g_{\text{eff},\rho}^{\text{tot},n}$ ,  $g_{\text{eff},s}^{\text{tot},n}$ , and  $g_{\text{eff},s}^{\text{SM},0}$ , the percentage of bulk motion energy going into turbulence  $\epsilon_{\text{turb}}$ , as well as the bubble wall velocity  $v_w$ . As discussed in chapter 2.5.4, we will optimistically set  $\epsilon_{\text{turb}} = 10\%$  and  $v_w = 1$  in accordance with the work by Breitbach et al. [12]. Since our investigated model further does not include additional DOFs to the SM that are still abundant today, we can set  $g_{\text{eff},s}^{\text{SM},0} = 3.93$  [54]. Further, a detailed description of the calculation of the DOFs  $g_{\text{eff},\rho}^{\text{tot},n}$  and  $g_{\text{eff},s}^{\text{tot},n}$ , and the dilution factor  $D$  has already been presented in the sections 3.2 and 3.4.

*Out of the 10 SGWB parameters,  $\alpha$ ,  $\beta/H$ ,  $T_{SM}^n$ , and  $D$  are most important*

Due to the previous discussion of DSs we are now well-equipped to extend the superficial description of the parameters  $\alpha$ ,  $\alpha_\infty$ ,  $\beta/H$ , and  $T_{SM}^n$  given in chapter 2.5.4. First of all, it should be noted that the nucleation condition presented in equation (2.63) remained agnostic about the precise notion of the temperature  $T_n$ . We will follow the approach described in reference [12] and use the DS temperatures in the nucleation criterion, neglecting logarithmic corrections arising from the difference between  $T_{DS}^n$  and  $T_{SM}^n$ . Once the nucleation temperature  $T_{DS}^n$  is determined, we will convert it to an SM temperature by dividing it by  $\zeta_n$ . To further spare the calculation of the time evolution of  $\zeta(T_{SM})$  from some fixed point before the phase transition until  $T_{SM} = T_{SM}^n$ , we will immediately use  $\zeta_n$  as an input parameter when scanning over different realizations of the model presented in chapter 4.

*$\zeta_n$  translates  $T_{SM}^n$  and  $T_{DS}^n$*

Having fixed the nucleation temperature of the DS phase transition, we can determine the inverse timescale  $\beta/H$  following equation (2.92), where we again set  $T_n = T_{DS}^n$ . Note that  $\beta/H$  is independent of the temperature ratio  $\zeta_n$ , such that one could use  $T_{SM}^n$  as well to come to the same inverse timescale, since  $\zeta_n$  cancels [12].

*$\beta/H$  does not depend on  $\zeta_n$*

Since the radiation energy density at the nucleation is given by  $\rho_{\text{rad}}^n = \frac{\pi^2}{30} g_{\text{eff},\rho}^{\text{tot},n} (T_{\text{SM}}^n)^4$  and  $g_{\text{eff},\rho}^{\text{tot},n} = g_{\text{eff},\rho}^{\text{SM},n} + g_{\text{eff},\rho}^{\text{DS},n} \zeta_n^4$ , there will be a considerable influence of  $\zeta_n$  on the transition strength  $\alpha = \epsilon / \rho_{\text{rad}}^n$ . The latent heat  $\epsilon$  can be computed using equation (2.90) and is independent of the temperature ratio between the two sectors. By replacing  $T_{\text{SM}}^n$  with  $\zeta_n^{-1} T_{\text{DS}}^n$ , we find that

$$\rho_{\text{rad}}^n = \frac{\pi^2}{30} \left( \frac{g_{\text{eff},\rho}^{\text{SM},n}}{\zeta_n^4} + g_{\text{eff},\rho}^{\text{DS},n} \right) (T_{\text{DS}}^n)^4, \quad (3.40)$$

$\alpha \propto \zeta_n^4$  for small  $\zeta_n$   
and few DOFs in the  
DS

from which we follow that for small  $\zeta_n$  and few effective DOFs in the DS,  $\alpha \propto \zeta_n^4$  holds approximately [12]. This is the origin of the strong enhancement of SGWB signals from hot DSs.

Following the same reasoning, the critical phase transition strength must also scale with  $\zeta_n^4$ . Comparing to equation (2.94) yields the expression

$$\alpha_\infty \equiv \frac{(T_{\text{DS}}^n)^2}{\rho_{\text{rad}}^n} \left[ \sum_b \frac{n_b}{24} \Delta m_b^2(\phi) + \sum_f \frac{n_f}{48} \Delta m_f^2(\phi) \right], \quad (3.41)$$

which indeed approximately grows with  $\zeta_n^4$  for small  $\zeta_n$ , when  $T_{\text{DS}}^n$  is kept constant.

In Figure 3.6, an overview of the different effects of the quantities  $\alpha$ ,  $\beta/H$ ,  $T_{\text{SM}}^n$  and  $D$  on the resulting GW spectrum can be found. To be able to investigate their individual effects, a benchmark point has been fixed, that is representative for the kind of signals of the model presented in chapter 4 and lies just below the region observable by LISA (see Figure 2.12). Explicitly,  $\alpha = 10^{-2}$ ,  $\alpha_\infty = 10^{-3}$ ,  $\beta/H = 10^2$ ,  $T_{\text{SM}}^n$  and  $D = 1$  have been fixed, whereas the total effective DOFs at nucleation have been set to  $g_{\text{eff},\rho}^{\text{tot},n} = g_{\text{eff},s}^{\text{tot},s} = 100$ .

The overall effect of changing one of the four parameters considered is the shift of the broken power law spectrum towards other frequencies or amplitudes. Increasing  $\alpha$ , corresponding to the investigation of a stronger phase transition, leads to stronger signals, as is intuitively clear. For larger  $\alpha \sim \mathcal{O}(1 - 10)$ , one can however observe that the signal strength saturates due to the term  $\propto \alpha / (1 + \alpha)$  in equation (2.89). Increasing the temperature ratio  $\zeta$  between the DS and the SM bath will therefore lead to stronger signal strengths, until a saturation for very strong phase transitions will be achieved.

$\alpha$  increases the  
signal strength

Slow transitions, i. e.  
low  $\beta/H$ , are  
favored for strong  
signals

The effect of increasing  $\beta/H$  is more subtle: Larger values indicate faster phase transitions and smaller bubbles sizes. This is because in a fast phase transition many bubbles form at the same time, with the result that they will collide while still being small [12]. The collision of these smaller bubbles creates smaller anisotropies in size and amplitude, such that the spectrum shifts to higher frequencies and the

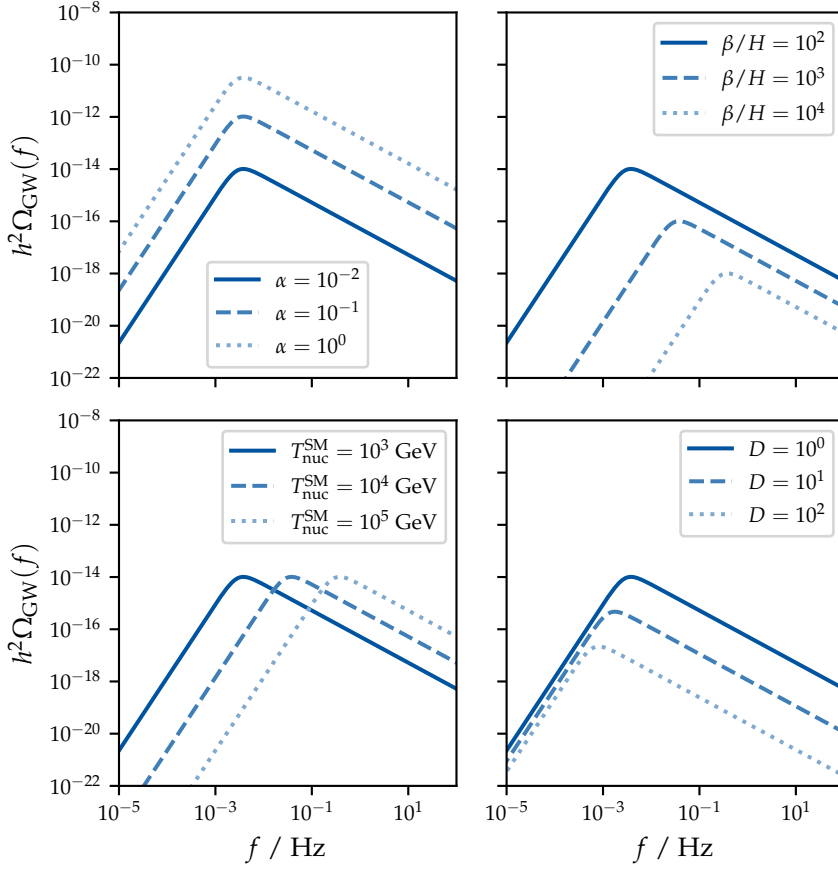


**Figure 3.6:** Plots of the SGWB spectrum generated by an FOPT, showing the individual effects of increasing the transition strength  $\alpha$ , the inverse time scale  $\beta/H$ , the temperature  $T_{\text{SM}}^{\text{n}}$  of the SM bath at the nucleation of bubbles, and the dilution factor  $D$ , introduced in equation (3.38). The transition strength meets the condition  $\alpha \gg \alpha_{\infty}$ . Thus, the phase transition produces runaway bubbles and the major part of the latent heat released is used to accelerate the bubble wall, such that the contribution from bubble collisions dominate over the sound wave and MHD production of GWs. For weaker transitions  $\alpha < \alpha_{\infty}$ , the sound waves will dominate over the scalar field contribution, thus giving a different power law spectrum. The effects presented in this figure will remain the same also in that case, even though the spectrum might obtain additional features, then. The parameters used for the benchmark point, depicted as a solid blue line in all plots, are given in the text.

overall signal strength becomes weaker. For that reason, low values of  $\beta/H$  are favored for observable signals.

*The peak frequency grows with  $T_{SM}^n$*

The only effect of increasing the nucleation temperature  $T_{SM}^n$  (next to comparably small changes in the DOFs of the SM bath and correspondingly small consequences for quantities depending on these) is the shift of the spectrum towards higher frequencies. This is not trivially clear, since the spectrum should naively just shift towards lower frequencies due to the increased redshift. Since the Hubble parameter at nucleation scales with  $(T_{SM}^n)^2$ , this effect, is however overcompensated for  $\beta/H = \text{const}$  and the relation  $f_p \propto T_{SM}^n$  is recovered, where  $f_p$  denotes the peak frequency [49].

*D dilutes the signal by shifting to lower strengths and frequencies*

Increasing the dilution factor finally yields the redshift to lower frequencies ( $\propto D^{-1/3}$ ) and lower amplitudes ( $\propto D^{-4/3}$ ), as discussed in section 3.4.3. As we have seen,  $D_{SM}$  increases with the temperature ratio  $\xi_{cd}$ . We will see that  $D$  will also increase for higher temperature ratios, such that there will be a series of competing effects: The increase in the transition strength, the shift in the SM nucleation temperature, and, ultimately, the increased dilution due to the increased amount of entropy injected into the SM bath.

So far we tried to treat the discussion of decaying hot DSs featuring an FOPT as model-independent as possible. The following chapter will finally become more concrete and investigate a given particle physics model and the possibility whether it can lead to an observable SGWB. This will answer also the question which of the effects on the GW spectrum will dominate when the temperature ratio between the sectors is increased.

# 4

## THE DARK PHOTON MODEL

We are now equipped with all the necessary tools to investigate a particular model of a DS, its possible phase transitions, the resulting SGWB, the decay of a mediator species, as well as the consequent entropy injection and dilution of the GW signal. In section 4.1, we will provide a detailed description of the model that we study in the rest of this chapter. We will find that the parameter space of our DS model can be expressed through five independent, physical quantities. A study of the effects occurring in the different regions of the available parameter space will be presented in section 4.2. Before we come to a short summary of the investigated model in section 4.4, we will analyze the expected SNRs for two benchmark points that can tell us about the capability of LISA and the ET to test our model in section 4.3.

*The structure of this chapter*

### 4.1 DEFINITION OF THE MODEL

In the following, we will consider an additional gauge group  $U(1)_D$  to the SM. Therein, the index “D” implies sufficiently weak interactions of the DS particles with those of the SM, such that the newly introduced particle species can be referred to as being “dark”. To achieve this, we assume that none of the SM particles are charged under the dark gauge group. The gauge boson of this new gauge group is a “dark photon” that mediates between particle species that are charged under the dark gauge symmetry. The idea for this model was first presented in 1985, predicting a kinetic mixing with the SM photon leading to a shift in the electromagnetic charges [60]. Moreover, we introduce a complex scalar field  $\Phi = (\phi + i\varphi) / \sqrt{2}$ , which we take to be a singlet under the SM gauge group and whose real part will obtain a non-zero VEV during an FOPT, in which  $\phi$  itself and the dark photon will become massive. The real part  $\phi$  of the dark Higgs field  $\Phi$  will be referred to as the “dark Higgs (boson)”. The DS can decay into SM particles as a result of the kinetic mixing of the dark photon with the SM photon as well as the mass mixing between the dark Higgs and the SM Higgs boson.

*Adding a dark Higgsed  $U(1)_D$  to the SM*

To obtain a gauge invariant Lagrangian, the covariant derivative acting on  $\Phi$  must also include the dark photon field  $B'_\mu$  which comes with a gauge coupling  $g$ :

$$D_\mu \Phi = \left( \partial_\mu + i g B'_\mu \right) \Phi. \quad (4.1)$$

The dark photon field strength tensor can be expressed as  $B'_{\mu\nu} = \partial_\mu B'_\nu - \partial_\nu B'_\mu$ . The corresponding quantities for the other U(1) gauge boson with which the dark photon can mix are denoted in the same way without a prime<sup>1</sup>. The relevant terms in the Lagrangian thus read [12]

$$\mathcal{L} \supset |D_\mu \Phi|^2 + |D_\mu H|^2 - \frac{1}{4} B'_{\mu\nu} B'^{\mu\nu} - \frac{\epsilon}{2} B'_{\mu\nu} B^{\mu\nu} - V(S, H), \quad (4.2)$$

*The tree-level potential*

where  $H$  is the SM Higgs field and  $\epsilon$  is the kinetic mixing parameter of the dark photon to the U(1)<sub>Y</sub> gauge boson. The most general tree-level potential for  $\Phi$  and  $H$ , being renormalizable and invariant under the model's symmetries, is given by [61]

$$V_{\text{tree}}(S, H) = -\mu^2 S^* S + \lambda (S^* S)^2 - \mu_H^2 H^\dagger H + \lambda_H (H^\dagger H)^2 + \lambda_p (S^* S) (H^\dagger H), \quad (4.3)$$

*The mass spectrum*

where  $\lambda$  ( $\lambda_H$ ) denotes the dark (SM) Higgs quartic coupling and  $\mu$  ( $\mu_H$ ) sets a corresponding mass scale. The coupling  $\lambda_p$  connects the two sectors and leads to a mass mixing of the two Higgs bosons and must thus be tiny for the sectors to be initially thermally decoupled [26]. Denoting the real part of the Higgs field  $H$  by  $h$ , which acquires a VEV in the EWPT, the field-dependent masses of the two physical Higgs bosons read

$$m_{(h,\phi)}^2(h, \phi) = \begin{pmatrix} -\mu_H^2 + 3\lambda_H h^2 + \frac{\lambda_p}{2}\phi^2 & \lambda_p h \phi \\ \lambda_p h \phi & -\mu^2 + 3\lambda\phi^2 + \frac{\lambda_p}{2}h^2 \end{pmatrix}. \quad (4.4)$$

Using this matrix, the respective mass terms in the tree-level potential can be written as  $V_{\text{tree}} \supset \frac{1}{2} \mathbf{v}^T m_{(h,\phi)}^2 \mathbf{v}$  with  $\mathbf{v} = (h, \phi)$ . Parameterizing the SM Higgs doublet as

$$H = \begin{pmatrix} G^+ \\ \frac{1}{\sqrt{2}} (h + i G^0) \end{pmatrix}, \quad (4.5)$$

<sup>1</sup> We assume here that the U(1) with which our U(1)<sub>D</sub> mixes is the gauge group of hypercharge U(1)<sub>Y</sub>. After the EWPT, the corresponding gauge group would be the gauge group of electromagnetism U(1)<sub>EM</sub>. The mathematical description of that would be equivalent, but the phenomenology of dark photon decays through mixing would change [23]. Since we will assume in the following that the mixing parameter  $\epsilon$  is sufficiently small such that only the dark Higgs can efficiently mediate between the two sectors, the following statements about the negligible mixing with the hypercharge gauge boson  $B$  will also hold for the gauge boson of electromagnetism.

the masses of the Goldstone modes  $G^0$  and  $G^+$  of the SM Higgs field and  $\varphi$  of the dark Higgs field can be calculated as

$$m_{G^0, G^+}^2(h, \phi) = -\mu_H^2 + \lambda_H h^2 + \frac{\lambda_p}{2} \phi^2, \quad (4.6a)$$

$$m_\varphi^2(h, \phi) = -\mu^2 + \lambda \phi^2 + \frac{\lambda_p}{2} h^2. \quad (4.6b)$$

The mixing between the hypercharge gauge bosons  $W^3$  and  $B$  and the dark photon field  $B'$  gives rise to the SM massive  $W^\pm$  and  $Z$  bosons, the massless photon  $A$  as well as the massive dark photon  $A'$ . The mass of the latter reads

$$m_{A'}(\phi) = g \phi \quad (4.7)$$

in the limit of small  $\epsilon$  [62]. We will work in the limit in which both  $\epsilon$  and  $\lambda_p$  are sufficiently small, such that we can ignore their individual effects during the phase transition and such that we can assume that the DS forms a distinct thermal bath. In that limit, the tree-level relations  $\mu^2 = \lambda v^2$  and  $m_{\text{DH}} \equiv m_\varphi = \sqrt{2\lambda} v$  hold, where  $v$  denotes the VEV of the real part  $\phi$  of the dark Higgs field, and the mass of the Goldstone boson  $\varphi$  vanishes. We will therefore be able to compute the dark Higgs potential using the three quantities  $\lambda$ ,  $g$  and  $v$ .

*The limit of small mixing parameters  $\epsilon$  and  $\lambda_p$*

In Figure 4.1, the effective potential of the model defined above is depicted for a series of increasing temperatures to show the individual effects of the different contributions to it. To calculate the daisy potential defined in equation (2.55c) for this example and the subsequent analysis, the following Debye masses are used [12]:

$$\Pi_\Phi(T_{\text{DS}}) = \left( \frac{\lambda}{3} + \frac{g^2}{4} \right) T_{\text{DS}}^2, \quad (4.8a)$$

$$\Pi_{A'}^L(T_{\text{DS}}) = \frac{g^2}{3} T_{\text{DS}}^2. \quad (4.8b)$$

For  $T_{\text{DS}} = 0$ , the tree-level potential  $V_{\text{tree}}$  gets corrections from  $V_{\text{CW}} + V_{\text{ctr}}$ , that increase the energy density of the potential minimum at  $\phi = v$ , which has been set to 1 TeV, but do not shift its position due to the imposed conditions on the counterterms given in the equations (2.57a) and (2.57b). Only for  $T_{\text{DS}} > 0$ , the additional potentials  $V_T + V_{\text{daisy}}$  contribute. For the critical temperature  $T_{\text{DS}} = T_{\text{DS}}^c \simeq 0.2 \text{ TeV}$ , the thermal corrections already dominate over the contributions from the Coleman-Weinberg potential and its counterterms. The daisy potential  $V_{\text{daisy}}$  therein leads to a small shift towards lower energy densities due to its relative sign with respect to  $V_T$ . The thermal corrections in total give rise to a barrier, through which  $\phi$  has to tunnel to reach the true vacuum state for lower temperatures, thus rendering it an FOPT. For higher temperatures, the thermal corrections completely dominate over the contributions for  $T_{\text{DS}} = 0$ , enforcing the field to remain in its symmetric  $\phi = 0$  configuration as has been argued in chapter 2.4.

*Contributions to the effective potential of the dark Higgs*

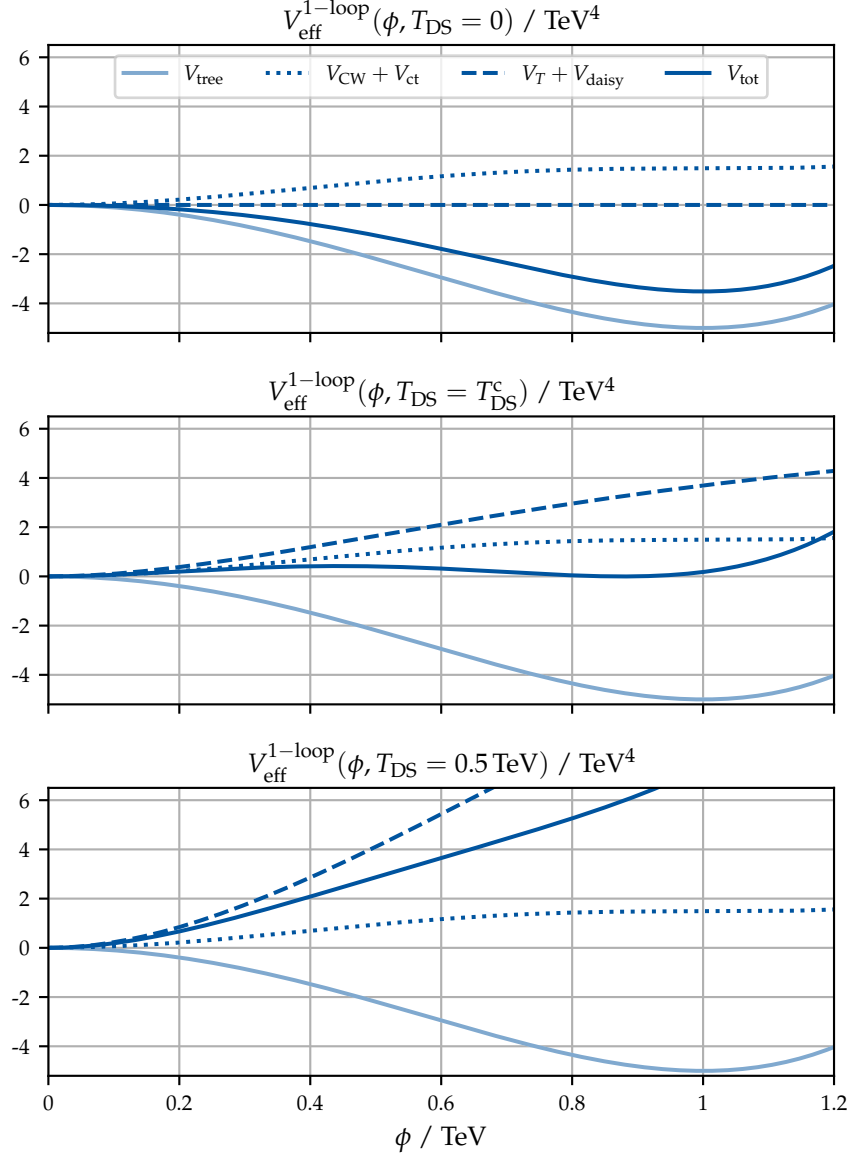


**Figure 4.1:** Plot of the effective 1-loop potential and its contributions from the tree-level potential  $V_{\text{tree}}$ , the Coleman-Weinberg potential and its counterterm potential  $V_{\text{CW}} + V_{\text{ct}}$ , as well as the temperature-dependent potentials  $V_T + V_{\text{daisy}}$  for three different temperatures. The effective potential energy for  $\phi = 0$  was subtracted from  $V_{\text{eff}}^{1\text{-loop}}$  for all temperatures. The quartic coupling was set to  $\lambda = 2 \cdot 10^{-3}$ , the gauge coupling was chosen as  $g = 0.5$ , and the tree level VEV has been fixed to  $v = 1$  TeV. For  $T_{\text{DS}} = 0$ , the only contributions to  $V_{\text{eff}}^{1\text{-loop}}$  come from  $V_{\text{CW}}$  and  $V_{\text{ct}}$ , which do not change the position of the true vacuum in field space, but increase its corresponding energy density due to the additional vacuum energy by self-interactions. At the critical temperature  $T_{\text{DS}}^c$ , the other potential terms contribute to a potential barrier, such that the minimum degenerates. At higher temperatures, the thermal contributions dominate and restore the symmetry for  $\phi = 0$ .

To be able to apply our discussion from the last chapter, where only one particle species was allowed to decay and to act as a mediator between the two sectors, we will assume that the dark photon does not contribute to the DS decays and that it is more massive than the dark Higgs boson. This will lead to a Boltzmann suppression of the dark photons and thus to the chemical decoupling of the two DS species at  $T_{\text{DS}}^{\text{cd}} \simeq m_{\text{DP}}$ , where  $m_{\text{DP}}$  denotes the dark photon mass<sup>2</sup>. Considering the tree-level relation for  $m_{\text{DH}}$  and comparing to the dark photon mass given in equation (4.7), the condition on the mass hierarchy is equivalent to  $g > \sqrt{2}\lambda$ , which allows for strong phase transitions, as we will see in the following section.

*Considering  $m_{\text{DP}} > m_{\text{DH}}$  for strong FOPTs and a dark Higgs mediator*

Only ultimately, during the decay of the dark Higgs, the effect of the mixing with SM particles will become important. The mass mixing can, however, only happen after the EWPT, during which the SM Higgs boson becomes massive. Before that, this decay channel is not available. However, including dimension-five operators in an effective field theory scenario of our DS would already allow for a decay of the dark Higgs boson to hypercharge bosons or gluons. We will remain agnostic about the specific decay channels and will therefore not further quantify the decay width  $\Gamma$  of the dark Higgs. Moreover, in the case of an effective field theory, there would be additional DOFs in the DS, whose freeze-out would alter the evolution of the temperature ratio between the sectors. We will therefore use the temperature ratio  $\zeta_n$  at the nucleation of the FOPT as a fixed point for the following analysis and derive the needed temperature ratios at later times by solving equation (3.5) numerically. In any case, the introduction of a specific description of the dependence of  $\Gamma$  on masses and couplings would not reduce the number of open parameters. We will therefore perform the analysis in a rather model-independent fashion by sticking to  $\Gamma$  in the scans presented in the following sections. We will also remain agnostic about possible UV-complete explanations that lead to the specific values of  $\zeta_n$  that we will use. Our study will therefore focus on the competing effect of the increase in  $\alpha$  and  $D$  when increasing the temperature ratio between the DSs and the SM bath, rather than specifics of the dark photon model.

*Why we choose  $\Gamma$  as a model parameter*

Hence, we can determine the model completely by fixing the dark Higgs quartic coupling  $\lambda$ , the  $U(1)_D$  gauge coupling  $g$ , the VEV  $v$ , the dark Higgs decay width  $\Gamma$  and the temperature ratio  $\zeta_n$  between the DS and the SM bath at the nucleation of bubbles during the FOPT. From these quantities, the mass spectrum of the relevant particles and the effective potential will be calculated. Then, the phase structure and the

*Model parameters:  $\lambda$ ,  $g$ ,  $v$ ,  $\zeta_n$ , and  $\Gamma$*

<sup>2</sup> We have checked explicitly that this assumption presents a conservative estimate on the expected SNRs. For  $T_{\text{DS}}^{\text{cd}} = C m_{\text{DP}}$  with  $0.1 < C < 1$ , the chemical decoupling occurs later, such that the dilution factors  $D$  will become smaller and the SGWB will be less diluted and thus more easily observable.

possible phase transitions encoded within the effective potential will be computed. In the case of a possible FOPT, when a thermally induced barrier exists at a critical temperature  $T_{\text{DS}}^{\text{c}}$ , the nucleation criterion in equation (2.63) is used to calculate a nucleation temperature  $T_{\text{DS}}^{\text{n}} < T_{\text{DS}}^{\text{c}}$ . To do so, it is necessary to solve a series of ODEs describing the bubble profiles and the corresponding bounce actions, see chapter 2.4. By calculating the derivative of the bounce action around the nucleation temperature, the inverse time scale  $\beta/H$  of the transition can be found. The nucleation temperature can further be used to calculate the transition strength  $\alpha$  by first computing the DOFs in the two sectors during the phase transition, which is necessary to calculate the radiation energy density of the surrounding plasma. By dividing the latent heat by the radiation energy density, one obtains the transition strength as was described in equation (2.91). Comparing  $\alpha$  to  $\alpha_{\infty}$  then determines whether the nucleating bubbles will reach a terminal velocity and how the energy budget of the transition is divided into kinetic energy accelerating the bubble walls, into sound waves, and MHD turbulence.

*Organizing the procedure of necessary calculations*

Next, the dilution factor  $D_{\text{SM}}$  due to the decay can be calculated as described in the last chapter: The temperature ratio  $\zeta_{\text{cd}}$  at the chemical decoupling of the dark photon from the dark Higgs is calculated from  $\zeta_{\text{n}}$  and the DOFs in the DS and the SM bath at that point. This thereby fixes also  $T_{\text{SM}}^{\text{cd}}$ . Together with  $m_{\text{DH}}$  and  $\alpha_{32}$ , which can be calculated using the dark Higgs quartic coupling  $\lambda$ , the dilution factor  $D_{\text{SM}}$  can be determined. To use the dilution factor for the calculation of the SGWB spectrum, it is translated into  $D$  using equation (3.35). The ten necessary parameters that govern the calculation of the SGWB are then all known, such that the GW spectrum can be determined. Finally, the SNR for the individual experiments, whose sensitivities have been shown in Figure 2.12, will be calculated to quantify the observability of the resultant signals.

During these calculations, it can happen that the nucleation temperature of the transition lies below the temperature at which the chemical decoupling would be expected, i. e.  $T_{\text{DS}}^{\text{n}} < T_{\text{DS}}^{\text{cd}} = m_{\text{DP}}$ . However, this is impossible, since both the dark photon as well as the dark Higgs are still massless before the transition, such that the chemical decoupling will be assumed to coincide with the phase transition, i. e.  $T_{\text{DS}}^{\text{cd}} = T_{\text{DS}}^{\text{n}}$ . In either case, the effective DOFs of the DS calculated assuming an LTE therein are checked to lie above 0.9 at the chemical decoupling, such that the dark Higgs is still relativistic, when the dark photon becomes Boltzmann suppressed. In the evaluation of the nucleation criterion, the DOFs of the DS will be set to four (corresponding to two internal DOFs for the massless dark photon and the dark Higgs each).

*Further assumptions on the nucleation and chemical decoupling*

Furthermore, this represents a conservative<sup>3</sup> approximation accounting for our ignorance of out-of-equilibrium effects that can happen at the bubble wall: Within the past two years, two additional processes known as the “bubble filtering” production [63, 64] and the “bubble expansion” [65, 66] production of particles have been found to be able to modify the naively expected particle abundances that can be calculated assuming an LTE at both sides of the bubble wall.

## 4.2 EXPLORATION OF THE MODEL PARAMETER SPACE

The parameter space of our model spanned by  $\lambda$ ,  $g$ ,  $v$ ,  $\Gamma$ , and  $\xi_n$  can be organized into groups: The only dimensionful quantities are  $v$  and  $\Gamma$ , out of which only  $v$  goes into the computation of the FOPT. Since  $\xi_n$  merely leads to a logarithmic shift in the nucleation criterion due to its occurrence in the effective DOFs  $g_{\text{eff},\rho}^{\text{tot},n}$ , the whole first part of the calculation can be understood by only considering  $\lambda$ ,  $g$ , and  $v$ . As has been argued before,  $g$  works as a measure of the height of the thermally induced potential barrier, while  $\lambda$  determines the importance of self-interactions in the tree-level potential. For a given quartic coupling  $\lambda$ , a large gauge coupling  $g$  therefore indicates stronger transitions, while a low  $g$  decreases the height of the potential barrier. Vice versa, for a fixed gauge coupling  $g$ , a small (large)  $\lambda$  indicates less (more) importance of the temperature-independent effects. We therefore observe the dependence of  $\alpha$  on these two parameters, as shown in Figure 4.2. The white area above the band in which FOPTs are possible refers to the case where the nucleation condition can never be fulfilled, such that the Universe is trapped in the false vacuum until today. In the area below, the contrary is the case: The thermally induced barrier is so low that the real part of the dark Higgs field does not have to tunnel to its true vacuum state to minimize its free energy. Instead, the transition rather occurs smoothly in the form of a crossover, in which no bubbles and no SGWB can form. We further observe that  $\alpha$  and  $\beta/H$  are not completely uncorrelated in our model, as it is usually the case [12, 26]: A strong transition is also a slow transition, which favors the observability of the produced signal.

*The couplings  $\lambda$  and  $g$  determine  $\alpha$  and  $\beta/H$*

We will focus on strong phase transitions in our analysis. We will therefore take  $\lambda = 1.5 \cdot 10^{-3}$  and  $g = 0.5$  as a benchmark point for a high potential barrier with low tree-level effects, resulting in a relatively strong ( $\alpha \simeq 10^{-1}$ ) and slow ( $\beta/H \simeq 10^3$ ) FOPT. However, any other point along the upper border of the colored band shown in

*The VEV  $v$  sets an energy scale; above  $\mathcal{O}(100 \text{ GeV})$  no influence on  $\alpha$  and  $\beta/H$*

<sup>3</sup> We have checked explicitly that a lower number of effective DOFs in the DS at the nucleation leads to weaker signal strengths due to the decrease in the dilution factor. The latter is due to the decrease in the temperature ratio  $\xi_{\text{cd}}$  for an already initially low number of DOFs  $g_{\text{eff},s}^{\text{DS},n}$  in the DS.

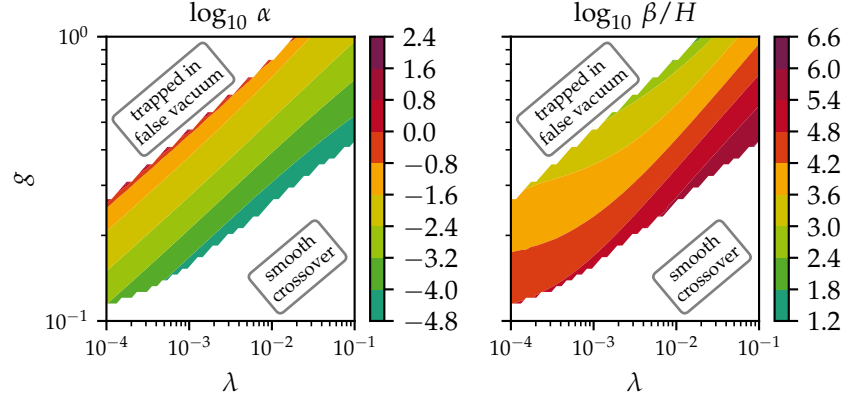


**Figure 4.2:** Plot of the phase transition strength  $\alpha$  and the inverse time scale  $\beta/H$  in dependence of the gauge coupling  $g$  and the quartic coupling  $\lambda$ . The tree level VEV has been set to  $v = 2$  TeV and the temperature ratio between the DS and the SM bath at the nucleation of the possible phase transition is fixed to  $\zeta_n = 1$ . There exists a band in the parameter space of  $g$  and  $\lambda$ , in which FOPTs are possible. If the gauge coupling is too large (small) for a given quartic coupling, the thermally induced barrier in the effective potential gets too large (small) for an FOPT to happen. Within the range of possible FOPTs, the ones at the upper boundary are therefore strong and slow, while at the lower boundary, the transitions are weak and fast.

Figure 4.2 could be chosen without changing the following discussion, as  $\alpha$  and  $\beta/H$  almost remain constant and the generated spectra therefore do not differ considerably. Further, setting a VEV  $v$  only has a relatively small effect on the transition strength and time scale, as its only influence consists in setting an energy scale, at which the effective DOFs of the SM particles being abundant during the nucleation is set. The latter go into the calculation of the radiation energy density, to which the latent heat of the transitions is normalized to, in order to obtain their strength  $\alpha$ . Since smaller  $v$  therefore lead to a smaller  $g_{\text{eff},\rho}^{\text{tot},n}$ , the transition strength increases slightly, when the VEV is decreased. The other way around, still keeping  $\lambda$  and  $g$  fixed, an increase in  $v$  will decrease  $\alpha$  until  $v \simeq 100$  GeV is reached, when the corresponding DOFs of the SM bath cannot increase considerably further. This expected behavior can also be seen in Figure 4.3, in which the influence of  $v$ ,  $\zeta_n$  and  $\Gamma$  on the SGWB spectrum are depicted in a condensed form: While for  $v = 1$  GeV (and  $\zeta_n = 1$ ) a peak signal strength above  $h^2 \Omega_{\text{GW}} \approx 10^{-13}$  can be reached, the compared spectra that have been obtained for  $v = 1$  TeV and  $v = 1$  PeV both have a peak signal strength that lies one order of magnitude below. To be more precise, we computed  $\alpha = 0.64$  for  $\zeta_n = 1$  and  $v = 1$  GeV, whereas we obtained  $\alpha = 0.14$  for  $v = 1$  TeV and  $v = 1$  PeV with the temperature ratio kept fixed at  $\zeta_n = 1$ .

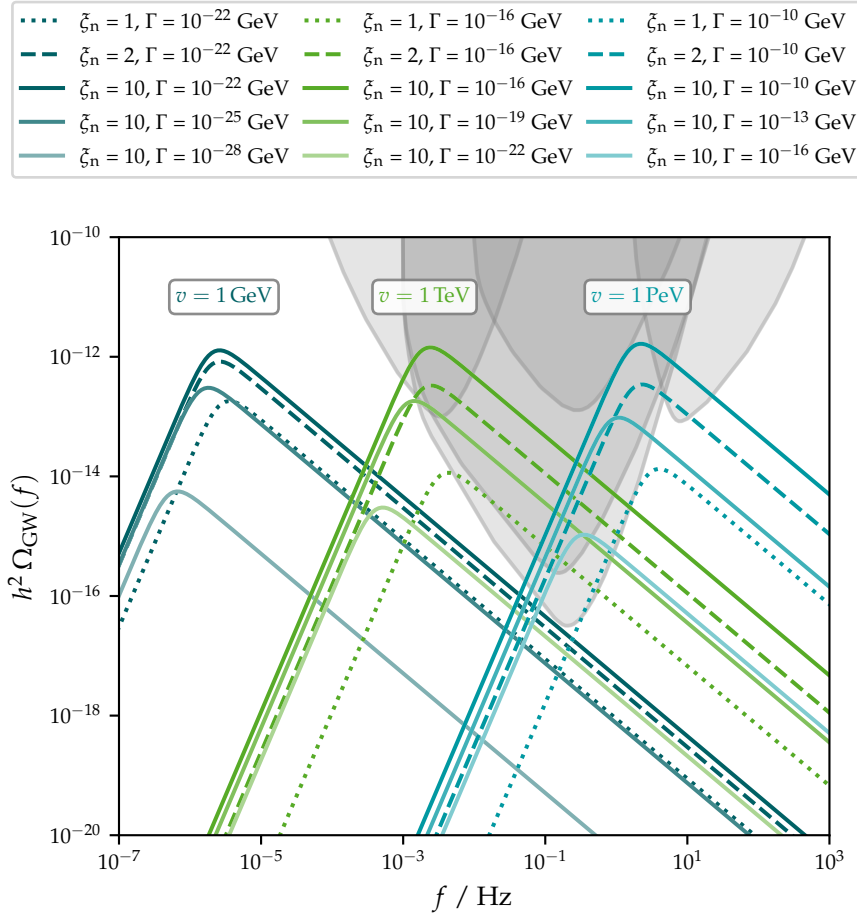


**Figure 4.3:** An overview plot for the different possible SGWB spectra that can be provided by our model for a strong FOPT ( $\lambda = 1.5 \cdot 10^{-3}$ ,  $g = 0.5$ ), compared to the expected PLI sensitivities of the different GW observatories presented in Figure 2.12. The plot shows the resulting spectra of the phase transition of a dark Higgs acquiring its VEV  $v = 1 \text{ GeV}$  (teal),  $v = 1 \text{ TeV}$  (green), or  $v = 1 \text{ PeV}$  (turquoise). Dotted lines refer to the case when  $\zeta_n = 1$ , whereas dashed and solid lines indicate  $\zeta_n = 2$  and  $\zeta_n = 10$ , respectively. The dependence of the spectrum on the dark Higgs' decay width is indicated by lighter colors. The main result is that increasing  $\zeta_n$  leads to a strong enhancement of the signal strength when the dark Higgs decays sufficiently fast. The tree level VEV shifts the signal to other frequencies and can have an influence on  $\alpha$ , determining the signal strength, for  $v \lesssim 100 \text{ GeV}$ .

*Increasing  $\zeta_n$  leads to stronger signals*

The effect of an increase of  $\zeta_n$  on the spectrum can be obtained by comparing the dotted, dashed, and solid lines in Figure 4.3: If the temperature ratio increases from 1 to 2, an increase of the signal strength by one to two orders of magnitude can be achieved. If the spectrum is already sufficiently high for  $\zeta_n = 1$  (as it is the case for  $v = 1$  GeV), the signal strength cannot be enhanced much further. Moreover, there seems to be a common maximal signal strength independent of the chosen VEV  $v$ . Both effects can be explained through the factor  $\propto \alpha/(1 + \alpha)$  that occurs in equation (2.89): If  $\alpha$  is already large ( $\gtrsim 1$ ) for  $\zeta_n = 1$ , as it is the case for  $v = 1$  GeV, the signal strength cannot be enhanced much further. Since the ratio  $\alpha/(1 + \alpha)$  converges to 1 for large  $\alpha$ , independent of  $v$ , the spectra all reach the same height in the presented cases in which  $\zeta_n = 10$ .

*If  $\Gamma$  is too low, dilution of the SGWB*

So far, only the impact of  $v$  and  $\zeta_n$  has been considered. The dark Higgs decay width  $\Gamma$  has been set to a relatively high value, corresponding to short lifetimes and no efficient injection of entropy into the SM, allowing for  $D \simeq 1$ , which indicates a negligible effect of dilution. This, however, changes when smaller dark Higgs decay widths are considered: If the dark Higgs becomes too long-lived, it can move out of equilibrium, inject a considerable amount of entropy into the SM bath, and dilute the SGWB to lower signal strengths and frequency scales, as has been depicted before in Figure 3.6.

It should be remarked that an increase in one order of magnitude in  $v$  has to be accompanied by an increase in two orders of magnitude in  $\Gamma$  to show a comparable signal strength with an approximately equal dilution factor. This is due to the scaling of the Hubble parameter with  $H \propto T^2$ , to which  $\Gamma$  has to be compared in the calculation of  $D$ . Therefore, the shift from  $v = 1$  GeV to  $v = 1$  TeV and  $v = 1$  PeV comes with a shift from  $\Gamma = 10^{-22}$  GeV to  $\Gamma = 10^{-16}$  GeV and  $\Gamma = 10^{-10}$  GeV to provide in all cases a dilution factor  $D \simeq 1$  for the uppermost curve.

*Defining benchmark points*

As we could see in Figure 4.3, VEVs in the TeV- and PeV-scale are favorable for a detection of the predicted signals with LISA and the ET, respectively. We will therefore extend our benchmark point for  $\lambda$  and  $g$ , denoting a slow and strong FOPT, to energy scales that are testable by the two experiments considered here. The two benchmark points can be found in Table 4.1. As is already clear from the shown Figure 4.3, the other GW interferometers planned to operate with higher sensitivities in the intermediate frequency range between LISA and the ET will be able to test the signals of weaker phase transitions, which our model can account for and whose strength could be enhanced by  $\zeta_n > 1$ . The following analysis will however focus on the study of strong phase transitions observable by LISA and the ET, as we expect them to be the first to start taking data.

Benchmark point	$\lambda$	$g$	$v$
LISA	$1.5 \cdot 10^{-3}$	0.5	2 TeV
ET	$1.5 \cdot 10^{-3}$	0.5	10 PeV

**Table 4.1:** Two benchmark points to study the impact of  $\Gamma$  and  $\zeta_n$  on the SGWB produced by a strong and slow FOPT, which can be tested by LISA or the ET.

To understand the impact of the temperature ratio  $\zeta_n$  on the FOPT, consider also the plots shown in Figure 4.4. Here, the LISA benchmark point was analyzed for  $\zeta_n \in [1, 10]$ . One can see that  $\alpha$  increases by about an order of magnitude and then saturates, when the temperature ratio is increased from 1 to 2. This matches the expected behavior that was derived in equation (3.40): For small  $\zeta_n$ , the transition strength (and the critical transition strength  $\alpha_\infty$ ) grow with  $\zeta_n^4$ . For larger  $\zeta_n$ , the DOFs of the DS dominate the radiation energy density, such that  $\alpha$  is no more dependent on the relative temperature of the DS with respect to the SM bath. This is intuitive since in the case of large  $\zeta_n$ , the Universe and its radiation energy are completely dominated by the DS, such that a change in the SM temperature has only a negligible effect, when  $T_{\text{DS}}$  is held constant. This can also be observed in the plot on the right-hand side: The total DOFs  $g_{\text{eff},\rho}^{\text{tot},n}$  at the nucleation grow with  $\zeta_n^4$  for large temperature ratios, thus canceling the  $\zeta_n^{-4}$  dependence of the SM temperature  $T_{\text{SM}}^4$  for a fixed DS temperature in equation (3.4a), when the DS dominates. The same phenomenon can be understood by observing how in equation (3.40) the dependence on  $\zeta_n$  drops out for large temperature ratios. It can further be observed that also  $(g_{\text{eff},s}^{\text{tot},n})^{4/3}$  grows with  $\zeta_n^4$  for large temperature ratios  $\zeta_n \gtrsim 3$ . The ratio between the two quantities on the right is therefore almost a constant, which a posteriori legitimates the argument that lead us to using  $D$  instead of  $D_{\text{SM}}$  in equation (3.39). The straight orange line for  $\beta/H$  in the left plot depicts the statement about the canceling of  $\zeta_n$  in the derivation of the inverse timescale. There exists however a slight change in  $T_{\text{DS}}^n$  due to the logarithmic corrections from  $g_{\text{eff},\rho}^{\text{tot},n}$  in the nucleation criterion that lead to an invisible change in  $\beta/H$  on the percent level for the considered range of temperature ratios.

*Understanding the increase of the signal strength:  $\alpha(\zeta_n)$*

*For large  $\zeta_n$ , no further increase possible since  $g_{\text{eff},\rho}^{\text{tot},n} \propto \zeta_n^4$*

### 4.3 OBSERVATION OF THE PRODUCED GRAVITATIONAL WAVES

The impact of our different model parameters has now been discussed—what is left is the analysis of the detectability of the predicted signals  $h^2 \Omega_{\text{GW}}(f)$ . As we have seen,  $\lambda$  and  $g$  determine  $\alpha$  and  $\beta/H$ , and thus

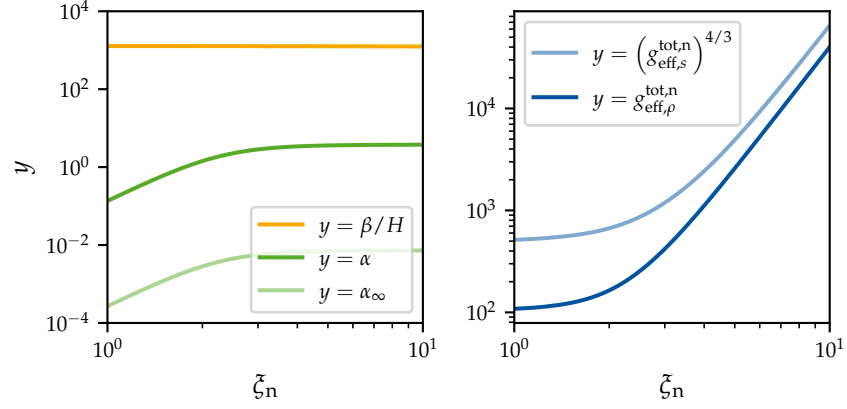


**Figure 4.4:** Dependence of the transition strength  $\alpha$ , the critical transition strength  $\alpha_\infty$ , the inverse time scale  $\beta/H$  (left), as well as the effective DOFs  $(g_{\text{eff},s}^{\text{tot},n})^{4/3}$  and  $g_{\text{eff},\rho}^{\text{tot},n}$  (right) on the temperature ratio  $\zeta_n$  at nucleation for the LISA benchmark point. The nucleation temperature in the DS is given by  $T_{\text{DS}}^n = 175 \text{ GeV}$ . The transition strength can be enhanced by increasing  $\zeta_n$  until  $g_{\text{eff},\rho}^{\text{tot},n}$  begins to scale with  $\zeta_n^4$ . Since the same argument holds also for  $\alpha_\infty \ll \alpha$ , the FOPT always occurs in the runaway bubble scenario. There is no relevant dependence of  $\beta/H$  on the temperature ratio  $\zeta_n$  and  $(g_{\text{eff},s}^{\text{tot},n})^{4/3}$  shows the same dependence on  $\zeta_n$  as  $g_{\text{eff},\rho}^{\text{tot},n}$ . The DOF ratio in equation (3.39) is therefore almost independent of  $\zeta_n$ .

control directly the strength of the resulting GW signals. Within the energy range of our interest, the only effect of  $v$  on the spectrum is to set a frequency scale. As could be seen in Figure 4.3, LISA will be able to test a frequency range that lies in the TeV scale, whereas the ET can test phase transitions above the PeV scale. This is the reason why we chose the particular set of parameters for our benchmark points in Table 4.1. Note that  $\zeta_n$  and  $\Gamma$  have not been specified for these points. From Figure 4.3 also only the general dependences on the observability of these two parameters can be deduced so far, while a quantitative analysis of the SNRs following the procedure explained in section 2.5.5 is still due. In this section, we will give an overview of the competing effects of  $\zeta_n$  and  $\Gamma$  on the expected SNRs. To do so, we will scan over the two leftover parameters for both of the defined benchmark points.

In Figure 4.5, the results of our analysis of the LISA benchmark point are shown. On the left-hand side, the dilution factor  $D$  is displayed as a function of  $\Gamma$  and  $\zeta_n$ , while the plot on the right-hand side shows the resulting SNRs of the generated signals for the expected LISA sensitivity curves. The dark Higgs decay width was chosen to range from  $\Gamma = 10^{-19} \text{ GeV}$  to  $\Gamma = 10^{-12} \text{ GeV}$ , corresponding to dark Higgs lifetimes between microseconds and a tenth of a picosecond.

*Investigating SNRs as a function of  $\zeta_n$  and  $\Gamma$  for the benchmark points*

*The LISA benchmark point*

The lower boundary of the decay width therefore corresponds to lifetimes that lead to dark Higgs decays happening around the QCD phase transition. In fact, the temperature  $T_{\text{SM}}^{\text{fin}}$  of the SM bath after the decay lies around  $\mathcal{O}(100 \text{ MeV})$  on the lower end of the plotted region of parameter space. The constraints from BBN and the CMB on the number of effective extra relativistic DOFs  $N_{\text{eff}}$  thus do not reduce the size of the feasible region of analyzed model parameter space. The mass of the dark photon is given by  $m_{\text{DP}} = g v = 0.5 \cdot 2 \text{ TeV} = 1 \text{ TeV}$ , whereas the dark Higgs mass lies at around  $m_{\text{DH}} = 110 \text{ GeV}$ . Since the thermally induced potential barrier is high due to the specific choice of  $g$  and  $\lambda$ , the nucleation temperature lies at a relatively low temperature of  $T_{\text{DS}}^{\text{n}} = 175 \text{ GeV}$ , below the mass of the dark photon. As has been shown in the previous discussion, the dark photon obtains its mass only during the phase transition and is thereby massless for  $T_{\text{DS}} > T_{\text{DS}}^{\text{n}}$ . Hence, the temperature of the chemical decoupling of the two DS species coincides with the nucleation, i. e.  $T_{\text{DS}}^{\text{cd}} = T_{\text{DS}}^{\text{n}}$ . This makes sense, since immediately after the transition  $m_{\text{DP}} \gg T_{\text{DS}}$  holds, resulting in the instantaneous decoupling of the dark photon. Therefore, the temperature ratio between the two sectors at the nucleation coincides with the chosen temperature ratios given along the horizontal axes, i. e.  $\xi_{\text{cd}} = \xi_{\text{n}}$ . Further, as has been already depicted in Figure 4.4, the considered transition is so strong that  $\alpha \gg \alpha_{\infty}$ , which implies that the latent heat of the FOPT goes directly into the acceleration of the bubble walls and eventually into their collision. This means that the spectral shape will remain a simple broken power law without any additional features at all points of the shown plane in the parameter space.

*Nucleation and chemical decoupling coincide*

For  $\xi_{\text{n}} = 1$ , the signal generated by the dark Higgs phase transition is not observable, regardless of the particular value of the dark Higgs decay width. When the temperature ratio is increased to  $\xi_{\text{n}} = 2$ , the GW spectrum becomes observable with LISA. What happens with the spectrum has already depicted in Figure 4.3 for a transition with  $v = 1 \text{ TeV}$  instead of  $2 \text{ TeV}$  (as in the benchmark point under consideration): The signal curve enters into the region that is enclosed by the PLI sensitivity curve, indicating the observability of the signal. This is however not possible, if the dark Higgs decay width is lower than about  $3 \cdot 10^{-19} \text{ GeV}$ . In that case, the dilution factor becomes too large for the signal to still be observable with the expected sensitivity of LISA. Going to higher temperature ratios, the competing effect of the increase in  $\alpha$ , leading to higher signal strengths, and the increase in  $D$ , leading to a shift to lower signal frequencies and strengths, result in a “rectangle” region of experimentally testable model parameter space.

*The competition between  $\alpha$  and  $D$  for large  $\xi_{\text{n}}$  and low  $\Gamma$*

As we noted in the previous chapter, we have to be aware that our fundamental assumption of the two considered sectors of particle physics being thermally decoupled only holds for sufficiently low  $\Gamma$ . In the plot, we excluded a part of the parameter space that should be

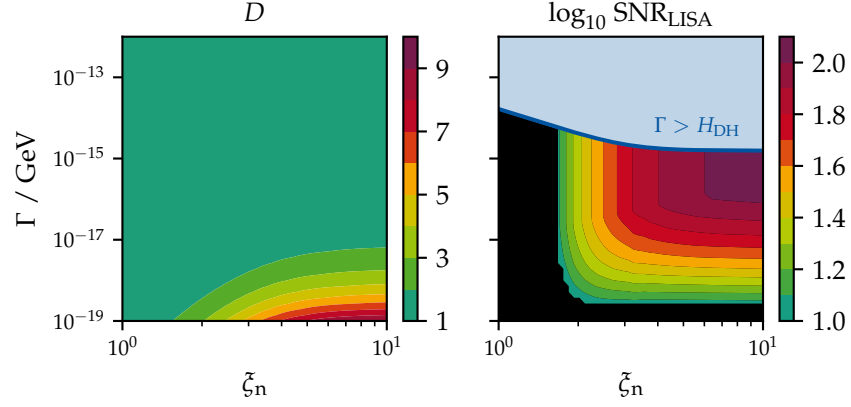


**Figure 4.5:** The dilution factor  $D$  (left) and the expected SNR (right) for the LISA benchmark point in dependence of the temperature ratio  $\zeta_n$  between the DS and the SM bath at nucleation and the decay width  $\Gamma$  of the dark Higgs. In large parts of the shown parameter space, the dilution factor is 1, such that the produced SGWB does not get diluted when the DS injects its entropy into the SM bath. This is however only the case if  $\Gamma$  is sufficiently high. When the dark Higgs becomes so short-lived that that  $\Gamma > H_{\text{DH}} \equiv H(T_{\text{DS}} = m_{\text{DH}})$ , our assumptions of a non-relativistic DS decay and distinct thermal baths do not hold any more, such that no qualified statements can be made about the region shaded in light blue.

*In the blue region,  
the DS is no more  
“dark”*

testable following our naive calculations, which is however forbidden as it violates the above condition. Explicitly, we require the dark Higgs to have a decay width below  $H_{\text{DH}} \equiv H(T_{\text{DS}} = m_{\text{DH}})$ . In doing so, we can exclude the case of relativistic dark Higgs decays, which our employed approximations do not account for. Additionally, we can neglect the effect of inverse decays of SM particles to dark Higgs bosons [24], which we ignored since the derivation of equation (2.13). If inverse decays could happen instead, the DS could moreover no longer be referred to as “dark”, when the dark Higgs gets non-relativistic, as the DS would already be coupled to the SM bath then. In the most extreme cases, close to the physically forbidden area in light blue, there lies the region in which the highest SNRs of  $\mathcal{O}(100)$  are expected. In these cases, the dark Higgs decays immediately after the phase transition while still following its equilibrium distribution. The entropy injection is thus minimal and virtually no dilution of the SGWB can be generated in the purple region.

*The ET benchmark  
point*

The very same picture can be drawn from our analysis of the ET benchmark point in Figure 4.6: Here, the VEV was set to  $v = 10 \text{ PeV}$  and the analyzed range of dark Higgs decay widths lies between  $10^{-11} \text{ GeV}$  and  $10^{-5} \text{ GeV}$ , corresponding to tiny dark Higgs lifetimes between  $10^{-13}$  and  $10^{-19}$  seconds. In these cases, the corresponding

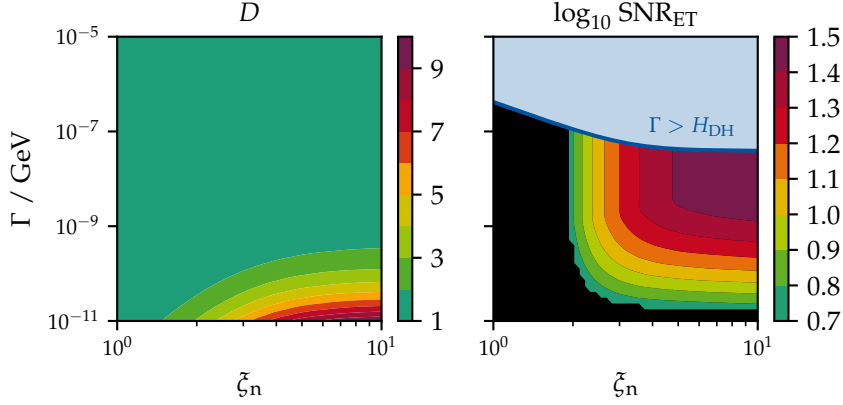


**Figure 4.6:** Scan over the temperature ratio  $\zeta_n$  and the decay width  $\Gamma$  of the dark Higgs for the ET benchmark point. The dilution factor  $D$  shows the same behavior as in the case for the LISA benchmark point. Also in this case, the dilution of the SGWB for a sufficiently long-lived dark Higgs and the finite sensitivity of the observatory lead to a lower limit of decay widths  $\Gamma$  that can be tested by the ET.

energy scales are so high, that (even for  $\zeta_n = 10$ ) the nucleation temperatures  $T_{\text{SM}}^n$  lie well above the electroweak scale. Thereby, the possible decay mechanism of the dark Higgs must be due to effects that could be explained in an effective field theory, but not in the currently presented form of the model. This is because no mixing between the massive dark Higgs boson and the still massless SM Higgs can occur before the EWPT. Explicitly, the nucleation temperature in the dark sector lies at  $T_{\text{DS}}^n = 851 \text{ TeV}$  and the mass spectrum is given by  $m_{\text{DP}} = 5 \text{ PeV}$  and  $m_{\text{DH}} = 548 \text{ TeV}$ . Hence, again due to the strong FOPT, the nucleation temperature lies below the dark photon mass, forcing the chemical decoupling to happen coincidentally with the nucleation. Therefore, the presented discussion of the LISA benchmark point also holds for the ET benchmark point. Note, however, that only slightly lower SNRs can be reached. This is due to the steeper sensitivity curve for lower frequencies of the ET with respect to LISA. A central result of our study of the chosen ET benchmark point is that the resultant SGWBs corresponding to a dark Higgs decay widths below  $2 \cdot 10^{-11} \text{ GeV}$  cannot be probed with the expected ET sensitivities for the investigated range of temperature ratios. Since both  $\alpha$  and  $D$  saturate for large temperature ratios, leading to the SNR losing its dependence of  $\zeta_n$ , the statement about the limit of testable parameter space will also hold for larger temperature ratios.

Using the results of our study of benchmark points, we can also make qualitative statements about the observation of SGWBs as predicted by our model with other experiments than LISA or the ET. In particular, as could be observed in Figure 4.3, for a phase transition, which is about

*More parameter space can be tested with better experimental sensitivities*

as strong as the one we considered in the benchmark points (which, hence, lies along the upper boundary of the plot shown in Figure 4.2), the generated signals for  $v = \mathcal{O}(\text{TeV-PeV})$  will likely be observable by DECIGO for combinations of  $\zeta_n$  and  $\Gamma$  that at least do not dilute the signal strongly. In fact, the signal described in the LISA benchmark point study could achieve even higher SNRs ranging from 30 to 3000 with DECIGO throughout all of the shown region of parameter space. In contrast, the ET benchmark point will not be testable by DECIGO, even for the most optimistic case of  $D = 1$  and  $\zeta_n = 10$ . This is due to the signal's power-law spectrum having about the same slope as the sensitivity curve and a slightly too-high peak frequency (or, equivalently,  $\text{VEV } v$ ).

*What would change for weak FOPTs*

For weaker transitions, lying in the center or even the lower end of the band shown in Figure 4.2, the condition  $m_{\text{DH}} < m_{\text{DP}}$  can still be fulfilled such that our assumption on the DS decay through dark Higgs bosons still holds. This also legitimates why we only focused on this case within our previous discussion. However, due to the decrease in  $\alpha$ , the spectra will lie orders of magnitude below those presented in Figure 4.3. Due to the increase in  $\beta/H$ , there will also be an additional increase of the peak frequency, as has been argued in the discussion of Figure 3.6 in the previous chapter. Therefore, to observe an FOPT that is weaker and faster compared to the benchmark cases discussed above, the VEV would have to lie at a lower energy scale than the one considered in our studies. The increase in the signal strength due to a large temperature ratio  $\zeta_n$  could in these cases indeed render a specific set of model parameters, usually only provoking a relatively weak and unobservable transition for  $\zeta_n = 1$ , testable with GW observatories. Moreover, an even larger increase in the signal strengths could be expected than in the two benchmark cases presented here for large temperature ratios, since the saturation in  $\alpha/(1 + \alpha)$  would not occur as quickly. Note that the above reasoning might be modified if the transitions become so weak that the impact of the bubble wall velocity, which we optimistically set to  $v_w = 1$ , can no longer be ignored in the calculation of the SGWB spectrum.

#### 4.4 SUMMARY

The central result of the investigation of the proposed model is that, indeed, the signal strength of an SGWB being generated through an FOPT in a DS will increase, if the relative temperature of the latter to the SM bath is increased. Put in a more direct wording: The hotter a DS featuring an FOPT is, the louder the resulting SGWB spectrum will be. Since a hot DS contains a considerable amount of energy which would lead to the untimely end of our Universe if it would remain

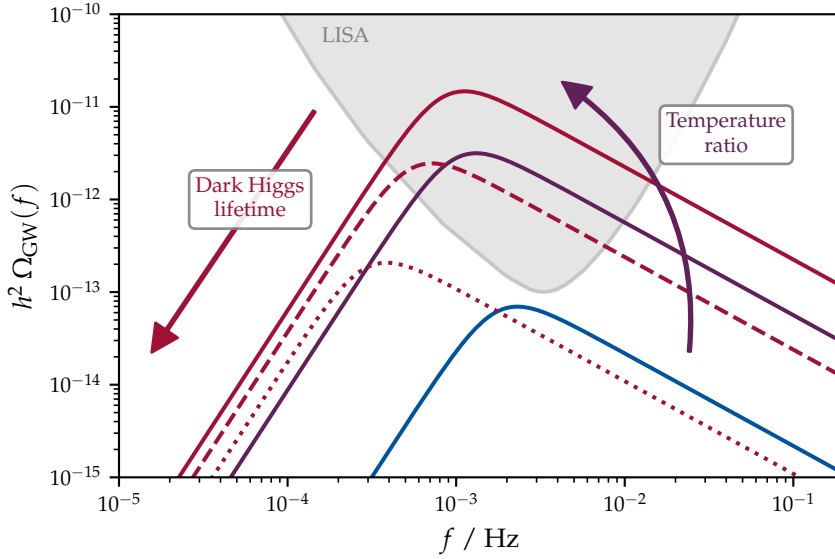


**Figure 4.7:** Overview of the two effects of the temperature ratio  $\zeta_n$  and the dark Higgs decay width  $\Gamma$  on the SGWB spectrum. An increase in  $\zeta_n$  increases the transition strength  $\alpha$ . Therefore, the GW signal gets amplified and becomes observable. This is, however, only possible if the dark Higgs is sufficiently short-lived. In the case of a long-lived dark Higgs, its decay injects a considerable amount of entropy into the SM bath, diluting the generated SGWB. The signal generated through the FOPT can therefore be tested by LISA only for sufficiently large temperature ratios and decay widths. The spectra shown in the plot refer to the LISA benchmark point with  $\zeta_n = 1$  (blue),  $\zeta_n = 2$  (violet), and  $\zeta_n = 5$  (red) and a dark Higgs decay widths of  $\Gamma = 10^{-16}$  GeV (solid lines),  $\Gamma = 10^{-18}$  GeV (dashed lines), and  $\Gamma = 10^{-20}$  GeV (dotted lines).

there, the energy must be injected into the SM bath through the decay of the DS, leading to a dilution of the produced SGWB. We found that this contrary process, being controlled by the decay width of the dark Higgs into SM particles, can lead to the non-observability of GW signals coming from long-lived DSs. Our results suggest that the detection of an SGWB of cosmological origin by LISA or the ET could be well-explained by a strong FOPT in a hot DS which decayed sufficiently fast to not dilute the resultant signal. The observation of weaker signals by other still-to-come GW experiments in a comparable frequency range with higher sensitivities could correspondingly be explained in our model by weaker FOPT in only warm DS, decaying later to SM particles. Figure 4.7 summarizes these results by comparing the spectrum of the SGWB generated by the LISA benchmark point for a choice of different temperature ratios  $\zeta_n$  and dark Higgs decay widths  $\Gamma$  to the corresponding PLI sensitivity region.

*A hotter DS is louder,  
if it decays  
sufficiently fast*



# 5 | CONCLUSIONS

In this thesis, we presented our studies on the stochastic gravitational wave backgrounds (SGWBs) which are produced by first-order phase transitions (FOPTs) in hot dark sectors (DSs). We showed that the signal strength of SGWBs can be enhanced by an increase of the temperature ratio between the DS and the Standard Model (SM) bath during the phase transition, as long as the lightest DS particle, carrying most of the DS energy density, decays sufficiently quickly into SM particles after the transition. If the DS is instead long-lived, the out-of-equilibrium decay of its lightest particle species can lead to a considerable entropy injection into the SM bath, resulting in the dilution of the SGWB. To demonstrate this general result, we investigated the parameter space of a minimalistic “dark”  $U(1)_D$  extension to the SM featuring an FOPT.

*Our main results*

In this phase transition, a complex scalar field charged under the additional gauge group develops a non-zero vacuum expectation value as the temperature decreases. Consequentially, bubbles nucleate into the hot primordial plasma, in which the radial mode of the scalar field and the gauge boson of the  $U(1)_D$  are massive. These bubbles eventually collide, giving rise to an SGWB. We refer to the two massive dark particle species as “the dark Higgs boson” and “the dark photon”, respectively, as we assume that their interactions with SM particles are negligible until the decay of the DS. Due to the lack of interactions, the two sectors form distinct thermal baths. We found that a DS temperature above that of the SM bath at the nucleation of bubbles increases the transition strength with respect to the case of coinciding temperatures. Considering the case of the dark photon being more massive than the dark Higgs, the dark photon will freeze out after the phase transition and leave the dark Higgs as the lightest DS state. Depending on the lifetime of the dark Higgs, it can become non-relativistic before its decay into SM particles and lead to an early matter domination. In this case, the dark Higgs decay will reheat the SM bath and dilute the SGWB considerably. To show the two individual effects, we analyzed two benchmark points for strong FOPTs testable by LISA and the ET. In either case, the SGWB can be observable, if the DS is at least twice as hot as the SM bath during the phase transition. We found that an observation is only possible for dark Higgs decay widths above  $3 \cdot 10^{-19}$  GeV for LISA and above  $2 \cdot 10^{-11}$  GeV for the ET. This corresponds to lifetimes below  $2 \cdot 10^{-6}$  s and  $3 \cdot 10^{-14}$  s, respectively.

*Our description of out-of-equilibrium decays extends the existing literature*

To calculate the dilution effect of the dark Higgs decay, we modeled the evolution of the DS after the phase transition and the subsequent thermalization with the SM bath. First, the two dark particle species form a local thermal equilibrium, which allows for the description using effective degrees of freedom. As soon as the DS temperature drops below the mass of the dark photon, we assume that it freezes out of the equilibrium. Afterwards, the dark Higgs is still relativistic. However, due to self-interactions number-changing processes can become relevant, resulting in an intermediate phase of cannibalism before the dark Higgs becomes non-relativistic. To describe the evolution of the energy density of the dark Higgs throughout its cannibalistic phase, we assumed that its chemical potential vanishes. We showed that in this case, the evolution of the dark Higgs energy density can be computed from the conservation of the comoving DS entropy density. Finally, we assumed that the dark Higgs decays non-relativistically. Our findings regarding the effects of an intermediate phase of cannibalism extend and improve the existing literature on out-of-equilibrium decays.

*Our code will be published*

We used and adapted CosmoTransitions [67] to perform the necessary calculations. To do so, we updated it to be used with Python 3, modularized it further to use model files, added a possibility to compute effective one-loop potentials, and implemented a general user interface for scans over parameter spaces. The code also offers the computation of signal-to-noise ratios for a list of GW observatories. Moreover, our code includes a module to solve the set of differential equations governing the out-of-equilibrium decay of a DS particle species, which can be preceded by a phase of cannibalism or early matter domination. This module can be used to quantify the dilution of SGWBs and frozen-out dark matter abundances. A publication of the code is still due, but a short summary of our extensions to the code can be found in the appendix A. It would also be particularly interesting to combine our code with the software tools GAMBIT [68] and Vevacious [69].

*New developments in the field, which we did not account for*

We employed the computational procedures described in the references [49] and [12] for calculating the resulting gravitational wave (GW) signals of FOPTs in DSs. As the field is however quickly evolving, we did not account for several new developments, which have been well-summarized in reference [48]: Most importantly, we did not include effects arising from the finite lifetime of GW sources and used the nucleation temperature as a reference scale to define thermodynamic quantities. New findings suggest to employ the “percolation temperature” instead, corresponding to the point in time where a significant fraction of the Universe is already filled with bubbles of the broken phase [70]. In our calculations, the obtained GW spectra for strong FOPTs were dominated by the contributions of bubble collisions, whose description relies heavily on previous semi-analytical work that uti-

lized the envelope approximation. In this approach, it is assumed that the scalar field's stress-energy is located in an infinitesimally thin shell around the bubble wall, which vanishes when two bubbles collide. Lately, this approximation was shown to yield larger signal strengths than predicted by fully numerical simulations of bubble collisions [71]. Moreover, we did not include the different particle interactions which can happen at the bubble wall in our computation, which have been presented in the references [63–66] and could, in turn, change the thermal evolution of the DS after the phase transition. We spared altogether the discussion of the different particle physics processes in the vicinity of bubble walls, which would constitute sources of friction on them. This approach relies on the assumption that the transitions under consideration are so strong for such effects to be sufficiently negligible. According to the references [12, 50], this approach is legitimate for phase transitions of the strength we considered in our benchmark point study. For weaker transitions, the runaway-bubble scenario in which bubble walls accelerate continuously will likely not be applicable, making necessary an in-depth analysis of the processes happening during the expansion of bubbles. In our calculation of the effective potential, we contented ourselves with the one-loop description including corrections from daisy diagrams which were resummed using the method proposed by Arnold and Espinoza [37]. Today, next to lattice QFT approaches, further developments have been achieved in the calculation of the effective potential, see for instance references [31, 72]. Further studies should respect these current developments. However, we are confident that the processes we described are so general that their effects will persist also when accounting for these recent findings for precision calculations. Nevertheless, more work will be needed to make our predictions completely robust.

In addition, it should be noted that our analysis of the evolution of the DS energy density after the FOPT reduced the complexity of the problem by approximating the results of the full numerical solution of the Boltzmann equation. In doing so, we ignored the case of relativistic and inverse mediator decays as well as the scenario in which more than one DS species is able to thermalize the two sectors. Subsequent studies should investigate these possibilities to obtain a more general description of the decay of hot DSs. Moreover, we remained agnostic about possible explanations for the occurring temperature ratios between the SM bath and the DS, which we required in our analysis. Additionally, we did not present a self-contained discussion of possible decay channels of the the dark Higgs boson before the electroweak phase transition. Hence, we focused on a rather model-independent approach when choosing the dark Higgs decay width as a fundamental model parameter of our analysis. Future studies are needed to close this gap and connect the decay width with the dark Higgs mass and the couplings to its decay products, to allow for a

*Many ideas for  
further research*

phenomenological analysis of the dark photon model. An intriguing possibility for further studies will also be the discussion whether the frozen-out dark photon in our model could account for (a fraction of) dark matter in our Universe. The dilution effect due to the dark Higgs decay might allow for particularly high dark photon masses above  $\mathcal{O}(100 \text{ TeV})$ , which would be forbidden for non-diluted dark matter by the unitarity bound [13].

*We live in exciting  
times!*

The results of our research open the doors for many possible future projects. In the light of the recent observations of NANOGrav [8, 11] and the plans for additional space-based GW observatories next to LISA, we are looking forward to many more hints towards a satisfying understanding of SGWBs. It is fascinating to see the rapid progress in the field of observational GW physics, which kick-started with the detection of the first signals only five years ago [3]. The weakness of Newtons gravitational constant, or equivalently the huge energy scale of the Planck mass, dictates that the sources of observable GWs have to be staggering events of tremendous power, be it the merger of black holes and neutron stars or the collision of bubbles in the hot plasma of primordial particle species. Therefore, we can already now predict that the experimental results using GW observatories of the next generation will allow us to further investigate our cosmos and get closer to an understanding of its very beginning. It is humbling to realize that we are still the first generation of physicists in the human history that can directly probe how our Universe must have looked like 14 billion years ago. However, to unravel the still unknown mysteries of the most remote corners of space-time, there is still a lot of work to be done, paving the way for many future studies to come.

# A

## THE SOFTWARE EMPLOYED FOR OUR CALCULATIONS

To perform our analysis of the possible phase transitions in DSs, we used a customized version of CosmoTransitions by Carroll L. Wainwright [67]. CosmoTransitions comes with the necessary tools to trace the global and local minima of a given effective potential of one or multiple scalar fields. Moreover, it allows to identify the possible phase transitions between these minima. CosmoTransitions is often used as a benchmark code in the literature [69, 73], as it is sufficiently stable and fast. Next to the identification of FOPTs, also the calculation of bounce actions and bubble profiles is possible with CosmoTransitions.

We first updated the individual modules of the program to work with Python 3 and extended it by an accurate nucleation criterion for FOPTs in DSs with a distinct temperature from the SM bath. Next, we added the code necessary to compute the important phase transition parameters  $\alpha$  and  $\beta/H$ . This required a model file, in which the effective potential  $V_{\text{eff}}^{1\text{-loop}}(\phi)$  and the mass spectrum of the DS are given, and an additional module to calculate effective DOFs. Furthermore, we added a module for the calculation of dilution factors  $D_{\text{SM}}$ , in which the decay of the DS is modeled. Another module for the calculation of SGWB spectra and SNRs has been added to interpret the observability of the generated signals. This set of modules is controlled by an interface, which itself is executed by a small scan file, which defines the region of parameter space, that one wishes to analyze. In addition, there are a few parameters for adjusting the accuracy of scans and the grid over which one likes to scan, for instance.

An overview of the tree of dependences of these different modules in our program is shown in Figure A.1. In the following, we will discuss briefly, what the individual modules can be used for. Note that this list is not exhaustive and includes only the most important features.

**my\_scan.py** defines the kind of analysis, that a user wishes to perform. This includes a simple computation of the resultant SGWB of a hot DS phase transition for a given set of parameters or whole scans over regions of parameter space. In either case, first a model file **my\_model.py** has to be called. Then, a set of physical input parameters is specified. If a scan is performed, the grid size and the range of parameters to be scanned over has to be set. The latter allows for combinations of linearized and logarithmized scales on the two axes of the plane in parameter

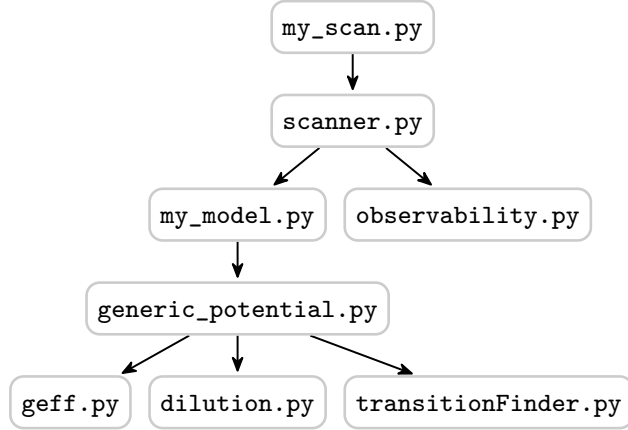


**Figure A.1:** The tree of dependences of the different modules that we employed in our calculations. A user can modify the files `my_scan.py` to specify the parameter region and accuracy of a scan. A DS model can be defined in `my_model.py`. The output of each scan will be a large set of plots to show how physical quantities like particle masses or nucleation temperatures vary throughout the chosen plane in the model parameter space. The output also includes plots of SNRs for the detection of the produced SGWBs, see e. g. Figure 4.5.

space. Further, all additional specifications of the model can be adjusted in this file. This allowed for example for a quick comparison between a different number of DOFs in the DS until the onset of the FOPT, see footnote 3 in chapter 4.1. Since it can always happen that `CosmoTransitions` gets stuck at some step in the calculation for certain parameter values, we added a possibility to re-scan over slightly shifted parameter points. The maximum number of tries and the relative shifts can be adjusted. For a correct labeling of the parameters in the produced plots at the end of the calculation, `TEX` code can be used to name the parameters.

**scanner.py** translates the chosen input parameters in `my_scan.py` into calls of the model file `my_model.py`. As the scans require high computing power, the code also allows for multiprocessing and a progress bar is shown throughout all computations. In the case of an analysis of a single parameter point, the resulting SGWB spectrum is plotted. We also included a possibility to directly compare the resulting spectra of different sets of input parameters, as was shown in Figure 4.3. If a plane in parameter space is analyzed, a large array of all input and output parameters is saved and evaluated by `observability.py`. A list of all input and output parameters of our program can be found in table A.1. Next to the quantities  $\alpha$ ,  $\alpha_\infty$ ,  $\beta/H$ ,  $T_{\text{SM}}^n$  as well as the DOFs  $g_{\text{eff},\rho}^{\text{tot},n}$  and  $g_{\text{eff},\rho}^{\text{tot},s}$ , which are needed for the calculation of the

GW signals, several other interesting parameters are calculated. These have been obtained throughout the calculations and can be used to interpret the resulting signal spectra. Since all parameters are plotted also a second time after being logarithmized, and all SNRs for the observatories shown in Figure 2.12 are plotted, a total of about 80 plots are produced within each scan. In the end of the calculation, all parameters and plots are saved together with a list of warnings and error messages.

**my\_model.py** is a child of `generic_potential.py`. It uses  $\lambda, g, v/\text{GeV}, \zeta_n,$  and  $\Gamma/\text{GeV}$  as an input to compute the effective one-loop potential and the mass spectrum of the model. We allowed to use either the daisy resummation procedure by Arnold and Espinoza, the Parwani method or no daisy resummation at all, see chapter 2.3.4.2. To ensure the computation's numerical stability, we set the VEV throughout the calculation to 100 and re-scaled dimensionful quantities to the correct energy units afterwards.

**generic\_potential.py** is an interface of the module which analyzes the phase transitions of the given effective potential. It is taken from `CosmoTransitions` and extends the original code by the calculation of the output parameters from table A.1. First, the possible phase transitions encoded in the effective potential are analyzed using `transition_finder.py`. Then, the nucleation criterion is solved to obtain the nucleation temperature. Thereafter, all of the parameters necessary to compute the SGWB are calculated, except for the dilution factor  $D_{\text{SM}}$ . This calculation is performed in the external module `dilution.py`. If the calculated dilution factor  $D_{\text{SM}}$  is equivalent to  $D < 1$ , we correct the two dilution factors accordingly to  $D = 1$  and  $D_{\text{SM}} = g_{\text{eff},s}^{\text{tot},n} / g_{\text{eff},s}^{\text{SM},n}$ . The case of  $D < 1$  is non-physical, as it would violate the second law of thermodynamics [13]. We found that this manual correction is only necessary in regions where a vanishing dilution effect has been expected in either case. To calculate the exclusion bounds for  $\Gamma > H_{\text{DH}} \equiv H(T_{\text{DS}} = m_{\text{DH}})$  (see Figure 4.5), we also compute the temperature ratio  $\zeta_{\text{DH}}$  and the effective energy DOFs  $g_{\text{eff},\rho}^{\text{tot},\text{DH}}$  at  $T_{\text{DS}} = m_{\text{DH}}$ . The Hubble parameter can then be obtained using

$$H_{\text{DH}} = \sqrt{\frac{\pi^2}{90} g_{\text{eff},\rho}^{\text{tot},\text{DH}} \frac{m_{\text{DH}}^4}{\zeta_{\text{DH}}^4 m_{\text{Pl}}^2}}. \quad (\text{A.1})$$

**transition\_finder.py** offers the possibility to trace the minima of the effective potential, to generate a list of possible phase transitions, and to solve the nucleation criterion. To do so, it solves the bounce equation (2.62) and integrates the obtained bubble profiles in order to calculate the bounce action of a transition at a given temperature  $T_{\text{DS}} < T_{\text{DS}}^c$ , which lies below the critical

temperature of a FOPT. The absolute value of the difference of the right- and left-hand side of the nucleation criterion in equation (2.63) is minimized to find its solution  $T_{\text{DS}}^n$ . This repeated computation of bounce actions is numerically expensive and the bottleneck of the presented program. To precisely determine  $\beta/H$ , we increased the internal accuracy of the bounce action calculation and used in each case at least 50 of support to evaluate the derivative of the bounce action at the nucleation temperature, see equation (2.92). The derivative was calculated using the slope of a linear function that was fitted to the bounce action around the nucleation temperature. The large number of points of support has shown to be necessary due to numerical instabilities of CosmoTransitions in the calculation of the bounce action.

**geff.py** is a small module to evaluate the integrals in the equations (3.3a) and (3.3c) to compute dark sector DOFs. For a given temperature  $T_{\text{SM}}$ , the DOFs of the SM bath are calculated using an interpolation of the data given in the ancillary material of reference [54].

**dilution.py** contains an implementation of the set of equations (3.33). These can be used to quantify the entropy injection of a decaying particle species, mediating between the DS and the SM. To integrate the set of differential equations numerically, the equations have been logarithmized. The input parameters of this module are the SM temperature  $T_{\text{SM}}^{\text{cd}}$  at the chemical decoupling of the mediator species, the mediator mass  $m_{\text{med}}$ , its decay width  $\Gamma$  in GeV, the temperature ratio  $\zeta_{\text{cd}}$  at chemical decoupling, the energy density of frozen-out DM  $f_{\text{mat}} = \rho_{\text{DM}}^{\text{cd}} / \rho_{\text{med}}^{\text{cd}}$ , normalized to the mediator energy density, the internal mediator degrees of freedom  $g_{\text{med}}$ , and the effective  $3 \rightarrow 2$  coupling  $\alpha_{32}$  of the mediator. The output parameters of this module are the dilution factor  $D_{\text{SM}}$  and the temperature of the SM bath after the mediator decay  $T_{\text{SM}}^{\text{fin}}$ . We used an interpolation function for  $\frac{d \ln \bar{\rho}}{d \ln \bar{s}}$ , which is required to evaluate the function  $\zeta(\theta)$ , defined in equation (3.11).

**observability.py** is used to quantify the observability of the GW signals generated by the analyzed FOPTs. First, the produced SGWB spectra are calculated using equation (2.89). Then, they are compared to the expected noise spectra for the considered GW observatories to compute SNRs. The noise spectra are taken from the ancillary material of reference [12]. In the case of a scan over the model parameter space, plots are produced, which show how the output parameters listed in table A.1 change throughout the considered region of parameter space.

Parameter	Explanation
$\lambda$	Dark Higgs quartic coupling
$g$	$U(1)_D$ gauge coupling
$v/\text{GeV}$	Tree-level VEV of the dark Higgs potential
$\zeta_n$	Temperature ratio at nucleation
$\Gamma/\text{GeV}$	Decay width of the dark Higgs
$\alpha$	Transition strength
$\alpha_\infty$	Critical transition strength for runaway bubbles
$\beta/H$	Inverse time scale of the transition
$D_{\text{SM}}$	Entropy ratio $S_{\text{SM}}^{\text{fin}}/S_{\text{SM}}^{\text{cd}}$
$D$	Entropy ratio $S_{\text{SM}}^{\text{fin}}/S_{\text{tot}}^{\text{cd}}$ , see reference [13]
$T_{\text{SM}}^n/\text{GeV}$	Temperature of the SM bath at nucleation
$T_{\text{DS}}^n/\text{GeV}$	Temperature of the DS at nucleation
$g_{\text{eff},\rho}^{\text{SM},n}$	Effective energy DOFs of the SM at nucleation
$g_{\text{eff},\rho}^{\text{DS},n}$	Effective energy DOFs of the DS at nucleation
$g_{\text{eff},\rho}^{\text{tot},n}$	Total effective energy DOFs at nucleation
$g_{\text{eff},s}^{\text{SM},n}$	Effective entropy DOFs of the SM at nucleation
$g_{\text{eff},s}^{\text{DS},n}$	Effective entropy DOFs of the DS at nucleation
$g_{\text{eff},s}^{\text{tot},n}$	Total effective entropy DOFs at nucleation
$g_{\text{eff},\rho}^{\text{tot},n} / \left( g_{\text{eff},s}^{\text{tot},n} \right)^{4/3}$	Ratio of effective DOFs, see equation (3.39)
$T_{\text{DS}}^c/\text{GeV}$	Critical temperature of the DS
$T_{\text{SM}}^{\text{fin}}/\text{GeV}$	Temperature of the SM bath after the decay of the dark Higgs
$m_{\text{DP}}/\text{GeV}$	Mass of the dark photon
$m_{\text{DH}}/\text{GeV}$	Mass of the dark Higgs
$\Delta m_{\text{DP-DH}}/\text{GeV}$	Mass difference of dark photon and dark Higgs
$\zeta_{\text{cd}}$	Temperature ratio at chemical decoupling
$T_{\text{SM}}^{\text{cd}}$	Temperature of the SM bath at chemical decoupling
$\zeta_{\text{DH}}$	Temperature ratio, when $T_{\text{DS}} = m_{\text{DH}}$
$\zeta_{\text{DP}}$	Temperature ratio, when $T_{\text{DS}} = m_{\text{DP}}$
$g_{\text{eff},\rho}^{\text{tot},\text{DH}}$	Total effective energy DOFs, when $T_{\text{DS}} = m_{\text{DH}}$
$g_{\text{eff},\rho}^{\text{tot},\text{DP}}$	Total effective energy DOFs, when $T_{\text{DS}} = m_{\text{DP}}$

**Table A.1:** List of input parameters (*above the horizontal line*) and output parameters (*below the horizontal line*) of the presented code and the dark photon model. “At nucleation” denotes the onset of the FOPT, when the nucleation criterion in equation (2.63) is fulfilled, whereas “at chemical decoupling” describes the moment, when the dark photon decouples from the dark Higgs.



## BIBLIOGRAPHY

- [1] Albert Einstein. "Approximative Integration of the Field Equations of Gravitation." In: *Sitzungsber. Preuss. Akad. Wiss. Berlin (Math. Phys. )* 1916 (1916), pp. 688–696.
- [2] Albert Einstein. "Über Gravitationswellen." In: *Sitzungsber. Preuss. Akad. Wiss. Berlin (Math. Phys. )* 1918 (1918), pp. 154–167.
- [3] The LIGO Scientific Collaboration and the Virgo Collaboration. "Observation of Gravitational Waves from a Binary Black Hole Merger." In: *Phys. Rev. Lett.* 116, 061102 (2016) (Feb. 11, 2016). DOI: 10.1103/PhysRevLett.116.061102. arXiv: 1602.03837v1 [gr-qc].
- [4] The LIGO Scientific Collaboration et al. "GWTC-1: A Gravitational-Wave Transient Catalog of Compact Binary Mergers Observed by LIGO and Virgo during the First and Second Observing Runs." In: *Phys. Rev. X* 9, 031040 (2019) (Nov. 30, 2018). DOI: 10.1103/PhysRevX.9.031040. arXiv: 1811.12907v3 [astro-ph.HE].
- [5] R. Abbott et al. "GWTC-2: Compact Binary Coalescences Observed by LIGO and Virgo During the First Half of the Third Observing Run." In: (Oct. 27, 2020). arXiv: 2010.14527v3 [gr-qc].
- [6] Edward W. Kolb and Michael S. Turner. *The Early Universe*. Vol. 69. 1990. ISBN: 978-0-201-62674-2.
- [7] Michele Maggiore. "Gravitational wave experiments and early universe cosmology." In: *Phys. Rept.* 331 (2000), pp. 283–367. DOI: 10.1016/S0370-1573(99)00102-7. arXiv: gr-qc/9909001.
- [8] Zaven Arzoumanian et al. "The NANOGrav 12.5-year Data Set: Search For An Isotropic Stochastic Gravitational Wave Background." In: *The Astrophysical Journal Letters, Volume 905, Number 2* (2020) (Sept. 9, 2020). DOI: 10.3847/2041-8213/abd401. arXiv: 2009.04496v2 [astro-ph.HE].
- [9] Wolfram Ratzinger, Pedro Schwaller, and Ben A. Stefanek. "Gravitational Waves from an Axion-Dark Photon System: A Lattice Study." In: (Dec. 2020). arXiv: 2012.11584 [astro-ph.CO].
- [10] Michele Maggiore. *Gravitational Waves. Vol. 2: Astrophysics and Cosmology*. Oxford University Press, Mar. 2018. ISBN: 978-0-19-857089-9.

- [11] Zaven Arzoumanian et al. "Searching For Gravitational Waves From Cosmological Phase Transitions With The NANOGrav 12.5-year dataset." In: (Apr. 28, 2021). arXiv: 2104.13930v1 [astro-ph.CO].
- [12] Moritz Breitbach, Joachim Kopp, Eric Madge, Toby Opferkuch, and Pedro Schwaller. "Dark, Cold, and Noisy: Constraining Secluded Hidden Sectors with Gravitational Waves." In: *JCAP* 07 (2019) 007 (Nov. 27, 2018). DOI: 10.1088/1475-7516/2019/07/007. arXiv: 1811.11175v2 [hep-ph].
- [13] Marco Cirelli, Yann Gouttenoire, Kalliopi Petraki, and Filippo Sala. "Homeopathic Dark Matter, or how diluted heavy substances produce high energy cosmic rays." In: (Nov. 8, 2018). DOI: 10.1088/1475-7516/2019/02/014. arXiv: 1811.03608v3 [hep-ph].
- [14] Pablo Carlos Budassi. *Observable sphere for 3d*. Rendered for Wikimedia.org. Aug. 2020. URL: [https://commons.wikimedia.org/wiki/File:Observable\\_sphere\\_for\\_3d.png](https://commons.wikimedia.org/wiki/File:Observable_sphere_for_3d.png).
- [15] Julien Lesgourgues. *The Ingredients of the Universe*. Lecture course given at RWTH Aachen University in the summer term 2019.
- [16] Planck Collaboration et al. "Planck 2018 results. VI. Cosmological parameters." In: *A&A* 641, A6 (2020) (July 17, 2018). DOI: 10.1051/0004-6361/201833910. arXiv: 1807.06209v3 [astro-ph.CO].
- [17] Dietrich Bodeker and Wilfried Buchmuller. "Baryogenesis from the weak scale to the grand unification scale." In: (Sept. 15, 2020). arXiv: 2009.07294v2 [hep-ph].
- [18] Stefano Profumo. *An Introduction to Particle Dark Matter*. World Scientific, 2017. ISBN: 978-1-78634-000-9. DOI: 10.1142/q0001.
- [19] Nima Arkani-Hamed, Savvas Dimopoulos, and G. R. Dvali. "The Hierarchy problem and new dimensions at a millimeter." In: *Phys. Lett. B* 429 (1998), pp. 263–272. DOI: 10.1016/S0370-2693(98)00466-3. arXiv: hep-ph/9803315.
- [20] Y. Fukuda et al. "Evidence for oscillation of atmospheric neutrinos." In: *Phys. Rev. Lett.* 81 (1998), pp. 1562–1567. DOI: 10.1103/PhysRevLett.81.1562. arXiv: hep-ex/9807003.
- [21] Antonio Riotto and Mark Trodden. "Recent progress in baryogenesis." In: *Ann. Rev. Nucl. Part. Sci.* 49 (1999), pp. 35–75. DOI: 10.1146/annurev.nucl.49.1.35. arXiv: hep-ph/9901362.
- [22] Leszek Roszkowski, Enrico Maria Sessolo, and Sebastian Trojanowski. "WIMP dark matter candidates and searches - current status and future prospects." In: *Rept.Prog.Phys.* 81 (2018) no.6, 066201 (July 19, 2017). DOI: 10.1088/1361-6633/aab913. arXiv: 1707.06277v2 [hep-ph].

- [23] Jim Alexander et al. “Dark Sectors 2016 Workshop: Community Report.” In: (Aug. 30, 2016). arXiv: 1608.08632v1 [hep-ph].
- [24] Marco Hufnagel. “Primordial Nucleosynthesis in the Presence of MeV-scale Dark Sectors.” Dissertation, Universität Hamburg, 2020. Dissertation. Hamburg: Universität Hamburg, 2020, p. 175. DOI: 10.3204/PUBDB-2020-02699. URL: <https://bib-pubdb1.desy.de/record/441760>.
- [25] Stefan Heimersheim, Nils Schöneberg, Deanna C. Hooper, and Julien Lesgourgues. “Cannibalism hinders growth: Cannibal Dark Matter and the  $S_8$  tension.” In: (Aug. 19, 2020). DOI: 10.1088/1475-7516/2020/12/016. arXiv: 2008.08486v2.
- [26] Moritz Breitbach. “Gravitational Waves from Cosmological Phase Transitions.” MA thesis. Johannes Gutenberg University Mainz, Apr. 2018. URL: <https://www.glk.uni-mainz.de/files/2019/01/MasterThesis-MoritzBreitbach.pdf>.
- [27] Mariano Quiros. “Finite temperature field theory and phase transitions.” In: *ICTP Summer School in High-Energy Physics and Cosmology*. Jan. 1999. arXiv: hep-ph/9901312.
- [28] Mark B. Hindmarsh, Marvin Lüben, Johannes Lumma, and Martin Pauly. “Phase transitions in the early universe.” In: *SciPost Phys. Lect. Notes 24 (2021)* (Aug. 20, 2020). DOI: 10.21468/SciPostPhysLectNotes.24. arXiv: 2008.09136v3 [astro-ph.CO].
- [29] Yuhao Yang. “An Introduction to Thermal Field Theory.” MA thesis. Imperial College London, Sept. 2011. URL: <https://www.imperial.ac.uk/media/imperial-college/research-centres-and-groups/theoretical-physics/msc/%5C%5C%20dissertations/2011/Yuhao-Yang-Dissertation.pdf>.
- [30] Steven Weinberg. *The quantum theory of fields. Vol. 2: Modern applications*. Cambridge University Press, Aug. 2013. ISBN: 978-1-139-63247-8.
- [31] David Curtin, Patrick Meade, and Harikrishnan Ramani. “Thermal Resummation and Phase Transitions.” In: (Dec. 1, 2016). arXiv: 1612.00466v1 [hep-ph].
- [32] Cédric Delaunay, Christophe Grojean, and James D Wells. “Dynamics of non-renormalizable electroweak symmetry breaking.” In: *Journal of High Energy Physics* 2008.04 (Apr. 2008), pp. 029–029. ISSN: 1029-8479. DOI: 10.1088/1126-6708/2008/04/029. URL: <http://dx.doi.org/10.1088/1126-6708/2008/04/029>.
- [33] Oliver Gould. “Real scalar phase transitions: a nonperturbative analysis.” In: *JHEP* 04 (2021) 057 (Jan. 14, 2021). DOI: 10.1007/JHEP04(2021)057. arXiv: 2101.05528v2 [hep-ph].

- [34] Rajesh R. Parwani. "Resummation in a hot scalar field theory." In: *Phys. Rev. D* 45 (1992). [Erratum: *Phys.Rev.D* 48, 5965 (1993)], p. 4695. DOI: 10.1103/PhysRevD.45.4695. arXiv: hep-ph/9204216.
- [35] Eibun Senaha. "Symmetry Restoration and Breaking at Finite Temperature: An Introductory Review." In: *Symmetry* 12.5 (2020), p. 733. DOI: 10.3390/sym12050733.
- [36] M. E. Carrington. "The Effective potential at finite temperature in the Standard Model." In: *Phys. Rev. D* 45 (1992), pp. 2933–2944. DOI: 10.1103/PhysRevD.45.2933.
- [37] Peter Brockway Arnold and Olivier Espinosa. "The Effective potential and first order phase transitions: Beyond leading-order." In: *Phys. Rev. D* 47 (1993). [Erratum: *Phys.Rev.D* 50, 6662 (1994)], p. 3546. DOI: 10.1103/PhysRevD.47.3546. arXiv: hep-ph/9212235.
- [38] Thomas Hambye, Alessandro Strumia, and Daniele Teresi. "Super-cool Dark Matter." In: *JHEP* 1808 (2018) 188 (May 3, 2018). DOI: 10.1007/JHEP08(2018)188. arXiv: 1805.01473v2 [hep-ph].
- [39] Andrei D. Linde. "Decay of the False Vacuum at Finite Temperature." In: *Nucl. Phys. B* 216 (1983). [Erratum: *Nucl.Phys.B* 223, 544 (1983)], p. 421. DOI: 10.1016/0550-3213(83)90072-X.
- [40] Michael J. Baker and Joachim Kopp. "The Vev Flip-Flop: Dark Matter Decay between Weak Scale Phase Transitions." In: *Phys. Rev. Lett.* 119, 061801 (2017) (Aug. 26, 2016). DOI: 10.1103/PhysRevLett.119.061801. arXiv: 1608.07578v3 [hep-ph].
- [41] Michael J. Baker, Moritz Breitbach, Joachim Kopp, and Lukas Mittnacht. "Dynamic Freeze-In: Impact of Thermal Masses and Cosmological Phase Transitions on Dark Matter Production." In: *JHEP* 1803 (2018) 114 (Dec. 11, 2017). DOI: 10.1007/JHEP03(2018)114. arXiv: 1712.03962v2 [hep-ph].
- [42] Sidney R. Coleman. "The Fate of the False Vacuum. 1. Semiclassical Theory." In: *Phys. Rev. D* 15 (1977). [Erratum: *Phys.Rev.D* 16, 1248 (1977)], pp. 2929–2936. DOI: 10.1103/PhysRevD.16.1248.
- [43] Andrei D. Linde. "Fate of the False Vacuum at Finite Temperature: Theory and Applications." In: *Phys. Lett. B* 100 (1981), pp. 37–40. DOI: 10.1016/0370-2693(81)90281-1.
- [44] Riccardo Apreda, Michele Maggiore, Alberto Nicolis, and Antonio Riotto. "Gravitational waves from electroweak phase transitions." In: *Nucl. Phys. B* 631 (2002), pp. 342–368. DOI: 10.1016/S0550-3213(02)00264-X. arXiv: gr-qc/0107033.
- [45] Michele Maggiore. *Gravitational Waves. Vol. 1: Theory and Experiments*. Oxford Master Series in Physics. Oxford University Press, 2007. ISBN: 978-0-19-857074-5.

- [46] Daniel Kennefick. *Traveling at the speed of thought: Einstein and the quest for gravitational waves*. Princeton, USA: Univ. Pr., 2007.
- [47] Disrael Camargo Neves da Cunha and Christophe Ringeval. "Interferences in the Stochastic Gravitational Wave Background." In: (Apr. 29, 2021). arXiv: 2104.14231v1 [astro-ph.CO].
- [48] Huai-Ke Guo, Kuver Sinha, Daniel Vagie, and Graham White. "The Benefits of Diligence: How Precise are Predicted Gravitational Wave Spectra in Models with Phase Transitions?" In: (Mar. 11, 2021). arXiv: 2103.06933v1 [hep-ph].
- [49] Chiara Caprini et al. "Science with the space-based interferometer eLISA. II: Gravitational waves from cosmological phase transitions." In: (Dec. 19, 2015). DOI: 10.1088/1475-7516/2016/04/001. arXiv: 1512.06239v2 [astro-ph.CO].
- [50] Dietrich Bodeker and Guy D. Moore. "Electroweak Bubble Wall Speed Limit." In: *JCAP* 05 (2017), p. 025. DOI: 10.1088/1475-7516/2017/05/025. arXiv: 1703.08215 [hep-ph].
- [51] Jose R. Espinosa, Thomas Konstandin, Jose M. No, and Geraldine Servant. "Energy Budget of Cosmological First-order Phase Transitions." In: *JCAP* 1006:028,2010 (Apr. 23, 2010). DOI: 10.1088/1475-7516/2010/06/028. arXiv: 1004.4187v1 [hep-ph].
- [52] Anson Hook, Gustavo Marques-Tavares, and Davide Racco. "Causal gravitational waves as a probe of free streaming particles and the expansion of the Universe." In: (Oct. 7, 2020). DOI: 10.1007/JHEP02(2021)117. arXiv: 2010.03568v2 [hep-ph].
- [53] Lars Husdal. "On Effective Degrees of Freedom in the Early Universe." In: *Galaxies*, 4(4), 78 (2016) (Sept. 16, 2016). DOI: 10.3390/galaxies4040078. arXiv: 1609.04979v3 [astro-ph.CO].
- [54] Ken'ichi Saikawa and Satoshi Shirai. "Primordial gravitational waves, precisely: The role of thermodynamics in the Standard Model." In: *JCAP* 05(2018)035 (Mar. 2, 2018). DOI: 10.1088/1475-7516/2018/05/035. arXiv: 1803.01038v2 [hep-ph].
- [55] Eric D. Carlson, Marie E. Machacek, and Lawrence J. Hall. "Self-interacting dark matter." In: *Astrophys. J.* 398 (1992), pp. 43–52. DOI: 10.1086/171833.
- [56] Adrienne L. Erickcek, Pranjal Ralegankar, and Jessie Shelton. "Cannibal domination and the matter power spectrum." In: (Aug. 10, 2020). arXiv: 2008.04311v1 [astro-ph.CO].
- [57] Marco Farina, Duccio Pappadopulo, Joshua T. Ruderman, and Gabriele Trevisan. "Phases of Cannibal Dark Matter." In: (July 11, 2016). DOI: 10.1007/JHEP12(2016)039. arXiv: 1607.03108v2 [hep-ph].

- [58] Robert J. Scherrer and Michael S. Turner. “Decaying Particles Do Not Heat Up the Universe.” In: *Phys. Rev. D* 31 (1985), p. 681. DOI: 10.1103/PhysRevD.31.681.
- [59] Steven Weinberg. *Cosmology*. 2008. ISBN: 978-0-19-852682-7.
- [60] Bob Holdom. “Two  $U(1)$ ’s and Epsilon Charge Shifts.” In: *Phys. Lett. B* 166 (1986), pp. 196–198. DOI: 10.1016/0370-2693(86)91377-8.
- [61] David Curtin, Rouven Essig, Stefania Gori, and Jessie Shelton. “Illuminating Dark Photons with High-Energy Colliders.” In: (Nov. 28, 2014). DOI: 10.1007/JHEP02(2015)157. arXiv: 1412.0018v2 [hep-ph].
- [62] Jia Liu, Xiao-Ping Wang, and Felix Yu. “A Tale of Two Portals: Testing Light, Hidden New Physics at Future  $e^+e^-$  Colliders.” In: *JHEP06(2017)077* (Apr. 3, 2017). DOI: 10.1007/JHEP06(2017)077. arXiv: 1704.00730v2 [hep-ph].
- [63] Michael J. Baker, Joachim Kopp, and Andrew J. Long. “Filtered Dark Matter at a First Order Phase Transition.” In: *Phys. Rev. Lett.* 125, 151102 (2020) (Dec. 5, 2019). DOI: 10.1103/PhysRevLett.125.151102. arXiv: 1912.02830v2 [hep-ph].
- [64] Dongjin Chway, Tae Hyun Jung, and Chang Sub Shin. “Dark matter filtering-out effect during a first-order phase transition.” In: *Phys. Rev. D* 101, 095019 (2020) (Dec. 9, 2019). DOI: 10.1103/PhysRevD.101.095019. arXiv: 1912.04238v2 [hep-ph].
- [65] Aleksandr Azatov and Miguel Vanvlasselaer. “Bubble wall velocity: heavy physics effects.” In: (Oct. 6, 2020). DOI: 10.1088/1475-7516/2021/01/058. arXiv: 2010.02590v3 [hep-ph].
- [66] Aleksandr Azatov, Miguel Vanvlasselaer, and Wen Yin. “Dark Matter production from relativistic bubble walls.” In: (Jan. 14, 2021). arXiv: 2101.05721v1 [hep-ph].
- [67] Carroll L. Wainwright. “CosmoTransitions: Computing Cosmological Phase Transition Temperatures and Bubble Profiles with Multiple Fields.” In: (Sept. 19, 2011). DOI: 10.1016/j.cpc.2012.04.004. arXiv: 1109.4189v1 [hep-ph].
- [68] Peter Athron et al. “GAMBIT: The Global and Modular Beyond-the-Standard-Model Inference Tool.” In: *Eur. Phys. J. C* 77.11 (2017). [Addendum: *Eur.Phys.J.C* 78, 98 (2018)], p. 784. DOI: 10.1140/epjc/s10052-017-5321-8. arXiv: 1705.07908 [hep-ph].
- [69] J. E. Camargo-Molina, B. O’Leary, W. Porod, and F. Staub. “**Vevacious**: A Tool For Finding The Global Minima Of One-Loop Effective Potentials With Many Scalars.” In: *Eur. Phys. J. C* 73.10 (2013), p. 2588. DOI: 10.1140/epjc/s10052-013-2588-2. arXiv: 1307.1477 [hep-ph].

- [70] Xiao Wang, Fa Peng Huang, and Xinmin Zhang. “Phase transition dynamics and gravitational wave spectra of strong first-order phase transition in supercooled universe.” In: *JCAP*05 (2020) 045 (Mar. 19, 2020). DOI: 10.1088/1475-7516/2020/05/045. arXiv: 2003.08892v3 [hep-ph].
- [71] Daniel Cutting, Elba Granados Escartin, Mark Hindmarsh, and David J. Weir. “Gravitational waves from vacuum first order phase transitions II: from thin to thick walls.” In: *Phys. Rev. D* 103, 023531 (2021) (May 27, 2020). DOI: 10.1103/PhysRevD.103.023531. arXiv: 2005.13537v2 [astro-ph.CO].
- [72] Djuna Croon, Oliver Gould, Philipp Schicho, Tuomas V. I. Tenkanen, and Graham White. “Theoretical uncertainties for cosmological first-order phase transitions.” In: *JHEP* 04 (2021) 055 (Sept. 21, 2020). DOI: 10.1007/JHEP04(2021)055. arXiv: 2009.10080v2 [hep-ph].
- [73] Chiara Caprini et al. “Detecting gravitational waves from cosmological phase transitions with LISA: an update.” In: (Oct. 29, 2019). DOI: 10.1088/1475-7516/2020/03/024. arXiv: 1910.13125v2 [astro-ph.CO].



# Eidesstattliche Versicherung

## Statutory Declaration in Lieu of an Oath

Tasillo, Carlo

Name, Vorname/Last Name, First Name

Matrikelnummer (freiwillige Angabe)

Matriculation No. (optional)

Ich versichere hiermit an Eides Statt, dass ich die vorliegende ~~Arbeit/Bachelorarbeit/~~ Masterarbeit\* mit dem Titel

I hereby declare in lieu of an oath that I have completed the present paper/Bachelor thesis/Master thesis\* entitled

Listening to hot dark sector phase transitions

selbstständig und ohne unzulässige fremde Hilfe (insbes. akademisches Ghostwriting) erbracht habe. Ich habe keine anderen als die angegebenen Quellen und Hilfsmittel benutzt. Für den Fall, dass die Arbeit zusätzlich auf einem Datenträger eingereicht wird, erkläre ich, dass die schriftliche und die elektronische Form vollständig übereinstimmen. Die Arbeit hat in gleicher oder ähnlicher Form noch keiner Prüfungsbehörde vorgelegen.

independently and without illegitimate assistance from third parties (such as academic ghostwriters). I have used no other than the specified sources and aids. In case that the thesis is additionally submitted in an electronic format, I declare that the written and electronic versions are fully identical. The thesis has not been submitted to any examination body in this, or similar, form.

Aachen, 21. Mai 2021

Ort, Datum/City, Date

Unterschrift/Signature

\*Nichtzutreffendes bitte streichen

\*Please delete as appropriate

### Belehrung:

#### Official Notification:

#### § 156 StGB: Falsche Versicherung an Eides Statt

Wer vor einer zur Abnahme einer Versicherung an Eides Statt zuständigen Behörde eine solche Versicherung falsch abgibt oder unter Berufung auf eine solche Versicherung falsch aussagt, wird mit Freiheitsstrafe bis zu drei Jahren oder mit Geldstrafe bestraft.

#### Para. 156 StGB (German Criminal Code): False Statutory Declarations

Whoever before a public authority competent to administer statutory declarations falsely makes such a declaration or falsely testifies while referring to such a declaration shall be liable to imprisonment not exceeding three years or a fine.

#### § 161 StGB: Fahrlässiger Falscheid; fahrlässige falsche Versicherung an Eides Statt

(1) Wenn eine der in den §§ 154 bis 156 bezeichneten Handlungen aus Fahrlässigkeit begangen worden ist, so tritt Freiheitsstrafe bis zu einem Jahr oder Geldstrafe ein.

(2) Straflosigkeit tritt ein, wenn der Täter die falsche Angabe rechtzeitig berichtigt. Die Vorschriften des § 158 Abs. 2 und 3 gelten entsprechend.

#### Para. 161 StGB (German Criminal Code): False Statutory Declarations Due to Negligence

(1) If a person commits one of the offences listed in sections 154 through 156 negligently the penalty shall be imprisonment not exceeding one year or a fine.

(2) The offender shall be exempt from liability if he or she corrects their false testimony in time. The provisions of section 158 (2) and (3) shall apply accordingly.

Die vorstehende Belehrung habe ich zur Kenntnis genommen:

I have read and understood the above official notification:

Aachen, 21. Mai 2021

Ort, Datum/City, Date

Unterschrift/Signature